

AG Gensch
TECHNISCHE UNIVERSITÄT BERLIN

Institut für Optik und Atomare Physik
Faculty II

Master's Thesis

**Laboratory Studies on Laser-Induced Shock Waves
for LIBS Measurements on Mars**

Fabian Seel

Matriculation Number: 356694

22nd of July 2021

Supervisors:

Prof. Dr. Michael Gensch
Prof. Dr. Heinz-Wilhelm Hübers

Declaration of Authenticity

I declare that this thesis was composed by myself, that the work contained herein is my own except where explicitly stated otherwise in the text, and that this work has not been submitted for any other degree or professional qualification except as specified.

Erklärung zur eigenständigen Anfertigung

Hiermit erkläre ich, dass ich die vorliegende Arbeit selbständig und eigenhändig sowie ohne unerlaubte fremde Hilfe und ausschließlich unter Verwendung der aufgeführten Quellen und Hilfsmittel angefertigt habe.

Berlin, 2021-07-22

Place, Date
Ort, Datum

Signature
Unterschrift

Abstract

The research presented in this thesis examines the shock waves generated by laser induced breakdown spectroscopy (LIBS) measurements in the context of robotic planetary exploration. When investigating the history of planetary bodies, compositional data of geological samples is of great interest, as changing climate conditions on the surface or geological features like rivers leave traces in the composition and structure of rocks on the surface. The chemical composition of rocks and soils can be analysed with the LIBS method. This emission spectroscopy technique works by focusing a laser beam on the surface of a geological sample. A small amount of material is ablated and ionized. The plasma subsequently emits a spectrum characteristic for the material's composition. Further information about the target properties can be inferred from a pressure wave that is generated by the expanding plasma.

When probing the same spot on a geological sample multiple times, a growing crater forms from the repeated ablation process that affects both the pressure wave signal and the emitted spectrum. Acoustic recordings of the pressure wave present complementary data to the LIBS spectra, allowing for instance to deduce the material's hardness. This data could also potentially be used for normalisation applications.

Some scientific missions on the surface of Mars employ the LIBS technique already to analyse the composition of geological samples in-situ. With the successful landing of the Mars 2020 mission's Perseverance rover, sounds such as the pressure wave emitted during the laser ablation process can be recorded for the first time with the SuperCam instrument suite.

To better understand the evolution of the pressure wave and the processes involved in its generation, this work investigates the expansion of the shock wave shortly after the ignition of the plasma in a simulated Martian atmosphere experimentally, so results can be applied to in-situ data from Mars. For this, a schlieren imaging system was designed and built, allowing to directly image the density fluctuations induced by the shock wave. By fitting a Taylor-Sedov model to the temporal evolution of the shock wave position, changes in the energy of the explosion were monitored over the course of a series of shots on the same position. To the author's knowledge, this work represents the first time that the schlieren imaging technique was used to investigate laser-induced shock waves in this low pressure regime and specifically at Martian atmospheric conditions.

A data set containing acoustic recordings, spectral measurements and schlieren images was collected for several materials with different hardnesses, thermal properties and optical properties. The previously reported correlation between a decrease in acoustic energy and the material's hardness could be confirmed for most non-metals. Comparing the evolution of the explosion energy with the development of the acoustic and spectral signals showed that target properties influence the measured parameters in different ways.

The influence of the laser energy and the atmospheric pressure on the shock wave dynamics and the acoustic energy of the pressure wave were also investigated. A linear correlation between the laser's energy and the explosion energy was found, as well as a linear correlation with the acoustic energy of the pressure wave at later stages. The explosion energy was

shown to vary little with changing atmospheric pressures. Furthermore, the acoustic energy was found to grow linearly with rising ambient pressure, while the shock wave dynamics are slowed down in an environment with higher pressure. In the pressure range relevant for Martian surface operations, the data obtained in this study showed notable changes in the shock wave, suggesting that diurnal and annual variations could affect the Martian in-situ data. Moreover, changes in the laser pulse energy that are expected for data from SuperCam due to sampling targets at varying distances affect the shock wave and should be taken into account.

Kurzfassung

In dieser Arbeit werden Schockwellen untersucht, die bei Messungen mit dem Spektroskopieverfahren *Laser-Induced Breakdown Spectroscopy* (LIBS) entstehen. Dabei liegt der Fokus auf LIBS im Kontext der robotischen Erforschung des Mars. Die Kenntnis der chemischen Zusammensetzung von Gesteinsproben ist bei der Erforschung der geologischen Vergangenheit planetarer Körper von zentraler Bedeutung. Änderungen im Klima oder in geologischen Merkmalen wie Flüssen beeinflussen die Zusammensetzung und Struktur von Gestein an der Oberfläche. Die Kenntnis über Komposition und Struktur von Gesteinsformationen oder Geröll erlaubt Rückschlüsse auf geologische Prozesse. Mithilfe des Spektroskopieverfahrens LIBS können die chemischen Bestandteile einer geologischen Probe bestimmt werden. Dabei wird ein Laserstrahl auf die Probenoberfläche fokussiert, woraufhin etwas Probenmaterial verdampft und ionisiert wird. Das entstehende Plasma emittiert ein Spektrum, das charakteristisch für die Zusammensetzung der Probe ist. Während der Messung expandiert das Plasma und erzeugt dadurch eine Druckwelle, die für die Analyse weiterer Probeneigenschaften verwendet werden kann.

Wird mehrmals hintereinander an derselben Stelle gemessen, bildet sich im Laufe der Schussserie ein Krater, der sowohl die Druckwelle, als auch das emittierte optische Spektrum beeinflusst. Die Druckwelle kann mithilfe eines Mikrofons aufgenommen werden, um spektrale Daten zu ergänzen. Akustische Daten können verwendet werden, um die Härte des Materials zu bestimmen und könnten auch für die Normierung spektraler Daten Anwendung finden.

Das Analyseverfahren LIBS wird auf dem Mars bereits bei mehreren wissenschaftlichen Missionen eingesetzt. Nach der erfolgreichen Landung des Perseverance Rovers im Rahmen der Mars 2020 Mission kann nun zum ersten Mal auch die während einer LIBS Messung emittierte Druckwelle aufgenommen werden.

Um Einblicke in die Entstehung des Signals der Druckwelle, die in einiger Entfernung von dem Plasma aufgenommen wird, zu gewinnen, beschäftigt sich diese Arbeit mit der Expansion der Schockwelle kurz nach der Plasmaentstehung in einer simulierten Marsatmosphäre. Hierfür wurde ein optisches System entwickelt und aufgebaut, das die von der Druckwelle verursachten Dichteänderungen abbilden kann. Mithilfe dieser sogenannten Schlierenfotos kann die Dynamik der Schockwellenexpansion untersucht werden. Änderungen der Explosionsenergie im Verlauf einer Schussserie werden in dieser Arbeit analysiert, indem die Daten mit dem Taylor-Sedov-Modell einer Punktexplosion verglichen werden. Nach Wissen des Autors war dies das erste Mal, dass laserinduzierte Schockwellen in diesem Niederdruckbereich und insbesondere in einer simulierten Marsatmosphäre mittels Schlieren fotografien untersucht wurden.

Ein Datensatz aus akustischen Aufnahmen, optischen Spektren und Schlieren fotografien wurde für Proben mit unterschiedlichen Härten, sowie optischen und thermischen Eigenschaften aufgenommen. Der Zusammenhang zwischen Materialhärte und einem Abfall in der akustischen Energie im Verlauf einer Schussserie konnte für die meisten nichtmetallischen Proben bestätigt werden. Ein Vergleich der akustischen und optischen Daten mit der Explo-

sionsenergie ergab, dass die einzelnen Messgrößen auf unterschiedliche Art von den Eigenschaften des jeweiligen Materials beeinflusst werden.

Der Einfluss der Laserenergie und des Atmosphärendrucks auf die Expansion der Schockwelle und das akustische Signal wurden ebenfalls untersucht. Die Explosionsenergie und akustische Energie der Druckwelle zeigte einen linearen Zusammenhang mit der Laserenergie. Änderungen des Umgebungsdrucks wirkten sich kaum auf die Explosionsenergie aus. Mit steigendem Druck stieg die akustische Energie der Druckwelle linear, während die Expansion der Schockwelle verlangsamt wurde. Die aufgenommenen Daten zeigen Veränderungen in der Schockwelle innerhalb des für die Marsoberfläche relevanten Druckbereiches. Änderungen des Umgebungsdrucks im Verlauf eines Tages oder Jahres könnten Daten von der Marsoberfläche signifikant beeinflussen. Ebenso sollten Variationen in der Laserenergie, die aufgrund unterschiedlicher Arbeitsabstände des Lasers für das SuperCam Instrument zu erwarten sind, bei Messungen berücksichtigt werden.

Contents

1. Introduction	1
2. Theory	5
2.1. Laser-Induced Breakdown Spectroscopy	5
2.1.1. Principle	5
2.1.2. Sample Evaporation	6
2.1.3. Plasma Generation and Shielding	8
2.1.4. Plasma Expansion and Absorption Waves	9
2.1.5. Plasma Emission	10
2.2. Pressure Waves	13
2.2.1. Shock Waves	13
2.2.2. Strong Point Explosion	14
2.2.3. Acoustic Waves	16
2.3. Schlieren Imaging	18
2.3.1. Principle	18
2.3.2. Sensitivity	22
2.3.3. Measuring Range	23
2.4. Schlieren Imaging in the Context of Laser-Induced Shock Waves	24
3. Methodology and Setups	27
3.1. Description of the Experiments	27
3.2. LIBS Setup with High Spectral Resolution	29
3.3. Setup with Multiple Diagnostic Tools	29
3.3.1. Laser System and Atmospheric Simulation Chamber	29
3.3.2. Plasma Imaging System	31
3.3.3. Schlieren Imaging System	32
3.3.4. Acoustic Recording System	39
3.4. Samples	40
3.5. Data Processing	41
4. Analysis and Results	43
4.1. Schlieren Imaging	43
4.1.1. Shock Wave Structure	44
4.1.2. Time Series	50
4.1.3. Shot Series	53
4.1.4. Combined Time and Shot Series	56
4.2. Acoustic Measurements of a Shot Series	58
4.3. Spectral Measurements of a Shot Series	62
4.4. Comparison and Discussion of the Signal Changes in a Shot Series	64

Contents

4.5. Influence of Laser Energy and Ambient Pressure on the Shock Wave Expansion	68
4.5.1. Laser Energy	68
4.5.2. Discussion of the Influence of the Laser Energy	68
4.5.3. Ambient Pressure	70
4.5.4. Discussion of the Influence of the Ambient Pressure	71
5. Conclusion and Outlook	73
A. Appendix: Theory	77
A.1. Plasma Properties	77
B. Appendix: Setup	81
B.1. Derivation of the Maximum Angle of Deflection	81
B.2. Schlieren Imaging System	82
C. Appendix: Results	85
List of Figures	85
Bibliography	98

1. Introduction

Since mankind started studying our solar system, the planet Mars has come to play a special role both in public interest as well as in the scientific community for good reason. It is not only close to our home in terms of distance, it is also the planet closest to terrestrial conditions in terms of climate. Learning about Mars' geological history can help us understand this geologically active planet, the history of earth and the solar system.

Mars is also of particular importance to answer the question if life developed only on Earth. The existence of liquid water is crucial to the type of life we know. Research suggests that environmental conditions on Mars used to be close to that of the early Earth and could have supported primitive life. Recently it was found that liquid water likely existed at different points in time of the Martian history and even exists today [29, 40].

Since humanity began exploring the Martian surface with the first successful landers in 1971, technology has advanced significantly and ever more capable remote laboratories have landed, improving our understanding of the planet's past and present. With the successful landing of the Mars 2020 rover Perseverance in Jezero crater, a new suite of instruments to study the Martian surface is available to scientists of different fields [67].

When investigating the geological history of the planet, determining the elemental composition of rocks is a key capability. A changing geological landscape leaves traces in the composition of rock formations on a planet's surface. To study the mineralogy and geochemistry of rocks and soil, Perseverance is equipped amongst others with the sensor suite SuperCam [65]. Aside from Raman, luminescence and infrared reflectance spectroscopy, the SuperCam suite can perform laser-induced breakdown spectroscopy (LIBS) measurements and take high resolution images of the sample. The LIBS system is based on the still actively working ChemCam instrument previously developed for the Mars Science Laboratory known as the Curiosity rover in Gale crater [10, 34]. ChemCam was the first instrument to employ a LIBS system in extraterrestrial research.

When performing a LIBS measurement, the optical emission spectrum of the sample material is acquired by focusing a pulsed laser beam with high intensity on the target. Following a rapid evaporation process, a plasma is formed that emits a spectrum characteristic for the target's elemental composition.

This technique first became available with the development of lasers in the 1960s [13]. In 1992 first studies on the feasibility of this technique in the context of in-situ planetary exploration were presented [27, 28]. A major benefit of LIBS over other techniques is its remote-sensing capability in distances of up to a few meters. When taking a measurement, the instrument does not need to be in contact with the sample, simplifying measurement procedures and opening up more samples to be investigated that are inaccessible to other analytical methods.

Performing a LIBS measurement in an atmosphere results in a shock wave travelling outwards from the targeted area, as the plasma plume expands hypersonically into the ambient gas. Recent studies have shown that this pressure wave can be recorded and used for further scientific analysis of the sample material [7, 8, 19, 41]. When the same spot on a sample is

1. Introduction

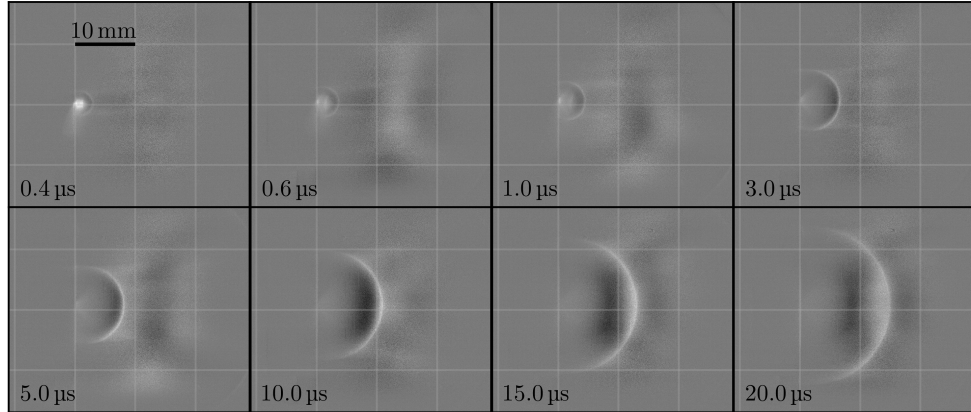


Figure 1.1.: An exemplary measurement of the shock wave expansion from an iron target under Martian atmospheric conditions. The time of recording after plasma ignition is denoted on the bottom left of each frame.

probed with successive laser shots, the acoustic energy carried by the pressure wave changes over the course of the shot series. This change can be correlated to the hardness of the material. Furthermore, the acoustic signal could potentially be used to normalise LIBS spectra in a series of shots, since it could be a proxy for the coupling of the laser radiation with the sample material, which also affects shot-to-shot fluctuations in the LIBS spectra. This scaling is needed, since various parameters influence the emission spectrum in a complex way. In particular, as the repeated laser ablation creates a growing crater in the sample material, the developing crater affects the interactions between the laser and the sample as well as the interaction between the laser and the plasma. The acoustic signal can also be used to find the best focus of the ablating laser beam, as the LIBS signal is brightest when the acoustic energy reaches its maximum [7]. External parameters like the laser energy or the atmospheric pressure influence the acoustic signal, too.

Material properties and external parameters also change the acquired LIBS spectrum, complicating the quantitative analysis of the sample material. The acoustic signal could be used as a tracer for these parameters to better understand and interpret the spectrum.

A microphone to perform acoustic measurements complementary to the acquisition of LIBS spectra is available for the first time on the Mars 2020 Perseverance rover. While some research has been published relating the target's hardness and the ambient pressure to the acoustic energy of the pressure wave at large distances from the target, the dynamics of the shock wave under Martian atmospheric conditions close to the target have not been studied until now.

For this work a schlieren imaging system was designed and built, capable of imaging the density fluctuations caused by a LIBS measurement in a simulated Martian atmospheric environment. The expansion velocity of the shock wave that can be measured with this system is assumed to be correlated with material properties [55]. Exemplary images of the shock wave as it travels through the ambient atmosphere are shown in Figure 1.1 for an iron sample. The goal of the presented study is to investigate the relation between the shock wave dynamics, the pressure wave recorded at large distances from the target and spectral

data.

To correlate the shock wave dynamics with data that is actually available from Mars, acoustic measurements were performed and LIBS spectra were recorded as well. The decoupling of the shock wave from the emitting plasma was investigated using a plasma imaging system that was built for previous studies [59]. A set of schlieren images, acoustic recordings and LIBS spectra was collected for each of the analysed materials. It contains data for iron, lead, gypsum, hematite, magnetite, pyrite and talc. These samples were chosen because of their different material properties, most importantly they span a wide range of hardness.

In Chapter 2, the theoretical background of the relevant physical phenomena is explained. This includes an introduction to the LIBS technique in general, followed by more detailed sections on the generation of the plasma and the resulting LIBS spectrum.

Afterwards, the mechanics of the pressure wave emitted from a LIBS measurement are explained with a detailed description of shock waves and spherically symmetric shock waves in particular. In the limit of small pressure variations, acoustic waves, like those recorded at large distances from the LIBS measurements, are explained as well.

The third section of this chapter is dedicated to the technique of schlieren imaging used to capture the dynamics of the shock wave. An extensive explanation of the general principle is given, followed by a closer look on the sensitivity of the system and its measuring range.

In Chapter 3, the different systems used for the measurements are presented, starting with the LIBS setup used to record spectral data. Afterwards, a brief overview on the plasma imaging system that was used to investigate the decoupling of the shock wave from the plasma is given. A central part of this work was the design of the schlieren imaging system, which is detailed in the next section. Measurements characterising the setup are also presented. The system used to acquire complementary acoustic data to the schlieren images is explained in the following section on acoustic measurements.

In the next two sections, the sample materials investigated in this work are presented and the data processing for the different measurements is explained.

The results are presented in Chapter 4, beginning with the schlieren imaging data. A description of the general shock wave structure is given, followed by an evaluation of the shock wave dynamics. Afterwards, changes to the shock wave that occur during a series of measurements on the same spot are analysed. Finally, the evolution of the plasma dynamics over a series of shots is investigated.

After the schlieren imaging data, the acoustic and spectral measurements are presented and evaluated, followed by a section comparing the evolution of the shock wave dynamics with the acoustic and spectral data over the course of a shot series.

The influence of varying the laser energy and ambient pressure are presented and discussed afterwards.

In the final Chapter 5, the results are summarised and a conclusion is given, as well as an outlook towards further analysis of the shock wave dynamics.

2. Theory

In this chapter, the theoretical aspects of laser-induced shock waves travelling through a homogeneous atmosphere are covered, starting with an overview on laser-induced breakdown spectroscopy. Pressure waves will be discussed with a focus on shock waves, as well as schlieren imaging as a method of recording such pressure waves.

2.1. Laser-Induced Breakdown Spectroscopy

Laser-induced breakdown spectroscopy (LIBS) is a spectroscopic method used in industry and science to determine the elemental composition of samples [21]. In LIBS measurements, a laser is used to evaporate small amounts of material from a target and ignite a small plasma that can be analysed spectroscopically. Multiple elements can be detected simultaneously in rapid measurements that take on the order of one second or less. Since only optical access to the target surface is required and no sample preparation is needed, this method is of particular interest where physical access to the sample can be difficult, like in planetary exploration.

While more challenging than the qualitative analysis of LIBS spectra, measurements of the sample composition can also be evaluated quantitatively, with more accurate algorithms being an active field of research [2].

This section gives an overview on the principle of LIBS measurements, highlighting important mechanisms in the evolution of the plasma and the generation of the LIBS spectrum. All sections focus on mechanisms dominant for ablation with nanosecond laser pulses, since such laser systems are currently used on Mars.

If not stated otherwise, this part is based on the work of Noll [38], Singh and Thakur [52] as well as Cremers and Radziemski [13]. An extensive overview on the LIBS technique and its application in geological studies can be found in [48].

2.1.1. Principle

The principle of taking a LIBS measurement is depicted in Figure 2.1. The indicated times refer to the typical temporal evolution of plasmas ignited with a nanosecond laser pulse under terrestrial atmospheric conditions. A pulsed laser beam is focused on the surface of a sample at $t = 0$ ns, where some of the energy from the incident beam is deposited in the target surface, leading to an increase in temperature.

If the laser irradiance I is sufficiently high, some of the material is vaporised. Part of the laser radiation is absorbed by the vapour, which heats up and gets ionised. The plasma plume becomes more opaque to the incident laser radiation, partially shielding the target surface from it. At this point, the emitted plasma radiation $I_E(\lambda, t)$ is mostly continuous bremsstrahlung and recombination radiation.

The plasma expands hypersonically into the ambient gas, driven by the high pressure p_1 within the plasma, while cooling down. A shock front layer is formed around the expanding

2. Theory

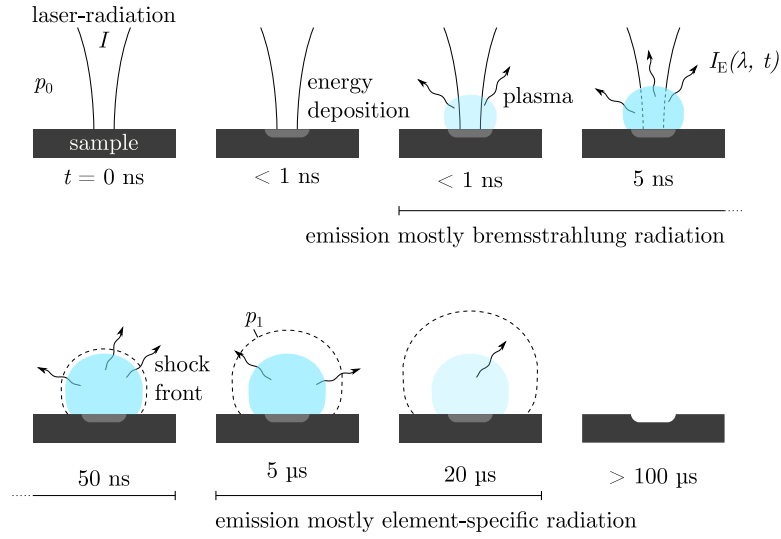


Figure 2.1.: Principle of performing a LIBS measurement with a nanosecond laser on a solid sample under terrestrial atmospheric conditions. The laser beam with irradiance I is focused on the sample surface and vaporises some material, which is heated and turns into a plasma. The plasma partially absorbs the incident laser radiation. It expands while initially radiating continuous bremsstrahlung. As the plasma expands further it cools down and the emission $I_E(\lambda, t)$ is dominated by line emission. During the expansion, a shock wave is formed that continues to travel through the ambient atmosphere and can be recorded using a microphone for further analysis. The listed timescales are taken from [38] and [13].

plasma plume. From this point onward, characteristic line emission constitutes most of the plasma emission $I_E(\lambda, t)$ [13, 38].

The plasma continues to cool down and expand while the shock front is travelling outwards. At this point, the plasma has cooled down sufficiently for molecules to form and emit light from molecular transitions [15, 60]. At around $t \sim 150$ ns, the shock front detaches from the plasma surface, leaving the decaying plasma behind [22].

The plasma begins to fade away and a crater from the ablation process is left behind.

Parameters like the ambient pressure p_0 , the laser wavelength and irradiance I and also the target's optical and thermal properties can have a significant influence on the plasma evolution. Some of these effects will now be discussed in greater detail.

2.1.2. Sample Evaporation

The process of sample evaporation depends heavily on the duration of the laser pulse and the laser irradiance. For nanosecond pulses with an irradiance of less than $I < 10^8 \frac{\text{W}}{\text{cm}^2}$, thermal processes are dominant. If the irradiance is high enough, non-thermal ablation by Coulomb-explosion coexists with thermal processes [52]. The laser irradiance used in this work is on the order of $I \sim 10^9 \frac{\text{W}}{\text{cm}^2}$.

In the following, only thermal processes will be discussed. Thermal processes depend on

macroscopic material parameters that are often available in the literature, while non-thermal processes need to take the electronic structure of the sample into account. Details on non-thermal ablation can be found in [52].

When a solid target material is exposed to sufficiently intense laser radiation, the sample is heated locally above the boiling or decomposition temperature. The evaporation process depends on the fraction of laser radiation absorbed by the sample and on the rate that energy is carried away from the irradiated area by thermal diffusion.

These material properties can be described by the optical penetration depth

$$\delta_{\text{opt}} = \frac{1}{\alpha} \quad (2.1.1)$$

at the laser's wavelength λ as the inverse of the absorption coefficient α and by the thermal penetration depth

$$\delta_{\text{th}} = \sqrt{D\tau} = \sqrt{\frac{k}{\rho C_p} \tau} \quad (2.1.2)$$

at the laser's pulse duration τ , with the material's thermal diffusivity D , the thermal conductivity k , the density ρ and the heat capacity C_p [7]. Apart from the absorption coefficient of the material, its reflectivity R influences the amount of energy absorbed by the sample as well. The optical and thermal penetration depths are visualised in Figure 2.2.

With these parameters, two extreme cases can be investigated [38].

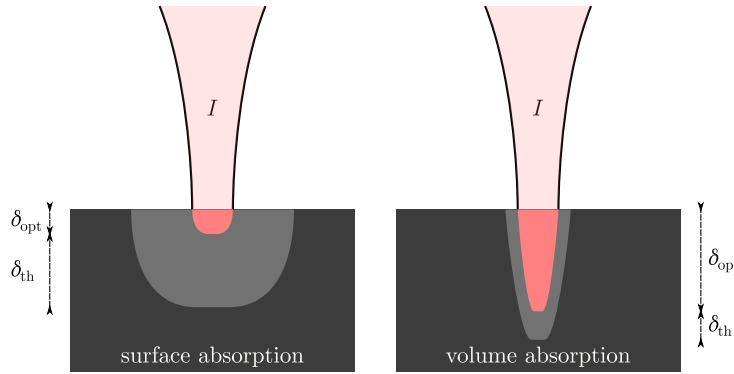


Figure 2.2.: Absorption processes relevant for laser ablation with nanosecond pulses. If the optical penetration depth δ_{opt} is much smaller than the thermal penetration depth δ_{th} , most of the laser radiation I is absorbed close to the sample surface. If the optical penetration depth is much larger than the thermal penetration depth, the laser radiation is absorbed in a larger volume. The figure was inspired by [38].

Surface Absorption $\delta_{\text{opt}} \ll \delta_{\text{th}}$: If the optical penetration depth at the laser's wavelength is much shorter than the thermal penetration depth, most of the incident energy is absorbed in a small volume close to the target's surface and the absorbed irradiance is $AI = (1 - R)I$. This generally leads to a relatively low absorbed irradiance required for evaporation of the

2. Theory

target material. With increasing thermal diffusivity of the material, the necessary irradiance rises. For a given irradiance, the amount of absorbed energy depends also on the duration of the laser pulse.

For laser wavelengths in the visible or infrared range like used in this work, plasma initiation for materials like metals can typically be described by surface absorption.

Volume Absorption $\delta_{\text{opt}} \gg \delta_{\text{th}}$: For a thermal penetration depth much smaller than the optical penetration depth, the energy entering the target $(1 - R)I$ is absorbed over a distance z according to the Beer-Lambert law. The greater volume leads to a higher necessary irradiance when compared to surface absorption processes.

This process is typical for polymers.

The interaction between the sample and the laser radiation affects the amount of ablated material and the properties of the plasma and thus also has an influence on the emission spectrum of the plasma, its dynamics and the shock wave generated during the ablation process [7, 11, 55]. Effects that influence the LIBS spectrum due to changes in the interaction between the laser radiation and the sample are called matrix effects and complicate the quantitative analysis of the sample material.

When the target is probed at the same location with multiple laser shots, the ablation process creates a deepening crater. The changing crater morphology influences the interaction between the laser and the sample for subsequent measurements. As mentioned in Chapter 1, a correlation between the target's hardness and the recorded pressure wave was found, as well as a correlation with the volume of the crater [7]. Knowing these parameters can help interpreting LIBS emission spectra, aid in characterising the sample and could also be used for LIBS data processing procedures such as normalisation.

2.1.3. Plasma Generation and Shielding

When evaporated, the material reaches sufficiently high temperatures so that there are always free electrons that can be accelerated in the laser's radiation field. These electrons can transfer energy to the atoms of the vapour when colliding. The collisions allow the electrons to experience a sufficient net energy gain to further increase the ionisation of the vapour [38]. The plasma is ignited and emits mostly bremsstrahlung radiation at early times.

For the duration of the nanosecond laser pulse, the plasma continues to be heated by absorbing some laser radiation, while part of the radiation is being reflected at the plasma's surface. This effect commonly known as plasma shielding limits the energy released in the focal spot of the laser beam. The absorption coefficient α of the plasma depends on the laser radiation's angular frequency ω , the electron's collision frequency with ions and atoms ν and the plasma frequency ω_p describing the oscillations of the electrons relative to the ions. Apart from constants, the plasma frequency and also the absorption coefficient α depend only on the electron density n_e inside the plasma

$$\omega_p \propto \sqrt{n_e}. \quad (2.1.3)$$

For typical conditions in LIBS plasmas $\nu \ll \omega$ and $\omega_p < \omega$ can be assumed, which leads to the relation

$$\alpha = \frac{\nu}{c} \frac{\omega_p^2}{\omega^2 \sqrt{1 - (\frac{\omega_p}{\omega})^2}} \quad (2.1.4)$$

with the speed of light c [38].

Within the duration of the laser pulse, the plasma becomes ever more opaque to the laser beam in a self-enhancing process. As the electron density grows in the heated plasma, the plasma frequency gets closer to the angular frequency of the laser radiation, leading to a higher absorption and thus increasing the electron density even further. This effect can be seen in Figure 2.3, where the irradiance transmitted through the vapour decreases rapidly after the plasma is ignited due to the higher absorption.

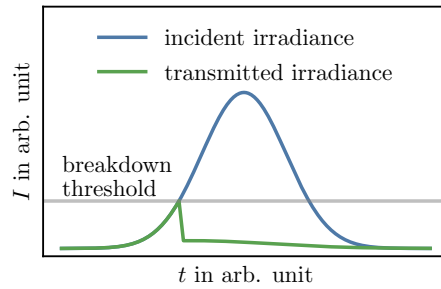


Figure 2.3: Illustration of laser absorption in the plasma. By measuring the laser irradiance I transmitted through a plasma as a function of time t , the effects of laser absorption in the plasma can be studied. The transmitted irradiance drops off quickly as soon as the breakdown threshold for igniting the plasma is crossed. Measurements of the transmitted irradiance can be found in [22] or [52].

The effects of plasma shielding depend on the confinement of the plasma and therefore on the ambient pressure. For low pressure environments like the Martian atmosphere, plasma shielding is reduced, which results in an increase of the mass ablated from the sample material [30].

2.1.4. Plasma Expansion and Absorption Waves

Driven by the high pressure within the hot ionised region, the plasma expands into the surroundings until the pressure of the plasma equalises with the ambient pressure. The expansion of the plasma is slowed down by the surrounding gas pressure, confining the plasma plume. Consequently, the plasma properties depend heavily on the surrounding atmospheric conditions.

While a plasma generated under terrestrial atmospheric conditions is contained in a rather small volume, a plasma in a vacuum dissipates without any confinement effects. This affects the plasma emission and analytical capabilities of the LIBS technique [30].

Apart from the hydrodynamic expansion of the plasma due to its high pressure, the volume of the ionised region above the sample surface grows with time because more of the incident laser radiation is absorbed and the surrounding gas is heated. The increasing ionisation and electron number density lead to an absorption wave travelling in the direction of the laser

2. Theory

beam. Three independent mechanisms can be identified explaining this absorption wave travelling outwards from the initial plasma spark [22, 69]. All these mechanisms contribute to the shielding of the sample surface from laser radiation.

Laser Supported Breakdown Wave If the incident radiant energy flux is well exceeding the breakdown threshold at the focal spot, this threshold will also be crossed over a certain length away from the target surface. Since the radiant flux is lower at larger distances from the target due to the wider laser beam, breakdown occurs later, leading to a breakdown wave travelling towards the laser beam. This is known as a laser supported breakdown wave.

Laser Supported Detonation Wave The laser radiation initially ionises a small layer of gas which expands, sending out a shock wave in all directions of the surrounding gas. While the shock front is travelling through the gas it heats and ionises the medium, leading to an optically thick layer across the shock front, where laser radiation is absorbed. This mechanism is similar to detonation processes, which are governed by laws described in Section 2.2. Accordingly, this mechanism is known as the laser supported detonation wave.

Laser Supported Radiation Wave High energy radiation emitted from the plasma plume can heat and ionise the surrounding gas, leading to an optically thick layer where laser radiation can be absorbed. This mechanism is called laser supported radiation wave.

In [22], the absorption wave mechanism during the laser pulse was shown to lead to a plasma shape elongated in the direction of the incident laser beam. Since the time scales investigated in this thesis are much larger than the duration of the laser pulse, for this work these mechanisms are mostly relevant in terms of their potential to ionise the surrounding gas after the laser pulse is over. For this reason, the laser supported breakdown wave is not expected to have a significant impact on the presented data in terms of plasma expansion. Effects attributed to the radiation wave mechanism are relevant in the early stages of the plasma expansion [22]. At later stages, the detonation wave was found to play an important role for the laser irradiances used for this work [59].

2.1.5. Plasma Emission

The radiation emitted by the plasma $I_E(\lambda, t)$ changes with time t , as the dominant underlying processes change. This temporal change in the emission spectrum is illustrated in Figure 2.4. The timescales noted in the following refer to a plasma generated in a terrestrial atmosphere by a nanosecond laser pulse [13, 38].

At early times $t_0 \sim 100$ ns after plasma ignition, the spectrum is dominated by a continuous background emission resulting from bremsstrahlung and recombination radiation. As the plasma cools down at around $t_1 \sim 1$ μ s, these processes become less relevant and the spectrum is dominated by characteristic line emission. With the decaying plasma, the emission also fades away at $t_2 \sim 100$ μ s. For plasmas in a Martian atmosphere, these timescales are reduced and the lifetime of the plasma is about 10 μ s [45, 47].

Bremsstrahlung and Recombination Radiation In the early stages of the plasma, most of the emission results from electrons moving in the Coulomb field of the ions or recombining

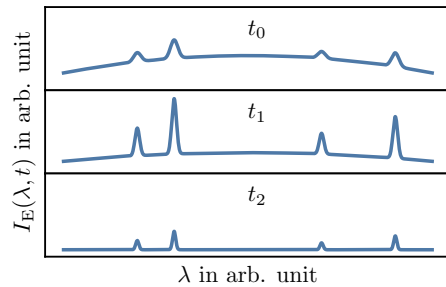


Figure 2.4.: Plasma emission intensity $I_E(\lambda, t)$ as a function of wavelength λ and its changes over time t . The early spectrum at t_0 is dominated by continuous emission from bremsstrahlung and recombination radiation. As the plasma cools down, line emission from the species within the plasma becomes dominant at t_1 and the line widths are reduced. When the plasma begins to fade away, so does the line emission at t_2 . The figure was inspired by [38].

with them, resulting in bremsstrahlung and recombination radiation. This can be seen at t_0 in Figure 2.4, where the spectrum is dominated by a continuous background emission.

The emission from these processes decreases much faster than the line emission from excited atoms and ions used for elemental characterisation [38]. For this reason, it is often favourable to start plasma recording after most of the background emission has decayed at t_1 .

Line Emission In LIBS measurements, atomic, ionic and at later stages also molecular line emission is used to assess the target's composition [59, 60]. Spontaneous emission is the primary process leading to characteristic line emission. The excitation of the plasma's constituents is dominated by collisions with electrons. Photoexcitation processes can change the appearance of the spectra, especially through self-absorption.

All excitation processes relevant for LIBS plasmas are dominated by interactions with free electrons [14]. For this reason, the knowledge of the electron density n_e is of great importance when deriving element concentrations from recorded spectra in a calibration-free LIBS analysis [9].

The conditions within the plasma affect the LIBS spectrum and depend on many external parameters like the ambient pressure p_0 and the laser irradiance $I_{\lambda L}^i$ at wavelength λ . The exact position of the laser focus Δs and the size of the focus w change the properties of the plasma as well.

Some of the most relevant parameters influencing the plasma emission $I_E(\lambda, t)$ are shown in Figure 2.5. These include the number density N_a^z of the species a with ionisation state z under investigation and the plasma temperature T [38]. All of these parameters depend on the position \mathbf{r} within the plasma and the time after the laser pulse t . A description of some plasma properties and how they influence LIBS spectra can be found in the appendix in A.1.

The intensity and shape of the collected emission spectrum is affected by the pressure and composition of the surrounding atmosphere [3, 16, 30]. If the ambient pressure is reduced below terrestrial atmospheric pressure, the signal to noise ratio and spectral resolution gen-

2. Theory

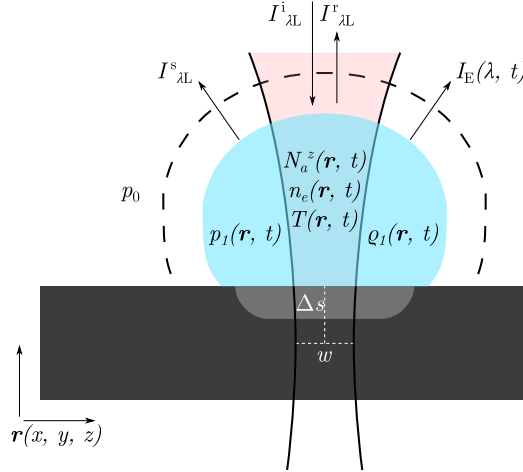


Figure 2.5.: Overview of the most relevant laser parameters and plasma properties. The plasma is ignited in an atmosphere with a pressure p_0 by a laser with irradiance $I_{\lambda L}^i$. The exact position Δs and size w of the laser focus influence the plasma properties. Some of the incident radiation is reflected $I_{\lambda L}^r$ or scattered $I_{\lambda L}^s$. The spectrum emitted from the plasma depends on the number density of the species under investigation N_a^z , the electron number density n_e and the plasma temperature T . All of these parameters depend on the position within the plasma \mathbf{r} and change with time t . The expansion of the plasma is governed by its thermodynamic properties T , p_1 and ρ_1 . The figure was inspired by [38].

erally improve, due to reduced plasma shielding and line broadening. At very low pressures under $p_0 \sim 10$ kPa, the LIBS signal usually weakens as the confinement of the plasma by the ambient atmosphere is reduced. The Martian atmospheric pressure with $p_0 \sim 0.7$ kPa presents a close to ideal environment for LIBS measurements, as plasma shielding effects are relatively low while the confinement of the plasma by the atmosphere leads to a strong LIBS signal [3, 16, 30].

For a quantitative analysis of LIBS spectra, a calibration model that is built from data of reference samples with known concentrations measured under similar conditions is often used, which comes with some challenges [21]. Differences in a target's composition might not only influence the line intensities of the transitions from one specific element, but can also influence the intensity of other species' lines. For example, if an element with a low ionisation energy is present in the plasma, the equilibrium between the amount of ions and neutral atoms can be influenced, changing the emission spectrum. Such a change in the spectrum due to the chemical composition of the target is referred to as chemical matrix effects. This is in addition to effects that the target's physical structure has on the laser-coupling, like its roughness or dust depositions on the surface of the sample. These effects also influence the LIBS spectrum and are referred to as physical matrix effects [13].

To reduce shot-to-shot variability partially due to the influence of matrix effects in LIBS spectra, the data is usually normalised. Different approaches are described in the literature, including normalising to a specific line's intensity, the total spectral intensity or plasma parameters such as its temperature. However, the reliability of these normalisation methods to correct for matrix effects is limited, in particular if additionally experimental parameters

are not stable, as is the case for robotic applications such as SuperCam [43].

The method of calibration-free LIBS avoids problems arising from matrix effects by calculating the chemical composition directly from the line intensities without the need of calibration data. It constitutes an extensive computational task and comes with its own challenges, as the knowledge of the plasma's temperature and electron density is required. More information on this quantitative method can be found in [21].

The crater resulting from repeated LIBS measurements at the same position changes the interaction between the laser and the sample, influencing not only the plasma properties and emission, but also the pressure wave emitted from the expanding plasma plume.

2.2. Pressure Waves

When a LIBS plasma is ignited, the energy deposited by the absorbed laser radiation gives rise to a steep increase in temperature and pressure, driving the plasma to expand supersonically into the ambient gas [5, 22, 51]. This expansion leads to a shock wave travelling outwards from the ablated area. The pressure wave slows down and weakens as it travels through the ambient gas. As the propagation velocity approaches the speed of sound c , the shock wave transitions to an acoustic wave [69].

Recent studies have shown that the acoustic energy E_a carried by the acoustic wave can give insight into material properties of the target under investigation and the laser ablation process [7, 19, 33]. Features in the frequency spectrum of the pressure wave were related to effects of plasma shielding [41].

In this work, the propagation of the supersonic shock wave close to the sample will be analysed, as well as the energy of the acoustic wave at larger distances. The following theoretical explanations are based on [69] except if noted otherwise.

2.2.1. Shock Waves

Shock waves can be thought of as pressure waves with a discontinuous change of the pressure p , density ρ and gas velocity u in front and behind the moving disturbance. This situation can arise, if a piston starts moving with a constant velocity u_1 into an initially resting ideal gas with p_0 , ρ_0 and $u_0 = 0$. If the piston is accelerating instantly to its constant velocity, the only physically meaningful solution to the gasdynamic equations requires the existence of a discontinuity, in front of which the gas is still in its initial state p_0 , ρ_0 and u_0 . Behind the discontinuity however, the gas is moving at the piston's velocity u_1 . This situation is depicted in Figure 2.6.

Applying the laws of conservation of mass, momentum and energy, the pressure p_1 , density ρ_1 and the specific enthalpy h_1 behind the discontinuity can be found.

$$\text{mass} \quad \rho_1 u_1 = \rho_0 u_0 \quad (2.2.1)$$

$$\text{momentum} \quad p_1 + \rho_1 u_1^2 = p_0 + \rho_0 u_0^2 \quad (2.2.2)$$

$$\text{energy} \quad h_1 + \frac{u_1^2}{2} = h_0 + \frac{u_0^2}{2} \quad (2.2.3)$$

The velocities u_i represent the speed of the gas, at which it is travelling into or out of the discontinuity.

2. Theory

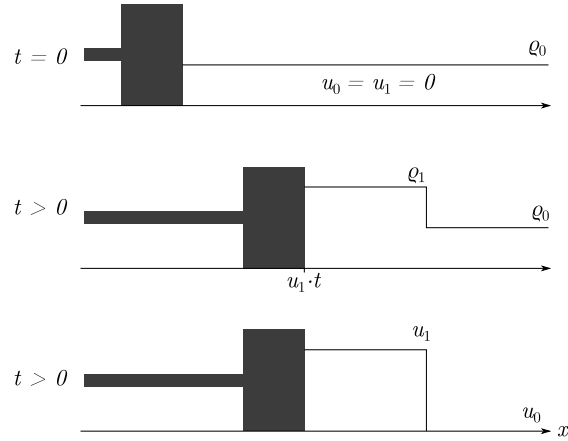


Figure 2.6.: Illustration of a plane shock wave produced by a piston. Initially, the gas of density ρ_0 is at rest, so $u_0 = u_1 = 0$. At $t > 0$ the piston starts moving instantaneously into the gas with the velocity u_1 . A discontinuous density change emerges with a high density region ρ_1 behind the shock front. The gas behind the shock front moves with the same velocity u_1 as the piston while the ambient gas in front of the shock is still at rest $u_0 = 0$. The figure was inspired by [69].

Considering these equations and relating the specific enthalpy and energy $\epsilon = h - \frac{p}{\rho}$ to the gas' specific heats $\gamma = \frac{c_p}{c_v}$, one can find the density ratio in front and behind the discontinuity

$$\frac{\rho_1}{\rho_0} = \frac{V_0}{V_1} = \frac{\gamma + 1}{\gamma - 1} \quad (2.2.4)$$

for the limiting case of $p_1 \gg \frac{\gamma+1}{\gamma-1} p_0$. This means that for a shock wave travelling through a CO₂ atmosphere with $\gamma = \frac{9}{7}$, the ratio of the densities behind and in front of the shock is $\frac{\rho_1}{\rho_0} = 8$.

Viscosity and heat conduction can be included in the description by considering collisions between the gas particles. Taking these effects into account leads to a description of the dissipation of sound wave energy through irreversible processes and lets one assess the thickness of the shock front layer.

If either heat conduction or effects of viscosity are present, the thickness of the shock front layer can be estimated to be

$$\Delta x \sim l \frac{p_0}{p_1 - p_0} \quad (2.2.5)$$

with the mean free path l of the gas particles in the shock layer.

2.2.2. Strong Point Explosion

One problem of particular interest for shock waves generated by laser-induced plasmas is that of a strong point explosion in a homogeneous atmosphere. When a large amount of energy E is released instantaneously in a small volume, a spherical shock wave will travel outwards from the point of the explosion, as is the case for LIBS plasmas.

If the counterpressure p_0 from the surrounding atmosphere is assumed to be sufficiently small and if a perfect gas with constant specific heats and a constant density ρ_0 is assumed, the solution to this problem is a self-similar flow, where all flow variables $u(r, t)$, $c(r, t)$, $\rho(r, t)$, $p(r, t)$ are functions of a particular combination of the coordinate variable r and the time variable t .

Since the only two relevant parameters in this approximation E and ρ_0 can not be combined to yield either a length or a time scale, the motion has to be self-similar and thus depend on a particular combination of E and ρ_0 . The only combination of the energy and the density variables containing only the dimensions length and time is their ratio

$$\left[\frac{E}{\rho_0} \right] = \frac{\text{m}^5}{\text{s}^2}.$$

From this, one can construct the dimensionless quantity

$$\xi = r \left(\frac{\rho_0}{E t^2} \right)^{\frac{1}{5}} \quad (2.2.6)$$

that can act as the similarity variable.

This variable determines the distribution of the flow variables at the position r with respect to the radius R of the shock wave and can be written as $\xi = \xi_0 \frac{r}{R}$. The position of the shock front can then be calculated for $r = R$ from

$$R(t) = \xi_0 \left(\frac{E}{\rho_0} \right)^{\frac{1}{5}} t^{\frac{2}{5}}. \quad (2.2.7)$$

It can be shown that ξ_0 depends only on the gas' specific heat ratio γ . This description of a spherical shock wave expansion is known as the Taylor-Sedov model. Similar equations can be derived for cylindrical symmetry and the case of a plane wave.

The pressure behind the shock front also depends on the similarity variable and can be calculated from the shock front velocity $D(t) = \frac{dR}{dt}$ in the limit of a strong shock $p_1 \gg \frac{\gamma+1}{\gamma-1} p_0$ from

$$p_1 = \frac{2}{\gamma+1} \rho_0 D^2. \quad (2.2.8)$$

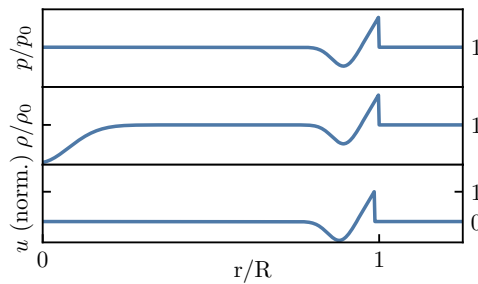


Figure 2.7.: Distribution of the pressure p , density ρ and velocity gas u for a weak shock wave in a atmosphere of pressure p_0 and density ρ_0 as a function of the position r relative to the shock front position R . The pressure and density distributions are normalised to the background levels, while the velocity distribution is normalised to its maximum. The discontinuous compression phase is followed by a rarefaction wave. The figure was inspired by [69].

2. Theory

As the shock wave travels outwards and slows down, the pressure p_1 behind the shock front decreases with the square of the propagation velocity D . When the pressure in the central region of the explosion becomes comparable to the ambient pressure p_0 , the expansion of the gas in the central region stops and only the gas around the shock front continues to move. The approximation of a strong shock $p_1 \gg \frac{\gamma+1}{\gamma-1} p_0$ is no longer valid and the spherical pressure wave is now of acoustic type. The compression zone behind the shock front of such a wave is followed by a distinct rarefaction zone. Both travel together into the ambient gas. The spatial distributions of pressure p , density ρ and velocity u of this weak shock wave are shown in Figure 2.7. In the center of the explosion the density is lowered. Further away from the center it rises to the level of the ambient gas. The density is lowered again in the rarefaction wave and increased in the compression wave.

When the strong shock approximation no longer holds, the solution to this problem is no longer self-similar, as it now contains characteristic scales. A characteristic length for example can be constructed from

$$r_0 = \left(\frac{E}{p_0}\right)^{\frac{1}{3}}. \quad (2.2.9)$$

After the pressure wave transitions to an acoustic wave, its movement can be described by

$$R = ct \quad (2.2.10)$$

with the speed of sound c .

2.2.3. Acoustic Waves

When considering small disturbances in density $\Delta\rho$ and pressure Δp of a gas, the solution to the gasdynamic equations provides their propagation velocity. This velocity is the speed of sound c and can be calculated from

$$c = \sqrt{\frac{\gamma RT}{M}} \quad (2.2.11)$$

for an ideal gas, which will be assumed for the following paragraphs, with the specific heat ratio γ , the universal gas constant R , the temperature T and the molecular weight M . Effects of heat conduction and viscosity will also be neglected.

Plane Wave For the case of a plane acoustic wave, any arbitrary initial disturbance $\Delta\rho(x, t = 0)$ will travel unchanged in shape and with a constant amplitude through the medium, as required by the wave equation governing the movement

$$\frac{\partial \Delta\rho}{\partial t^2} = c^2 \frac{\partial^2 \Delta\rho}{\partial x^2}. \quad (2.2.12)$$

The general solution to the wave equation consists of two particular solutions, travelling in both directions $+x$ and $-x$

$$\Delta\rho(x, t) = \frac{\rho_0}{c} f_1(x - ct) + \frac{\rho_0}{c} f_2(x + ct) \quad (2.2.13)$$

with the arbitrary functions

$$\begin{aligned} f_1 &= \frac{1}{2} \left(\frac{c}{\rho_0} \Delta\rho(x, t=0) + u(x, t=0) \right) \\ f_2 &= \frac{1}{2} \left(\frac{c}{\rho_0} \Delta\rho(x, t=0) - u(x, t=0) \right) \end{aligned}$$

of the initial density and velocity distributions $\Delta\rho(x, t=0)$ and $u(x, t=0)$.

One solution of particular importance for acoustics is the case of the monochromatic sound wave

$$\Delta\rho(x, t) = A \cos\left(\frac{\omega}{c}x - \omega t\right)$$

with the angular frequency ω .

Spherical Wave In the case of spherical symmetry, the appropriate wave equation delivers a solution, where the amplitude of the travelling density disturbance $\Delta\rho(r, t)$ at a distance r from the center decreases with

$$\Delta\rho = \frac{f(r-ct)}{r} \quad (2.2.14)$$

as it moves away from the center. In both the plane and the spherical case of acoustic waves, the change in pressure is proportional to the change in density $\Delta\rho \propto \Delta p$.

Using the solution for $\Delta\rho$ in the equation of motion for the spherical case reveals that a compressive wave of high density and pressure must be followed by a rarefaction wave so that the integral across the entire region of disturbance becomes zero to satisfy the boundary conditions. This can also be seen in Figure 2.7.

When the disturbances are not sufficiently small, the shape of the travelling wave will gradually change. This is because the speed of sound at the crest of the wave is slightly higher than the speed of sound at the valley of the wave.

In this work, the energy of acoustic waves emitted from a LIBS plasma will be analysed. The energy density U of an harmonic acoustic wave is given by [66]

$$U = \frac{1}{2} \frac{\Delta p^2}{\rho_0 c^2}. \quad (2.2.15)$$

Similar to previous works studying the connection between the acoustic energies of sound waves in LIBS measurements, the quantity

$$\hat{E}_a = \int \Delta p^2 dt \propto E_a, \quad (2.2.16)$$

will be analysed. It includes information about the waveform and is proportional to the acoustic energy E_a [7, 19, 41].

2.3. Schlieren Imaging

Density gradients like those occurring in pressure waves emitted from an expanding LIBS plasma can be made visible using the schlieren imaging technique. The local change in a gas' density influences its refractive index n . This effect can be used to image local gradients in the refractive index $\frac{\partial n}{\partial x}$ of a gas called a schlieren object in the following.

As pointed out above, the acoustic energy carried by a pressure wave induced by a LIBS plasma can reveal material properties of the target. However, the link between the pressure recorded at large distances from the LIBS target and the shock wave properties close to the target has not been studied yet. Schlieren imaging can be used to investigate the dynamics and properties of the pressure wave formed by a LIBS plasma at short distances.

If not noted otherwise, the following section is based on [49]. Any radiation losses from optical components or from schlieren objects shall be neglected for the purpose of this section.

2.3.1. Principle

Changes in the density ρ of a gas influence the gas' refractive index n as described by the linear Gladstone-Dale relation

$$n - 1 = k \rho \quad (2.3.1)$$

with the gas and wavelength dependent Gladstone-Dale coefficient k .

Light rays travelling in the direction z can be deflected in the perpendicular directions x and y by a schlieren object. For a disturbance of length L along the optical axis z , the angles of deflection θ_x towards x and θ_y towards y can be calculated from

$$\theta_x = \frac{L}{n_0} \frac{\partial n}{\partial x} \quad \text{and} \quad \theta_y = \frac{L}{n_0} \frac{\partial n}{\partial y} \quad (2.3.2)$$

in an atmosphere of refractive index n_0 .

Distinction of Shadowgraphing For a schlieren object illuminated by a light source, these deflections cause variations in brightness when the transmitted rays are viewed on a screen as depicted in Figure 2.8. Here, the schlieren object is a sphere with higher refractive index than its surroundings. It is illuminated by parallel light rays collimated by a lens and the transmitted light is viewed on a screen.

Light rays hitting the sphere's center are not deflected at all, since the local gradients vanish. The change in refractive index in the center occurs only in the direction of the optical axis z . Moving up or down from the center of the sphere, the gradients perpendicular to the optical axis change and the rays get deflected. The strongest deflection occurs just at the boundary between the sphere and the surrounding gas at the top where the gradient is highest.

Shadowgraphs can only be taken if the object has a varying gradient in refractive index, so the second spatial derivative $\frac{\partial^2 n}{\partial x^2}$ or $\frac{\partial^2 n}{\partial y^2}$ must not be zero. A schlieren object with uniform gradient would shift the entire beam without disturbing it.

The visible change in brightness recorded on the screen does not only depend on the refractive index of the schlieren object, but also on the distance of the screen from the object. No sharp image of the object's refractive index change can be produced with this technique, hence the name shadowgraphing.

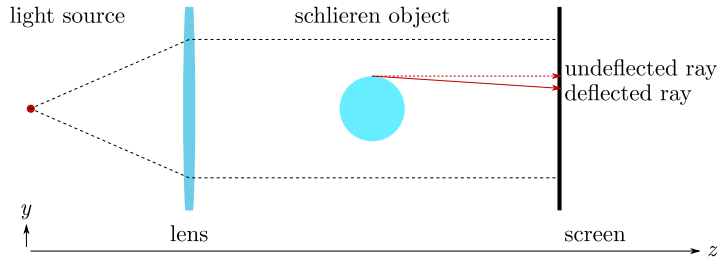


Figure 2.8.: Principle of shadowgraphing measurements. A schlieren object is illuminated by collimated light from a point light source. Changes in the refractive index cause the light rays to be deflected and hit the screen at a different position. Since no imaging optics are used, no sharp image of the schlieren object is produced. The figure was inspired by [49].

Schlieren Imaging In contrast to shadowgraphing, the schlieren imaging technique employs additional optical elements, resulting in a sensitivity to the gradient of the refractive index $\frac{\partial n}{\partial x}$ and $\frac{\partial n}{\partial y}$ and in a sharp image of the schlieren object.

A variety of different shadowgraphing and schlieren imaging techniques are discussed in [50]. In this work, a classic Toepler's lens-type schlieren system is used that is shown schematically in Figure 2.9. Instead of intersecting the transmitted and partially deflected rays at some distance with a screen like in the shadowgraphing setup in Figure 2.8, the schlieren imaging apparatus uses a focusing and an objective lens to image the actual schlieren object. Apart from the benefit of a sharp image of the object under investigation, this also allows for the image size to be adapted to the experimental environment and independently of the field of

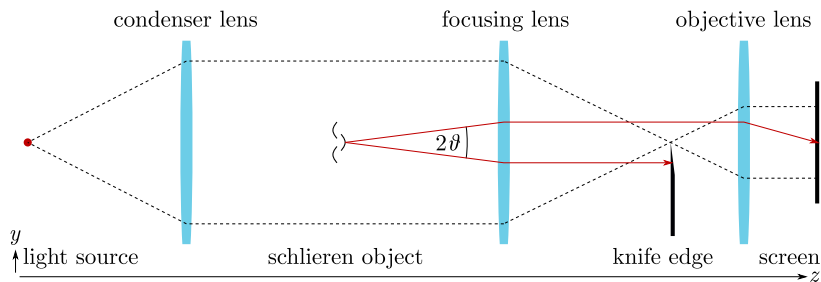


Figure 2.9.: Principle of schlieren imaging measurements. A schlieren object is illuminated by the collimated light from a point light source. The schlieren object causes the deflection of some light rays that consequently miss the focal point of the focusing lens. By introducing a knife edge in the focal plane of the focusing lens, deflected light rays can be filtered, resulting in a contrast on the screen. The use of an objective lens allows for a sharp image of the schlieren object to be produced. The figure was inspired by [49].

2. Theory

view.

In Figure 2.9, the schlieren object is illuminated by the collimated rays of a point light source. Two scenarios are shown here. A ray hitting the schlieren object can be deflected upwards or downwards by an angle θ . Subsequently, in both scenarios the ray misses the focal point of the focusing lens, while undisturbed rays pass through the focal point. Since the combination of focusing and objective lens is mapping each point from the schlieren object to a point on the screen, the deflected rays still arrive at the same point as if they would not have been deflected.

However, if a knife edge is introduced like in Figure 2.9, only rays deflected upwards can pass the imaging optics, while rays deflected downwards are blocked by the knife edge. In the scenario of a point light source, the background illumination is either on or off. Depending on the exact placement of the knife edge, the undisturbed light rays either all pass the knife edge resulting in a bright background illumination or all are blocked and the background is not illuminated. In this simplified scenario with a point light source, the contrast in the schlieren image is either a result of light rays being blocked in the case for a bright background or a result of light rays passing the knife edge in the case for a dark background.

This effectively means that the sensitivity S of this apparatus is infinite so that the smallest change in refractive index causes a maximum contrast C , while the measuring range θ_{\max} is zero, so different gradients in the refractive index don't cause a difference in illumination.

While this scenario is good for an illustration of the principle, it is clearly neither realistic nor practical.

The same apparatus with a more realistic extended light source is shown in Figure 2.10. In the focal plane behind the focusing lens, an image of the extended light source appears. Depending on the exact position of the knife edge, part of this image is blocked and thus the background illumination can be anywhere between full brightness and darkness. The ratio of the background brightness to the maximum possible brightness is called cutoff. For the scenario depicted in Figure 2.10 it is 50 %, as the knife edge is positioned exactly in the middle blocking half of the light.

Since the light source now has a finite size, the rays illuminating the schlieren object are not perfectly parallel. This introduces the effect of a depth of focus to the schlieren apparatus.

To understand the role of each lens and the knife edge, it is helpful to consider the system under the aspect of Fourier optics. The planes of the light source and the knife edge form conjugate optical planes, so changes in one plane appear undistorted in the other plane, except for a possible change in scale. A second set of conjugate optical planes are the planes of the schlieren object and the screen. These two sets are related to each other by a reciprocal Fourier transform.

The image of the light source in the knife edge plane can now be considered as a superposition of many separate images passing through the test area of the schlieren object. Since the two sets of planes are connected by the Fourier transform, blocking part of the light source's image will uniformly reduce the background illumination on the screen. The knife edge acts as a phase filter for the image of the schlieren object.

So far, no displacement of light rays by the schlieren object has been considered. It is important to understand that in each set of light rays passing through a point in the test plane, the entire information of the light source image is contained. When light is deflected by a refractive index gradient of the schlieren object, the bundle of light rays is deflected by

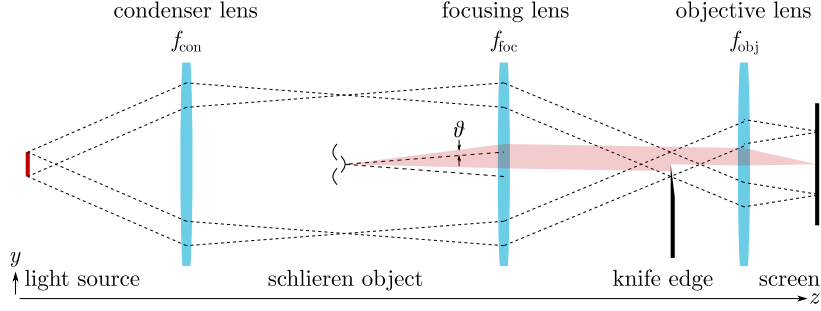


Figure 2.10.: Sketch of a realistic Toepler's lens-type schlieren system with an extended light source. The extended light source introduces a depth of focus effect to the schlieren images. A bundle of light rays is deflected upwards by an angle θ , shifting the bundle upwards. Consequently, a larger part of the light rays passes the knife edge when compared to the undisturbed background illumination. The point in the image of the schlieren object corresponding to the point of deflection is now brighter than the background. The figure was inspired by [69].

an angle θ . This is depicted in Figure 2.10, where the dashed line shows the path of the bundle without deflection and the red coloured area describes the actual path of the light ray bundle.

If no knife edge was present, no contrast would be achieved, as the displaced ray bundle hits the screen at the same relative position from where it came in the test plane. As is clear from Figure 2.10, when the knife edge is introduced, a smaller fraction of the light coming from the schlieren object is blocked by the knife edge when compared with the undisturbed light. This results in a brightening of the position of deflection in the schlieren image. If the deflection by the schlieren object would be downwards, a larger portion of the light would be blocked when compared to the background illumination, resulting in a darkened area.

This leads to a gradual change in brightness depending on the deflection angle θ until a maximum angle θ_{\max} is reached, where all or none of the deflected ray bundles are blocked by the knife edge. For small angles, the displacement of the light source image Δa in the focal plane of the focusing lens can be calculated from

$$\Delta a = f_{\text{foc}} \cdot \tan \theta_{\perp} \approx f_{\text{foc}} \cdot \theta_{\perp} \quad (2.3.3)$$

with the deflection angle θ_{\perp} perpendicular to the knife edge and the focal length f_{foc} of the focusing lens*. Figure 2.11 shows the image of a rectangular light source of width b and height h in the focal plane of the focusing lens. Note that the image width b_i and height h_i are only the same as the light source width b and height h if the condenser and focusing lens have equal focal lengths.

It is now clear that the irradiance E of a point in the schlieren image is proportional to the refraction angle θ_{\perp} for small angles, and is consequently also proportional to the refractive index gradient at the corresponding point in the schlieren object according to equations 2.3.2.

*The angle θ_{\perp} is measured upwards from the optical axis. For the purpose of this work, $\theta_{\perp} = \theta_y$.

2. Theory

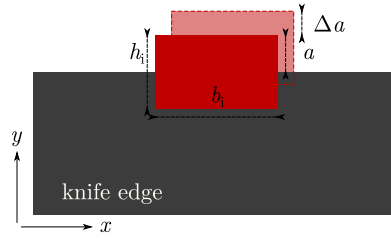


Figure 2.11.: Sketch of the light source image in the focal plane of the focusing lens at $R = 50\%$ cutoff. The image produced by undisturbed light rays is shown in dark red. The part $a \cdot b_i$ of this image is responsible for the background illumination of the schlieren image. If a bundle of rays is deflected, this produces a light source image shifted by Δa . In the case depicted here, this results in a brightening of the region where the rays were deflected, as a greater part of the light source image can pass the knife edge. The figure was inspired by [69].

Without displacement by a schlieren object, the part a of the image can pass the knife edge unobstructed while the rest is being blocked. The cutoff R of a system with a rectangular light source that is parallel to the knife edge can thus be calculated from the ratio of a to h .

$$R = 1 - \frac{a}{h} \quad (2.3.4)$$

2.3.2. Sensitivity

The sensitivity S of a schlieren apparatus relates the deflection angle θ induced by a schlieren object to the resulting change in brightness. To calculate it, we shall consider a light source with radiance L_e , delivering the irradiance

$$E'_e = \frac{L_e \cdot b \cdot h}{f_{\text{con}}^2} \quad (2.3.5)$$

to the condensor lens with focal length f_{con} . The same radiant flux is received by the focusing lens and, in the absence of a knife edge, the same flux is irradiating the sensor recording the schlieren image, except for some magnification factor m .

$$E''_e = \frac{L_e \cdot b \cdot h}{m^2 f_{\text{con}}^2} \quad (2.3.6)$$

If the knife edge is placed in the optical path like in Figure 2.11, only the part $b_i \cdot a$ of the light source image can pass the knife edge. The actual unobstructed height of the light source imaged on the knife edge is then $\frac{f_{\text{con}}}{f_{\text{foc}}} a$ and the background irradiance on the sensor is

$$E_e = \frac{L_e \cdot b \cdot a}{m^2 f_{\text{con}} f_{\text{foc}}}. \quad (2.3.7)$$

This background irradiance E is the reference value to which any change in brightness induced by refractive index gradients is compared. Lower brightness represents a negative gradient, while a higher brightness displays a positive gradient. No change in brightness

shows that the gradient is zero.

If a schlieren object is present, it can deflect a light ray bundle by some angle θ as shown in Figure 2.10 with some component in the direction perpendicular to the knife edge θ_{\perp} , which in this case is the y -direction. According to Equation 2.3.3, this results in a shift of the light source image Δa . Substituting Equation 2.3.3 for a in Equation 2.3.7 shows that the according change in irradiance is

$$\Delta E_e = \frac{L_e \cdot b \cdot \theta_{\perp}}{m^2 f_{\text{con}}}. \quad (2.3.8)$$

The relative change in brightness compared to the background illumination is called contrast

$$C \equiv \frac{\Delta E_e}{E_e} = \frac{f_{\text{foc}} \theta_{\perp}}{a}. \quad (2.3.9)$$

Taking the derivative with respect to the angle of deflection, we arrive at the sensitivity of the schlieren apparatus

$$S = \frac{dC}{d\theta} = \frac{f_{\text{foc}}}{a} \quad (2.3.10)$$

that depends only on the focal length of the focusing lens and the size of the light source[†].

Orientation of the Knife Edge From Figure 2.11 it is clear that the contrast achieved with a schlieren apparatus depends on the orientation of the knife edge. A change in brightness can only be seen in the direction perpendicular to the knife edge. Brighter regions relate to a positive refractive index gradient measured in the direction away from the knife edge. In Figure 2.10 this means upwards towards $+y$.

If contrast in both x and y directions is needed, two images can be taken with perpendicular knife edge orientations. One can also combine knife edges into the shape of the letter L or use a pinhole as a phase filter. Details on other types of filters can be found in [49]. For this work, only contrast in the y direction is necessary.

2.3.3. Measuring Range

As mentioned earlier, a gradual change in contrast is only possible for angles θ where part of the image transported by a deflected light ray bundle is blocked by the knife edge. If all or none of the deflected rays are blocked, any further change in θ will have no effect on the contrast.

The measuring range describes the instrument's ability to resolve gradual changes in deflection angles. For a system with a cutoff of $R = 50\%$, half of the light from the light source is blocked and $a = \frac{h_i}{2}$. Rearranging Equation 2.3.9 yields the maximum angle of deflection $\theta_{\perp\text{max}}$ that can be resolved.

$$\theta_{\perp\text{max}} = \frac{\Delta E_e}{E_e} \frac{h_i}{2 f_{\text{foc}}} \quad (2.3.11)$$

In the case of 50% cutoff, the measuring range is equal for positive and negative refractive index gradients. If any other cutoff is chosen, the measuring range will be different for

[†]The previously discussed case of a point light source is included, as $S \rightarrow \infty$ for $a \rightarrow 0$.

positive and negative refractive index gradients.

2.4. Schlieren Imaging in the Context of Laser-Induced Shock Waves

As described in the previous sections 2.1 and 2.2, taking a LIBS measurement in an atmosphere results in a hemispherical shock wave travelling outwards from the point of ablation. This work aims to investigate the connection between the signal from the acoustic waves at large distances from the sample and the shock front dynamics close to the target surface. Of particular interest is the transition of the supersonic shock wave to a sonic pressure wave of acoustic type.

Several different methods are employed to analyse the pressure wave that will be discussed in the next chapter. The main focus of this work lies on schlieren imaging with high temporal resolution to capture the fast dynamics of the expanding shock wave in a simulated Martian atmosphere.

Since reducing the atmospheric pressure to simulate the Martian environment results in a smaller relative change of the refractive index induced by the shock wave, the schlieren apparatus needs to have a much higher sensitivity than would be needed to capture the same effects under terrestrial atmospheric conditions.

As described in the previous sections, the density change of a shock wave influences the local refractive index of the atmospheric gas according to the Gladstone-Dale relation 2.3.1. The schlieren imaging technique is sensitive to changes in the refractive index and the contrast C of a schlieren image has a linear relationship with the deflection angle θ_{\perp} for small angles. The connection between the previous sections becomes very apparent from the following relation of the schlieren imaging contrast C and the density change caused by a shock wave[‡].

$$C \propto \theta_{\perp} \propto \frac{\partial n}{\partial y} \propto \frac{\partial \rho}{\partial y} \quad (2.4.1)$$

In Figure 2.12, the previously shown density distribution along the radius of a weak spherical shock wave is plotted along with its derivative. A curve similar in shape of the latter can be expected to be seen in schlieren measurements of such a weak shock wave.

[‡]As in the previous sections, effects of absorption and emission from the schlieren object are ignored.

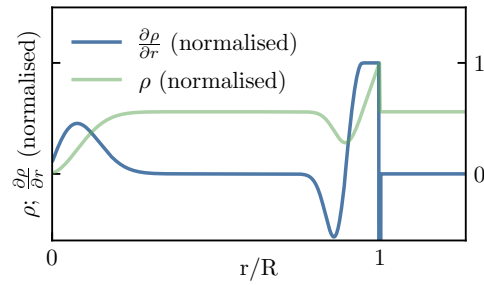


Figure 2.12.: Illustration of the density distribution ρ of a weak shock wave and its derivative $\frac{\partial\rho}{\partial r}$ as a function of the position r relative to the shock front position R . Both distributions were normalised to their respective maximum. When taking a schlieren image of such a weak shock wave, the brightness along the axis perpendicular to the knife edge changes according to the density gradient shown in blue.

3. Methodology and Setups

In the previous chapter, it was explained how an expanding laser-induced plasma results in a shock wave travelling outwards from the point of ablation on the target. This shock wave can be recorded using a microphone to gain additional insight into the interaction of the laser radiation and the material and consequently into material characteristics as described in previous works [7, 8, 19, 33, 41].

Some research on the plasma and shock wave dynamics has been conducted, visualising the laser-induced shock wave with shadowgraphing or schlieren imaging techniques [22, 57, 63]. However, most of these studies focus on terrestrial atmospheric conditions.

Since the composition and pressure of the atmosphere play a crucial role in the plasma and shock wave dynamics, this work employs several different methods to investigate the plasma expansion and shock wave dynamics in a simulated Martian atmosphere.

A recently finished setup for laser-induced plasma imaging was extended in the framework of this master thesis to allow for the acquisition of complementary schlieren and acoustic data in Martian atmospheric conditions [59]. Spectral data is also recorded with a separate setup. The experimental methods and setups will be described in detail in the following sections.

3.1. Description of the Experiments

Schlieren Imaging The main focus of this work is on a schlieren imaging system that has been designed and built to operate in low pressure environments and to achieve a high temporal resolution, allowing for the high velocity shock wave dynamics under Martian atmospheric conditions to be analysed. Refractive index variations caused by the laser-induced shock wave can be imaged with this system. The contrast in the schlieren images is achieved by using a knife edge as explained in Section 2.3 so that refractive index gradients are resolved only in the y direction. From the refractive index gradient perpendicular to the target surface, density variations in the test area can be inferred.

By adjusting the time delay between the ablating laser pulse and the schlieren measurement, a temporal sequence of successive images can be recorded that shows the expansion of the shock wave. In the following, this type of measurement will be called a time series.

When the same spot on the target is probed multiple times in a LIBS measurement, a crater develops, influencing the shock wave dynamics and the plasma emission. This change in the dynamics is studied by taking a series of images while the timing between the schlieren measurement and the laser pulse is kept constant. In the following, this type of measurement will be called a shot series.

These two types of measurements can be combined to obtain a data set revealing the change in the shock wave dynamics depending on the shot number on the same spot.

The influence of the laser energy used to ablate the material and the influence of the ambient pressure on the shock wave dynamics are also studied with this system.

3. Methodology and Setups

Plasma Imaging The plasma imaging system allows to record temporally and spatially resolved images of the plasma emission under Martian atmospheric conditions. As explained in Section 2.2, the shock wave is generated by the expanding plasma plume. At some point after plasma ignition, this shock wave decouples from the luminous plasma. By comparing the dynamics of the plasma expansion and the shock wave expansion, the time of decoupling is investigated.

Acoustic Measurements When probing the same spot on the target multiple times in a shot series, the acoustic wave generated by the ablation process changes over the course of the measurement. The decrease in its acoustic energy was shown to correlate with the hardness of the target material [7]. To investigate a possible correlation between the dynamics of the shock wave and the acoustic signal, acoustic data is acquired complementary to all schlieren measurements using a microphone.

Apart from signal changes in a shot series, the influence of the laser energy and the ambient pressure are also studied.

The system to record acoustic data was designed and built as part of this work.

Spectral Measurements While some information on the sample material can be gathered from acoustic data, most of the scientific value of a LIBS measurement comes from the spectral data, which reveals the target's composition. When performing a shot series measurement, the ablation process results in a growing crater, revealing deeper layers of the target.

In geological field measurements, this method is used to acquire depth profiles of the sample so that the potentially weathered surface composition can be distinguished from the bulk material.

When the crater grows, conditions in the plasma change through physical matrix effects, resulting in spectral changes that are not attributed to changes in the material composition. To avoid effects caused by a changing target composition, preferably homogeneous samples were chosen for this thesis. To investigate a possible correlation with the acoustic data and the shock wave dynamics, spectral data of shot series are also acquired. For this, a LIBS system with high spectral resolution is used.

Details on the experimental setups with a focus on the schlieren imaging system and the acoustic measurements will be discussed in the following sections.

First, a traditional LIBS system with high spectral resolution that was built for previous works will be discussed briefly.

A second setup separate from this LIBS system is used to acquire the schlieren and plasma images, as well as the acoustic data. The schlieren and plasma imaging system as well as the microphone all share the same laser system and atmospheric simulation chamber. These components will be discussed before a closer look on the plasma imaging system is taken. Finally, the main parts of this work will be presented in detail, starting with the schlieren imaging system. The last section of this part is dedicated to the microphone setup.

3.2. LIBS Setup with High Spectral Resolution

The LIBS system used to acquire spectral data from laser-induced plasmas achieves a very high spectral resolution over a wide range of wavelengths from ultraviolet to infrared. It uses the Echelle spectrograph *Aryelle Butterfly* by *LTB* with a gated ICCD camera *iStar* by *Andor* that allows to start the measurement shortly after plasma ignition, when the continuum emission has diminished. It can record spectra from 270 nm to 850 nm at a resolution of about 0.03 nm for the ultraviolet and about 0.09 nm for the near infrared range. The laser used to ablate the sample material is the Q-switched Nd:YAG laser *Inlite II-20* by *Continuum*. A cascade of attenuation filters allows for the nominal laser energy of 120.5 mJ to be adjusted down to 0.4 mJ. For this work, a laser energy of about (17.9 ± 0.5) mJ is used. The laser's pulse length is approximately 6 ns.

To simulate Martian atmospheric conditions, a vacuum chamber that can be filled with gas containing 95.55 vol – % CO₂, 2.70 vol – % N₂, 1.60 vol – % Ar and 0.15 vol – % O₂ is used. The plasma is ignited inside this simulation chamber. In this setup, the gas inside the chamber can be pumped out while new gas is flowing in at the same time. This allows operating at Martian atmospheric conditions without a contamination of the atmospheric gas with ablated target material.

The samples are placed on a motorised translation mount with three axes of movement, allowing for a specific spot on the sample to be targeted with the laser.

Data from this setup is recorded with the software *Sophi* by *LTB*.

This setup was built for previous studies and is the default LIBS system used in the scientific working group led by Susanne Schröder at the Deutsches Zentrum für Luft- und Raumfahrt. Further details can be found in [59] and [45].

3.3. Setup with Multiple Diagnostic Tools

The schlieren imaging system, the plasma imaging system and the microphone are part of the same setup, sharing the same laser system and atmospheric simulation chamber. Acoustic data can be collected simultaneously with either schlieren or plasma images. Schlieren and plasma images however can not be taken at the same time.

The following section will explain the components common to all diagnostic tools of this setup. Afterwards, the plasma imaging system, the schlieren system and the microphone system will be explained in greater detail.

3.3.1. Laser System and Atmospheric Simulation Chamber

The components common to all diagnostic tools of this setup are shown in Figure 3.1. A vacuum chamber allows for the simulation of a Martian atmospheric environment, in which a plasma can be ignited using the laser system.

Laser

The laser used to ignite the plasma is a Q-switched Nd:YAG laser by *Quantel Viron*. It operates at the fundamental emission wavelength $\lambda = 1064$ nm with a fixed shot frequency of 2 Hz and a pulse length of 8.1 ns.

The pulsed laser beam is focused on the target through a series of lenses. It is first collimated

3. Methodology and Setups

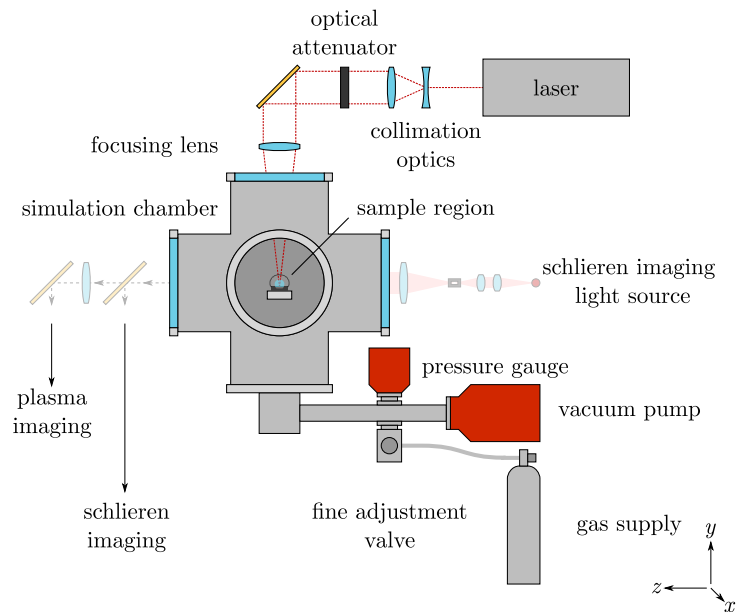


Figure 3.1.: All diagnostic tools of the setup make use of the same laser system and atmospheric simulation chamber that are shown here in a side view. The plasma is ignited inside the simulation chamber by a focused laser beam. Optical attenuators can be inserted into the optical path to adjust the energy of the laser pulse. The pressure inside the simulation chamber can be reduced using a vacuum pump. A gas supply is connected to the chamber with a fine adjustment valve. After evacuating the chamber, it can be flooded with a gas simulating the Martian atmosphere. The gas pressure is measured using a full range pressure gauge. The window on the right is used for the light source producing the background illumination in schlieren imaging measurements. The left window is used to collect light from the sample region in both plasma imaging and schlieren imaging measurements. A removable mirror allows for easy switching between the two modes. The components shown in this figure were set up by David Vogt [59].

before passing through an adjustable cascade of optical attenuation filters. These filters can be used to reduce the laser’s nominal pulse energy of about 25 mJ. For this work, most of the measurements were taken using a filter of OD = 0.1, reducing the laser pulse’s energy on the sample’s surface to about 18 mJ.

After passing the filter section, the expanded beam is redirected by a mirror to travel through a focusing lens and finally through a window into the atmospheric simulation chamber and onto the target surface.

A variable distance of the focusing lens with $f = 150$ mm from the target surface allows for the laser’s beam waist position to be adjusted. Generally, the pulsed laser beam reaches the target perpendicular to its surface. Tilting the mirror allows to target a new spot on the target in the z direction. When a new spot is targeted this way, the laser’s angle of incidence changes slightly [59].

Atmospheric Simulation Chamber

A vacuum chamber with gas inlet makes it possible to manipulate the conditions of the atmosphere in which the plasma is ignited. The gas pressure inside the chamber can be reduced to less than 50 mPa with the vacuum pumping station *Pfeiffer Vacuum HiCube 80 Eco*. To

simulate Martian atmospheric conditions, a bottle with gas containing 95.55 vol – % CO_2 , 2.70 vol – % N_2 , 1.60 vol – % Ar and 0.15 vol – % O_2 is connected to the chamber through a fine adjustment valve. By opening the valve after evacuating the chamber, the gas pressure and composition can be adjusted to match those on Mars with pressures of around $p_0 \approx 1 \text{ kPa}$. A full range pressure gauge allows for the gas pressure to be monitored.

The sample is placed on a translation mount inside the chamber so that its position can be adjusted in one axis by $\Delta x = 25 \text{ mm}$. This makes it possible to target a different spot on the sample and to take measurements on more than one sample without the need to open the simulation chamber. In combination with the laser system’s mirror, the laser spot can be moved in both x and z direction on the sample.

For optical access, the chamber has windows on two sides and on the top. The laser used for the LIBS measurements passes through the top window. One of the side windows is used for the collection of light from the sample area when taking schlieren or plasma images. This means that all images taken with either the plasma or the schlieren imaging setup view the plasma from a side perpendicular to the laser beam. The third window is placed on the opposite side facing towards the light source delivering background illumination in schlieren imaging measurements.

A door on one of the chamber’s six sides can be opened to change and position the target under investigation. Inside this door, the microphone used for the acoustic measurements is mounted with tape.

3.3.2. Plasma Imaging System

The plasma imaging system is capable of taking both spectrally and spatially resolved images of the plasma emission. The gated camera makes investigations of the plasma’s temporal evolution possible. This type of system can be used to investigate the spatial distribution of species within a plasma and can give insight into plasma dynamics and the distribution of parameters like temperature throughout the plasma.

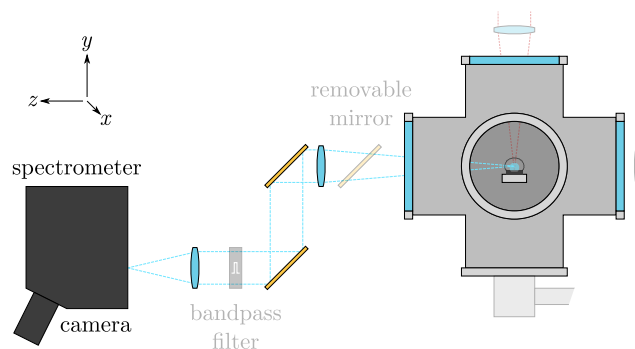


Figure 3.2.: The plasma imaging system uses a spectrometer and a gated camera to record images of the plasma emission. Depending on the spectrometer settings, the images have either spectral resolution in one axis and spatial resolution in the second axis, or both axes are spatially resolved. In the latter case, bandpass filters can be introduced to the optical path to image only certain spectral lines. Removing the first mirror behind the simulation chamber switches the setup from schlieren imaging mode to plasma imaging mode. This system was built by David Vogt [59].

3. Methodology and Setups

The plasma imaging system uses the laser and atmospheric simulation chamber that were already discussed in Section 3.3.1. By removing the mirror depicted in transparent gold in Figure 3.2, the plasma emission can enter the optical path of the plasma imaging system and plasma images can be taken. The system mainly consists of the optics for collecting the plasma emission, a spectrometer and a gated camera.

This apparatus was previously developed and built by David Vogt, details can be found in the according works [59, 62].

Spectrometer

The spectrometer used to disperse the plasma emission is a *Kymera 328i* imaging Czerny-Turner spectrometer by *Andor*. Its entrance slit width can be adjusted between 10 μm and 2500 μm . The grating and blaze angle can be chosen from a turret with three different diffraction gratings to adjust the spectrometer for the emission range under investigation. The system can be used to capture images that have both spatial and spectral resolution. In this case, one axis of the images represents a spatial axis while the other one resolves wavelength.

For the purpose of this work, the entrance slit was completely open and the spectrometer was set to the zeroth order of diffraction. This way, a two-dimensional image of the plasma can be recorded. By using an optical bandpass filter, specific emission lines of the plasma can be selected so that only a small spectral range is imaged by the camera. The data recorded for this work was acquired without such a filter, so light from the entire plasma spectrum was collected.

The spectrometer can be controlled with the software *Andor SOLIS*.

Camera

The plasma images are recorded using the ICCD camera *iStar334T* by *Andor*. Its nominal operating spectral range is between 180 nm and 850 nm with a resolution of 1024 px \times 1024 px. This camera can be gated to exposure times shorter than 2 ns, so plasma dynamics can be captured. The sensor can be cooled to -30°C to reduce noise.

All functionality can be controlled through the software *Andor SOLIS*.

3.3.3. Schlieren Imaging System

The schlieren imaging apparatus was designed specifically to capture the dynamics of the expanding shock wave resulting from laser-induced plasmas in a Martian atmosphere. Its development and construction constitute a large part of the work done for this thesis. The design follows that of a classic Toepler's lens-type schlieren system, which was discussed extensively in Section 2.3.

Figure 3.3 shows the system integrated into the previously discussed plasma imaging setup. In Figure B.1 in the appendix, photos of the system are presented. Behind the window used for light collection, a removable mirror redirects the light from the sample region into the optical path of the schlieren apparatus. If this mirror is removed, light from the sample region travels the optical path of the plasma imaging system instead.

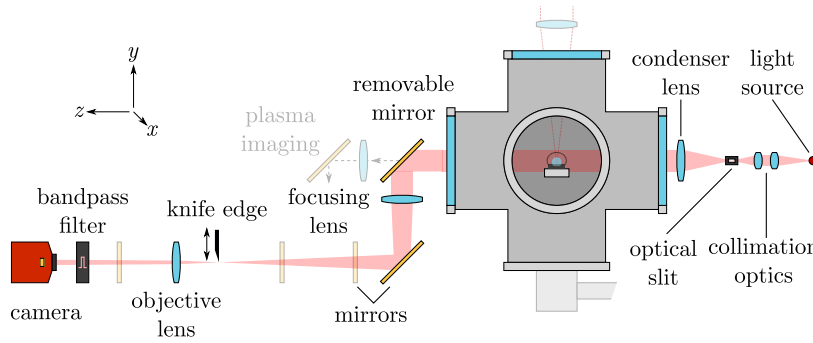


Figure 3.3.: When a plasma is ignited in the simulation chamber, a shock wave travels through the ambient gas. To take schlieren images, the shock wave is illuminated by a pulsed light source from the right. To provide a well defined light source image, the light is focused on an optical slit by a collimation system. The sample area is illuminated through an aspherical condenser lens. When the removable mirror behind the simulation chamber is inserted, light passes through the schlieren system to the camera. A series of mirrors is used to fit the system on the optical table. The knife edge can be moved on a translation stage to adjust the cutoff settings. An optical bandpass filter is mounted in front of the camera to reduce the amount of plasma emission and stray light collected by the camera.

Design Parameters

To image laser-induced shock waves in a simulated Martian atmosphere, the schlieren imaging apparatus has to be much more sensitive than if the shock wave was travelling through a terrestrial atmosphere.

As seen in Section 2.2, the relative density change across a strong shock front is constant as defined by the gas' ratio of specific heats. This density gradient results in a refractive index gradient according to the Galdstone-Dale relation 2.3.1. At lower pressures like those on Mars with $p_0 \approx 1$ kPa, the refractivity $n - 1$ also drops, leading to a smaller change in the refractive indices across the shock front, while the relative density change remains constant. According to Equation 2.3.10, the schlieren system's sensitivity can be enhanced by choosing a large focal length f_{foc} of the focusing lens, or by reducing the size of the light source. Since there needs to be enough light passing the knife edge for the recording camera to produce an image with reasonable signal to noise ratio, a high radiance light source with a small footprint is needed.

For this setup, a focal length of $f_{\text{foc}} = 750$ mm was chosen, limited by the space available on the optical table. This limitation makes a number of mirrors necessary to fold the optical path. In Figure 3.3 they are shown in gold.

To provide a light source with a well defined size for the background illumination, a $5 \mu\text{m}$ optical slit is used. It is illuminated from the back by a laser diode stack. Due to the lenses used in this setup, the height of the slit image on the knife edge is about $37.5 \mu\text{m}$.

Both the focal length f_{foc} and the slit size were chosen by considering the maximum angle of deflection θ_{\perp} for a strong spherical shock in a CO_2 atmosphere. A derivation can be found in appendix B.1. The selected optical components proved to deliver schlieren images of sufficient quality in first tests of the experimental setup.

3. Methodology and Setups

For the knife edge, a commercial razor blade by *Wilkinson* is used. It is attached to a translation stage, so the cutoff R of the setup can be adjusted to match the experimental conditions. The knife edge is mounted so that the discontinuity of the shock wave results in a brightening of the background illumination. This allows for an intuitive judgement of the data quality during measurements. A more detailed look on the influence of the cutoff on the quality of the data is given in Section 3.3.3.

Considering previous studies of shock waves and the plasma expansion, it can be concluded that a temporal resolution on the order of ~ 10 ns is needed [22, 51]. In this setup, the high temporal resolution is achieved by using a pulsed light source for the background illumination. This way, a conventional camera can be used to take the schlieren images. The actual temporal resolution achieved in this work is about $\Delta t_{\text{ls}} \approx 40$ ns as will be explained in Section 3.3.3.

Light Source

At these short illumination times, a light source with high radiance is needed. In this setup, a stack of three laser diodes *SPLDS90A 3* by *Osram* is used. According to the manufacturer, it has a short rise time of about 1 ns. The background illumination it provides for the schlieren images is at approximately half of the dynamic range of the camera so that both darkening and brightening of the schlieren image can be detected.

Since the plasma itself presents a light source, an optical bandpass is used to filter out light from the plasma emission. This of course works best when the light source's wavelength is chosen in a way that it doesn't overlap with intense emission lines from the plasma. The central wavelength of the laser diodes in this system is $\lambda = (905 \pm 10)$ nm with a full width at half maximum of $\text{FWHM}_\lambda = 7$ nm. According to the manufacturer, the size of the emitter stack is $200 \mu\text{m} \times 40 \mu\text{m}$. An optical system is used to produce a demagnified image of the light source on the $5 \mu\text{m}$ wide optical slit so that the radiance transmitted through the slit is maximised.

In accordance with the light source's wavelength, all lenses have an anti reflex coating for the near infrared and the mirrors of the schlieren system are coated in gold to minimise transmission and absorption losses.

The laser diode stack is driven by an avalanche pulse generator, the electrical circuit of which can be found in Figure B.2 in the appendix. As will be shown later, the time of illumination achieved with this pulse generator is about $\Delta t_{\text{ls}} \approx 40$ ns.

Camera

The schlieren images are recorded with the digital monochrome near infrared camera with global shutter *CS135MUN* by *ThorLabs*. All images taken for this work were recorded with a depth of 10 Bit and a resolution of $1280 \text{ px} \times 1024 \text{ px}$ with an exposure time of $\Delta t_{\text{exp}} = 10$ ms. At the relevant wavelength of 905 nm it has a quantum efficiency of about 0.22. To remove undesired light from the surroundings and the radiation from the plasma itself, a bandpass filter *FF01-900/11-25* by *Semrock* with a transmission window centred around 900 nm and a full width at half maximum of about 20 nm is mounted to the camera. Although this way the plasma's line emission is effectively suppressed, some continuum emission from the early stages of the plasma is present in images recorded shortly after plasma ignition.

An objective lens $f_{\text{obj}} = 150$ mm is used to image the schlieren object on the sensor and

maximise the illuminated area.

The software used for data acquisition is *ThorCam* by *ThorLabs*.

Trigger System

The synchronisation of the laser, the camera and the light source is achieved with the delay generator *9520 Series Pulse Generator* by *Quantum Composers*. Figure 3.4 shows the different connections and delays to achieve synchronisation. The delay generator is also used to capture schlieren images at different times after plasma ignition, allowing for time series to be recorded. This is achieved by delaying the illumination from the light source and the camera exposure by t_{delay} compared to the time of plasma ignition. Due to the relatively slow frame rate of the camera used in this setup, each frame of a time series has to be recorded from a different laser-induced plasma.

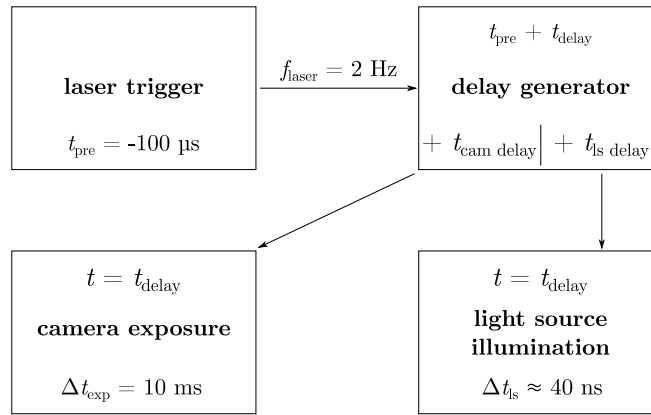


Figure 3.4.: Trigger system used to synchronise the different components. Schlieren images are recorded with the laser shot frequency of $f_{\text{laser}} = 2$ Hz. A trigger signal is sent from the laser 100 μs before the plasma ignition. A variable delay t_{delay} affecting both the camera and the light source defines the time t after plasma ignition, at which the schlieren image is taken. The constant delay times $t_{\text{cam delay}}$ and $t_{\text{ls delay}}$ for each of the channels account for the response lag of each component. The camera exposure time is set to $\Delta t_{\text{exp}} = 10$ ms and the light source's illumination time is about $\Delta t_{\text{ls}} \approx 40$ ns, defining the temporal resolution of the system.

All components follow the laser's trigger signal $t_{\text{pre}} = -100$ μs before the actual laser pulse. The laser is used with a repetition rate of $f_{\text{laser}} = 2$ Hz and the trigger pulse is sent with the same frequency to the delay generator. Both output channels for the camera and the light source now receive a variable delay t_{delay} defining the timing relative to the plasma ignition of the image taken. The channel for the camera trigger and the light source trigger are delayed by $t_{\text{cam delay}} = 97.295$ μs and $t_{\text{ls delay}} = 99.795$ μs , respectively. This accounts for the laser trigger's offset and the delay intrinsic to each component between receiving the trigger signal and starting the exposure or the light pulse. The offset timings are chosen in a way that the camera receives all of the light from the light source while not starting the

3. Methodology and Setups

exposure earlier than necessary.

The delays are chosen so that $t_{\text{delay}} = 0$ corresponds to the first plasma emission visible on the camera*.

This procedure reduces the influence of visible continuum emission from the plasma on the schlieren images. Since the start of the camera exposure is delayed in the same way the light source illumination is, the influence of the continuum emission is only significant for the first frames with $t_{\text{delay}} < 1 \mu\text{s}$.

All timings were tuned experimentally.

Characterisation

Light Source To characterise the illumination time Δt_{ls} achieved with the light source, the number of emitted photons n_{ph} was measured with a temporal resolution of 10 ns. The plasma imaging system introduced in Section 3.3.2 was used for this measurement.

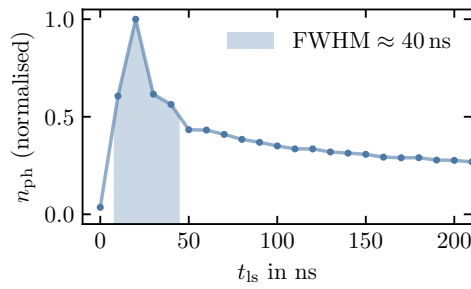


Figure 3.5.: Normalised development of the photon count n_{ph} emitted by the light source over time t_{ls} . Each data point was integrated over 10 ns. The shaded area shows the full width at half maximum of about $\text{FWHM} \approx 40 \text{ ns}$.

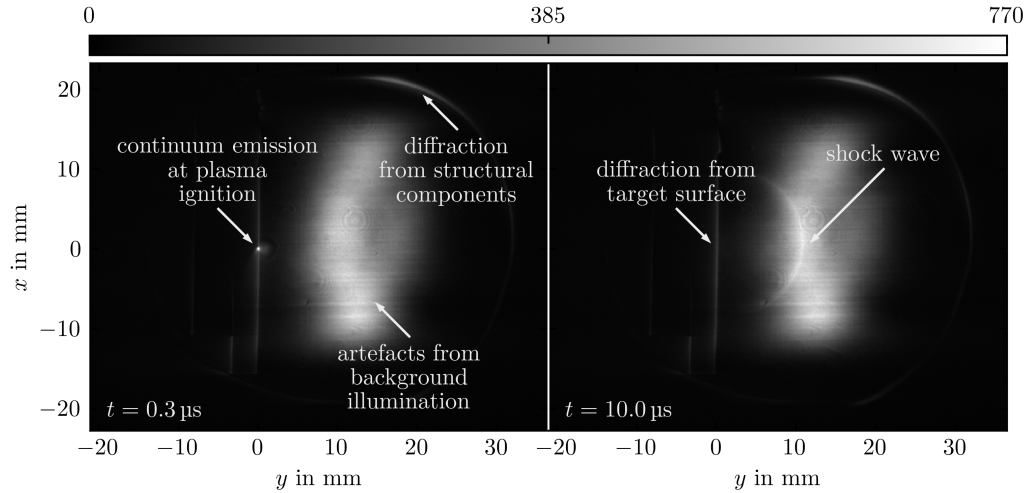
Figure 3.5 shows the evolution of the normalised photon count within a 10 ns period as a function of time t_{ls} . The illumination time can be defined as the full width at half maximum of this curve, which is $\Delta t_{\text{ls}} \approx 40 \text{ ns}$.

Schlieren Images The schlieren system described above is capable of producing schlieren images of sufficient temporal resolution and contrast for this work in the low pressure Martian atmospheric environment.

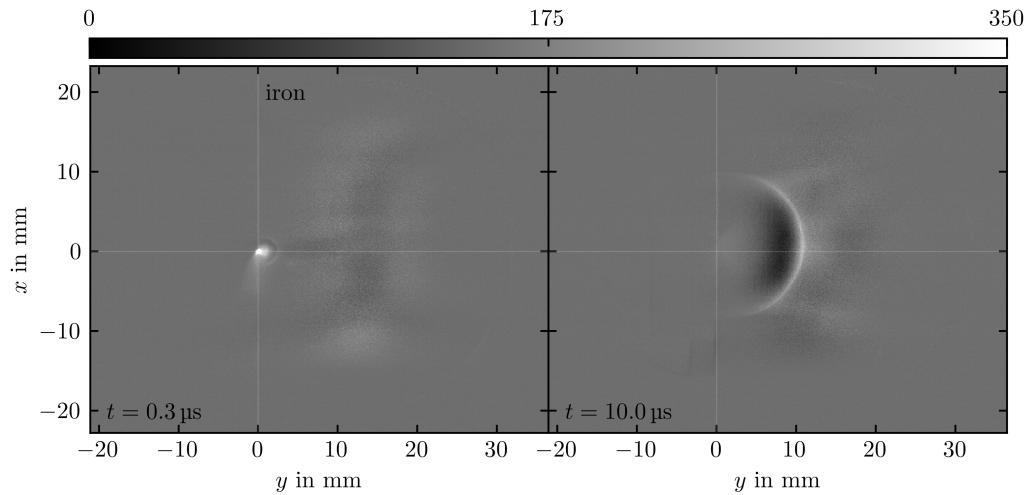
Two example pictures at different delay times are shown in Figure 3.6a. Both images were taken with an iron target at Martian atmospheric conditions with $p_0 = (1.04 \pm 0.03) \text{ kPa}$. In contrast to all other schlieren images shown in this work, no background image was subtracted so that the different optical effects relevant to this setup are clearly visible.

From these images it is obvious that the background illumination level is not constant over the entire field of view. Instead, the center of both images is much brighter than the rest. This inhomogeneous background illumination can be attributed to two effects. The first one is optical aberration from the different lenses used for this setup. A previous test system

*In practice, this was done by removing the filter so that the camera could capture more of the continuum emission's spectrum, and finding the frame of first light by scanning the delay generator with nanosecond resolution.



(a) Schlieren images before background subtraction. In the left frame taken at $t = 0.3 \mu\text{s}$, the continuum emission from the early plasma can be seen. The shock front emitted during the ablation process is clearly visible in the right image taken at $t = 10.0 \mu\text{s}$. Both images show significant artefacts from aberration and diffraction.



(b) Schlieren images after background subtraction at $t = 0.3 \mu\text{s}$ and $t = 10.0 \mu\text{s}$ after plasma ignition. The artefacts from aberration and diffraction are reduced significantly. In both images, the shock wave can be seen as bright hemispheres.

Figure 3.6.: Schlieren images from an iron target in a simulated Martian atmosphere before and after background subtraction. The grey scales represent the recorded pixel values.

was improved by incorporating an aspherical condenser lens instead of a plano-convex one. The second effect that appears to be more dominant in these images is diffraction from the knife edge. While the coherence lengths of a laser diode stack like the one used as the light source is generally much shorter than that of traditional lasers, clear diffraction patterns are still visible. This is not only true for diffraction from the knife edge, but also for diffraction from objects in the sample region and from the optical slit. In Figure 3.6a, diffraction from structural components of the setup can be seen as a bright line in the top right of both images. This particular feature is a result of diffraction from one of the optical mounts close

3. Methodology and Setups

to the sample region limiting the field of view. In the two images, diffraction from the target surface can also be seen.

In the left image, taken at $t = 0.3 \mu\text{s}$ after plasma ignition, the effects of continuum emission passing the bandpass filter can clearly be seen as a small bright spot on the target's surface. This undesired signal is gone in the image on the right taken $10 \mu\text{s}$ after plasma ignition, since the beginning of the camera exposure is delayed along with the light source illumination as described in the previous section.

Finally, the shock wave travelling outwards can clearly be seen in the right picture. While far less pronounced in the left image of Figure 3.6b, after subtraction of a background image it is also clearly visible.

After background subtraction, the undesired effects seen before are reduced significantly. The images now display the change in irradiance ΔE_e reaching the camera sensor. However, since the background illumination level is not constant over the entire image, the change in brightness does not only depend on the refractive index, but also on the relative position in the image. This does not hinder the analysis of the images for this work, as mostly positional data is used. Since the spatial extent of the refractive index gradient across the shock front is much smaller than the extent of the background illumination artefacts in the recorded images, a qualitative evaluation of the change in brightness is still possible.

It should be noted that the contrast in the images actually represents the negative change in refractive index $-\frac{\partial n}{\partial y}$ with respect to the y axis, so a brightening of the image actually represents a lessening refractive index while a dark area in the image shows an increase in refractive index. This is because the orientation of the knife edge was chosen in a way that the discontinuity of the shock wave stands out bright from the background. It should also be

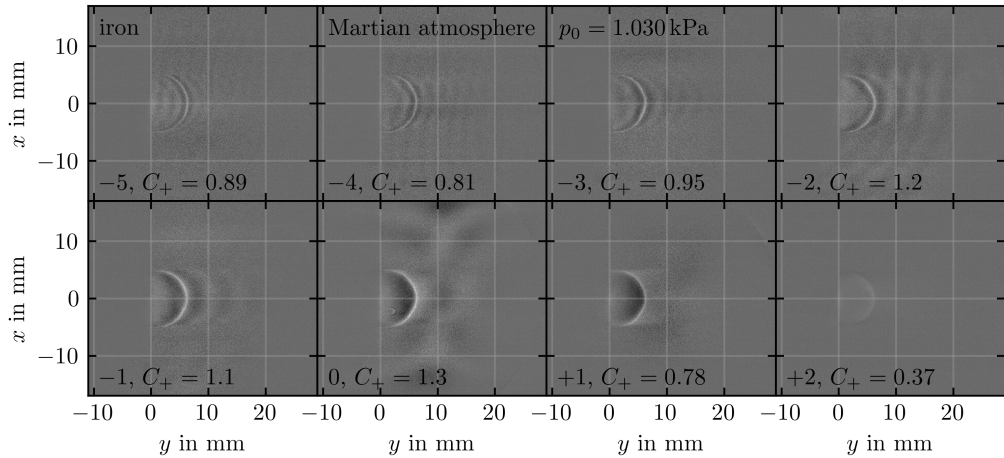


Figure 3.7.: Scan of the cutoff settings. The images were taken under Martian atmospheric conditions with an iron target. The cutoff position is noted as an integer representing a quarter turn on the fine adjustment screw in the bottom left of each frame. Position 0 was used for most of the measurements. Larger numbers represent a greater cutoff R . An offset was applied to each image so that the background illumination is the same. The ratio of change in maximum brightness and the background brightness is given as C_+ . Around the shock front, diffraction patterns can be seen as ripples in the y direction. The density of these ripples changes with the cutoff setting, suggesting they are a result of diffraction from the knife edge.

emphasised that all images show changes in refractive index exclusively in the y direction.

Cutoff Figure 3.7 shows a cutoff scan of the schlieren system’s knife edge. The position of the knife edge is noted with integers in the bottom left of each frame, representing a quarter turn of the fine adjustment screw of the knife edge’s translation mount. Position 0 represents the cutoff setting used for all measurements conducted under Martian atmospheric conditions. Negative values represent a decrease in cutoff while the cutoff is increased for positive values. In these images, the contrast C_+ after background subtraction is also noted in the corner of the respective image. It was calculated by taking the ratio of the change in maximum brightness of an image to the general background illumination level after background subtraction. From this cutoff scan it is clear that the maximum contrast is achieved for the position 0. The contrast decreases much faster with higher cutoff than it does when lowering the cutoff.

3.3.4. Acoustic Recording System

To record acoustic data that can be compared directly to previous measurements of laser-induced pressure waves conducted in [7], a microphone was integrated into the setup as part of this work. The acoustic recording system is shown in Figure 3.8. The microphone is mounted to the inside of the vacuum chamber with tape at a distance of roughly 60 mm to the target. Care was taken so that the membrane of the microphone faces directly towards the sample to reduce the influence of disturbing effects such as echoes in the recordings.

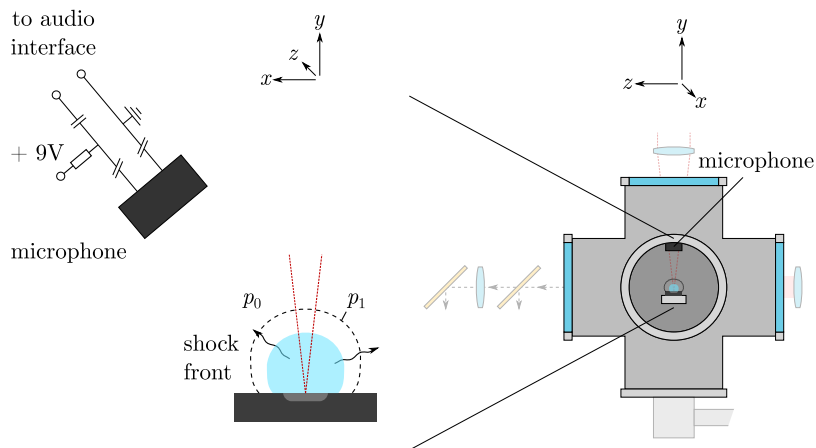


Figure 3.8.: System used to record the acoustic waves emitted from the ablation process. On the right side, an overview of the microphone mounted inside the simulation chamber is given. The left side shows a close up view of the microphone mounted above the sample. A phantom power circuit provides a voltage of 9 V to the microphone. The distance between the sample and the microphone is about 60 mm. The power supply was built with the help of Christian Seel.

3. Methodology and Setups

Microphone

The microphone used for this work is a common electret microphone from an unknown manufacturer. Since the specific wave shape is not being evaluated for this work, it is used without any calibration or characterisation. Typically, electret microphones like the one used on the Perseverance rover are able to record frequencies in the audible range from 100 Hz to 10 kHz [35].

Electret microphones need a constant power supply, so a simple phantom power circuit that is shown schematically in Figure 3.8 was built.

Audio Interface

To record the audio signal from the microphone, the commercial audio interface *UMC202HD* by *Behringer* is used. While the exact bandwidth and frequency response of this device are not characterised, it is built for music production and should therefore cover the audible range of approximately 20 Hz to 20 kHz.

The audio data is recorded with a depth of 24 Bit at a sampling rate of 192 kHz using the free software *Audacity*.

3.4. Samples

The influence of material properties on the shock wave dynamics, the acoustic signal and the plasma spectrum is investigated using a set of samples with different characteristics. The materials and their properties are listed in Table 3.1. In Figure 3.9, images of the samples are shown.

Table 3.1.: The materials and some of their properties used for this work. They were partially provided by Baptiste Chide. The Vickers hardness numbers HV from [7] were measured with the actual samples used in this work. The commonly used unit of the hardness number HV includes the standard gravity g_0 .

Material	ρ in $\frac{\text{g}}{\text{cm}^3}$	δ_{th} in nm	δ_{opt} in nm	HV in $\frac{\text{kg}}{\text{mm}^2} g_0$	References
Iron	7.87	336	21	104 ± 6	[7]
Lead	11.35	347	15	8 ± 1	[7]
Amorphous Gypsum	1.00	28	—	3.0 ± 0.5	[7]
Crystalline Gypsum	2.32	—	—	~ 60	[32, 54]
Hematite	5.15	140	7700	1370 ± 160	[7]
Magnetite	5.17	92	229	770 ± 140	[7]
Pyrite	5.03	—	—	~ 1560	[12, 32]
Talc	2.75	—	—	~ 47	[32, 54]

The lead, amorphous gypsum, hematite, magnetite and pyrite samples were obtained from Baptiste Chide, who received the natural minerals from the Collection de Minéraux at Sorbonne Université in Paris, France. The magnetite and amorphous gypsum samples were used in [7] and [8], so a direct comparison of the results is possible. The crystalline gypsum target was obtained from Dr. Klaus Vogt.

The set of samples was chosen because of their wide variety of material properties expected to be relevant for the ablation process and for their homogeneity [7]. According to Section



Figure 3.9.: The samples used in this work were chosen for their homogeneity and wide range of properties. They were partially provided by Baptiste Chide [7]. Each of the targets has a maximum diameter of roughly 3 cm.

2.1.2, volume absorption occurs only for the two metals, while the other listed parameters indicate surface absorption.

3.5. Data Processing

All the data acquired for this study was analysed and evaluated with custom scripts and programs written in Python as part of this thesis. Calculations and fits were done using standard Python packages [23, 31, 58].

Schlieren Images For all schlieren measurements, a background image without schlieren signal was acquired prior to the measurement and subtracted from the shock wave images for further analysis. The position of the shock front perpendicular to the target surface along the y axis was determined by the peak brightness of an average from 10 lines of pixels to reduce noise. This axis crosses the point of the laser-matter interaction at $x = 0$ and $y = 0$. While the shock front positions in shot series measurements were determined with a supervised algorithm, the time series measurements were evaluated manually. The combined time and shot series measurements were also evaluated manually.

Plasma Images Prior to measurements with the plasma imaging system, a background image with the same integration time was taken and subtracted from the plasma images. From this data, the plasma's leading emission edge was determined to be the position at which the signal strength is half that of the peak intensity for each frame.

Acoustic Measurements The acoustic energy of the pressure wave recorded with the microphone was evaluated by integrating over the square of the wave shape during the first

3. Methodology and Setups

compression phase.

$$\hat{E}_a = \int_{t_0}^{t_1} (\Delta p)^2 dt \propto E_a \quad (3.5.1)$$

The integration times t_0 and t_1 were determined by a 5% threshold in the pressure change compared to the signal height of the first compression phase.

Spectral Measurements For each measurement, a series of 30 spectra from 10 different positions on the sample was averaged after background subtraction. Only for the amorphous gypsum target, this had to be reduced to 10 spectra from 10 positions, since the ablation process penetrated the sample completely. The averaged spectra were calibrated with the response function of the spectrometer. To calculate the total photon count, the spectrum signal was integrated over the entire wavelength range.

4. Analysis and Results

Material properties influence the ablation process during a LIBS measurement and consequently properties in the plasma. When a series of measurements is performed on the same location on the sample, the hardness of the material was shown to bear a correlation with changes observed in the LIBS spectra collected in the shot series. This correlation was also observed in the expansion dynamics of the shock wave and in the acoustic signal emitted from the expanding plasma plume [7, 55].

In this work, multiple techniques are employed to investigate a connection between changes in the plasma's spectrum, the acoustic wave and the dynamics of the shock wave.

Throughout this chapter, all measurements were conducted on the targets that are shown in Figure 3.9 and listed in Table 3.1.

If not noted otherwise, the laser energy used for all schlieren and acoustic measurements is $E_L = (18.22 \pm 0.22)$ mJ. The pressures that are stated for each measurement are the averages of the pressure before and after taking the measurement. Changes in the pressure during a measurement are included in the indicated error. All indicated timings refer to the delay t_{delay} set with the delay generator. As described in Section 3.3.3, this delay can be assumed to be the time after plasma ignition with negligible error compared to the time scales relevant to these measurements.

4.1. Schlieren Imaging

In this section, the dynamics and the structure of laser induced shock waves will be analysed using data from the schlieren imaging apparatus. For all measurements shown here, a background image was recorded and subtracted from the shock wave image. This reduces artefacts from optical aberration and diffraction as explained in Section 3.3.3.

All images were taken using the same exposure time and duration of the light source illumination. If not noted otherwise, the cutoff used for every measurement was close to position 0 as described in Section 3.3.3.

Each image was processed to achieve a good visual contrast of the shock wave structure. The changes in brightness within the same figure are always comparable, as the same data processing was applied. However, small changes in the cutoff setting due to external factors between measurements can lead to small contrast differences. Different figures may be processed with different offsets and scaling.

The position of the shock wave is always assumed to be at the peak brightness of the shock front perpendicular to the target surface at $x = 0$. Errors indicated in the figures are estimated directly from the images and take the width of the brightness peak into account.

All schlieren images were adjusted in a way that the origin of each picture coincides with the center of the explosion. This position was inferred from the brightest pixel of a schlieren image just after plasma ignition at $0.3 \mu\text{s}$, which coincides well with the position of the target surface.

4.1.1. Shock Wave Structure

Terrestrial Atmosphere The evolution of the general structure of a laser induced shock wave from an iron target can be seen in Figure 4.1. These images were recorded under terrestrial atmospheric conditions, where the refractive index variations are larger, leading to improved contrast of faint structures. This makes a more detailed analysis of the shock wave structure possible when compared to data taken in a simulated Martian atmosphere. The cutoff used for these measurements is much lower than the one used for data taken under Martian atmospheric conditions.

In the first frame shown at $0.4 \mu\text{s}$, a structure consisting of one spherical and one hemispherical shock wave can be seen. Each sphere contains a bright spot in its center that can be attributed to continuum radiation from the early plasma emission. Data from [22] suggests that the shock wave has already decoupled from the plasma core at this stage. A ripple pattern going off to the positive y direction can be attributed to diffraction of the background illumination from the shock front. Similar patterns can also be seen in the following images. At $0.6 \mu\text{s}$, the signal from the plasma's continuum radiation is reduced while the spherical shocks are expanding. The continuum emission continues to fade in the next frame, while the shock waves travel outwards.

At $3.0 \mu\text{s}$, the two distinct spherical waves are merging. The shocked layer between the two shock waves is visibly distorted. On the top and bottom borders of this merging layer, starting points of shock waves that are reflected on both sides of the merging layer begin to be visible. Both structures now contain a dark region in their center. This could be due to a high density region forming in the plasma, however effects of absorption of the light source radiation within the plasma could also play a role. In fact, numerical simulations of laser induced plasmas show low density regions in the center with an increased temperature in the core [51]. Plasma shielding is a well known effect for the laser initiating the plasma. Since the frequency of the Nd:YAG laser with a wavelength of 1064 nm and the light source used for the schlieren images with a wavelength of 905 nm are relatively close together, absorption effects are likely to be important in the darkening of the center region as suggested by Equation 2.1.4.

The spherical shock waves continue to merge and expand at $5.0 \mu\text{s}$ while another reflection from the target surface appears. In the following frame at $10.0 \mu\text{s}$, the two separate spherical shock waves have merged to an extent where they share a common hemispherical leading shock layer. The schlieren contrast of this leading shock wave is much lower when compared to the earlier pictures. This shows a decreasing density and pressure change over the shock front as suggested by Equation 2.2.8.

In the last two frames at $15.0 \mu\text{s}$ and $20.0 \mu\text{s}$ after plasma ignition, the outer shock wave continues to expand while the inner reflections continue to travel through the shocked region. The dark region in the center assumes a roughly triangular shape with a complex pattern on the side facing the target surface. A similar behaviour was previously seen in plasma emission images in [22], where it was attributed to adiabatic compression of the plasma by reflected shock waves. This suggests that the dark region in the center is indeed a result of absorption of the background illumination in the plasma and similar mechanisms lead to the triangular shape of the plasma.

As mentioned earlier, each frame of this time series was recorded from a different laser shot. Observations in multiple measurements showed that the presented schlieren images

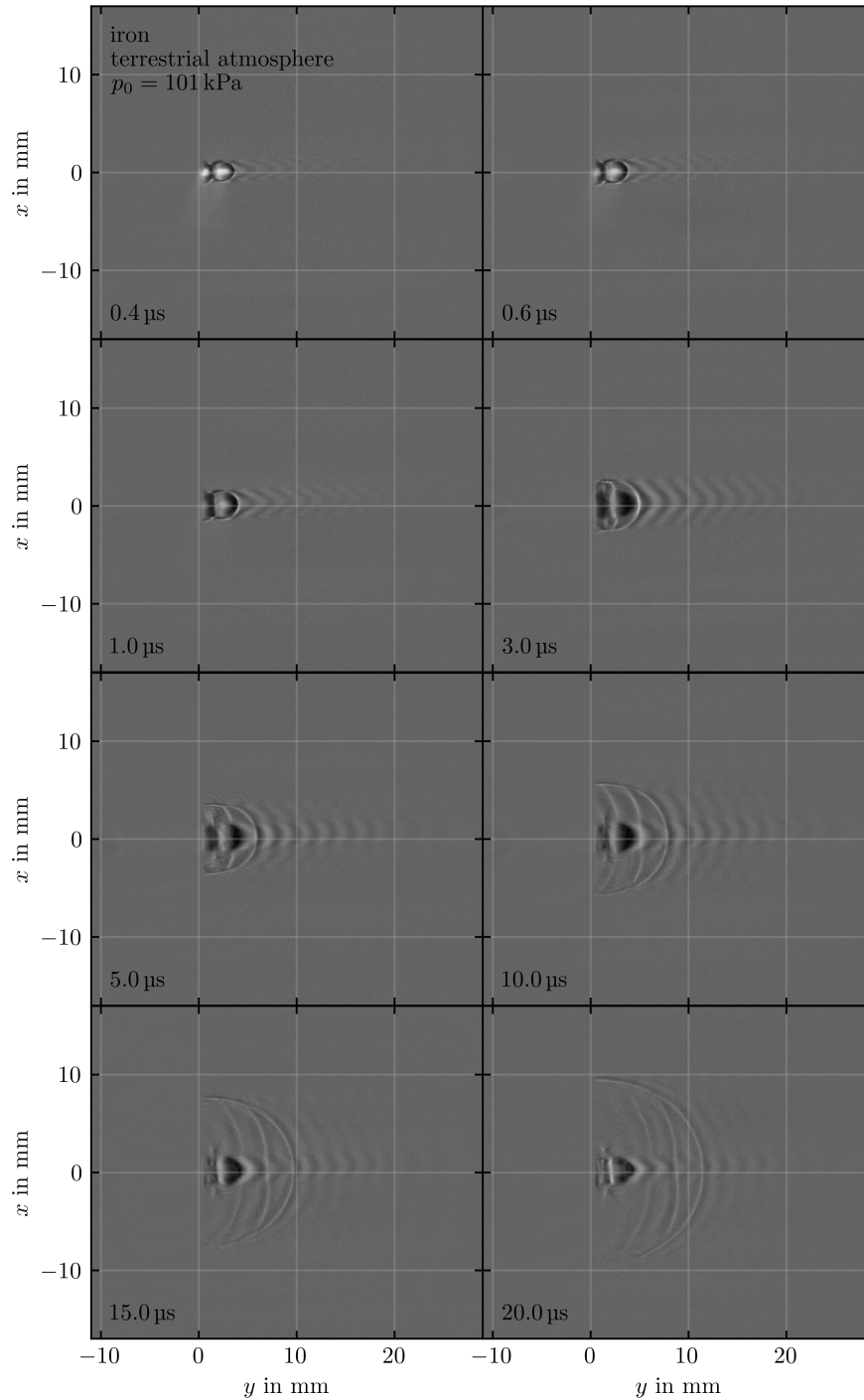


Figure 4.1.: Schlieren images of the laser induced shock wave from an iron target under terrestrial atmospheric conditions. The time after plasma ignition is noted in the bottom left corner of each frame. Two spherical shock waves are visible in the early moments of the shock wave expansion. Afterwards, they merge until only one hemispherical shock front is visible at later times. The structure of two spherical shock waves becomes less pronounced for lower pressures. Under terrestrial atmospheric conditions, the schlieren images show reflections of shock waves from the sample surface within the expanding shock front. The bright areas in the early moments are continuum emission from the plasma. The dark areas at later times are attributed to absorption of the background illumination within the plasma.

4. Analysis and Results

are highly reproducible.

The shock wave structure consisting of two spherical waves seen in Figure 4.1 at early times was also observed at reduced pressures for a terrestrial atmospheric composition. At lower pressures, the hemisphere at the target surface is larger than the spherical wave further from the target. This is a trend that continues through all investigated atmospheric pressures and suggests that while at high pressures both plasma cores are ignited in close succession, at lower pressures the plasma close to the sample is ignited earlier.

The existence of two ignition centres could be explained by the laser supported detonation wave mechanism. If the laser absorption in the shock front is sufficient, a second plasma and shock wave can be induced [56].

Another possible mechanism leading to the ignition of a second plasma could be the absorption of laser energy by particles ejected during the ablation process. The ejection of molten material droplets during laser ablation processes is a known phenomenon resulting from explosive boiling of the sample material [38, 52].

Under Martian atmospheric conditions, this double structure was only observed for some measurements on lead that will be discussed later.

While some literature on laser induced shock waves at atmospheric pressures is available, most of them focus on longer timescales or on breakdown in gasses. However, the data presented here is in general agreement with those studies [4, 22, 24, 44, 56].

Martian Atmosphere When taking schlieren images at Martian atmospheric conditions, the lower density of the ambient gas results in smaller changes of the refractive index. This leads to images with lower contrast when compared to schlieren images of shock waves in a terrestrial atmosphere. All measurements presented in the following were conducted under Martian atmospheric conditions.

Figure 4.2 shows the shock waves emitted from laser ablation processes for different target materials. All images were taken at the same time $t = 10.0 \mu\text{s}$ after plasma ignition at reduced pressures of around $p_0 \approx 1 \text{ kPa}$.

The most notable difference in the images of the different targets is a change in contrast. For iron and lead, the shock front is visible as a significantly brighter region when compared to the geological gypsum, hematite, magnetite, pyrite and talc samples, showing a stronger shock wave. The leading part of the shock wave from iron and lead is followed by a pronounced darkened region, indicating a low density area. For the other targets, this darkened region is less prominent, for magnetite it is barely visible. This distribution of bright and dark regions will be discussed in greater detail in the next paragraph, where the density distribution over the shock front will be analysed.

When comparing the data from Martian atmospheric conditions with schlieren images taken under terrestrial conditions, the position of the shock front at $10.0 \mu\text{s}$ is significantly different. The wave has expanded much further under the lower pressure Martian conditions. This effect will be discussed in detail in Section 4.5.3. The position of the shock front is slightly different for the various samples, showing a difference in the expansion velocity of the shock wave between the samples.

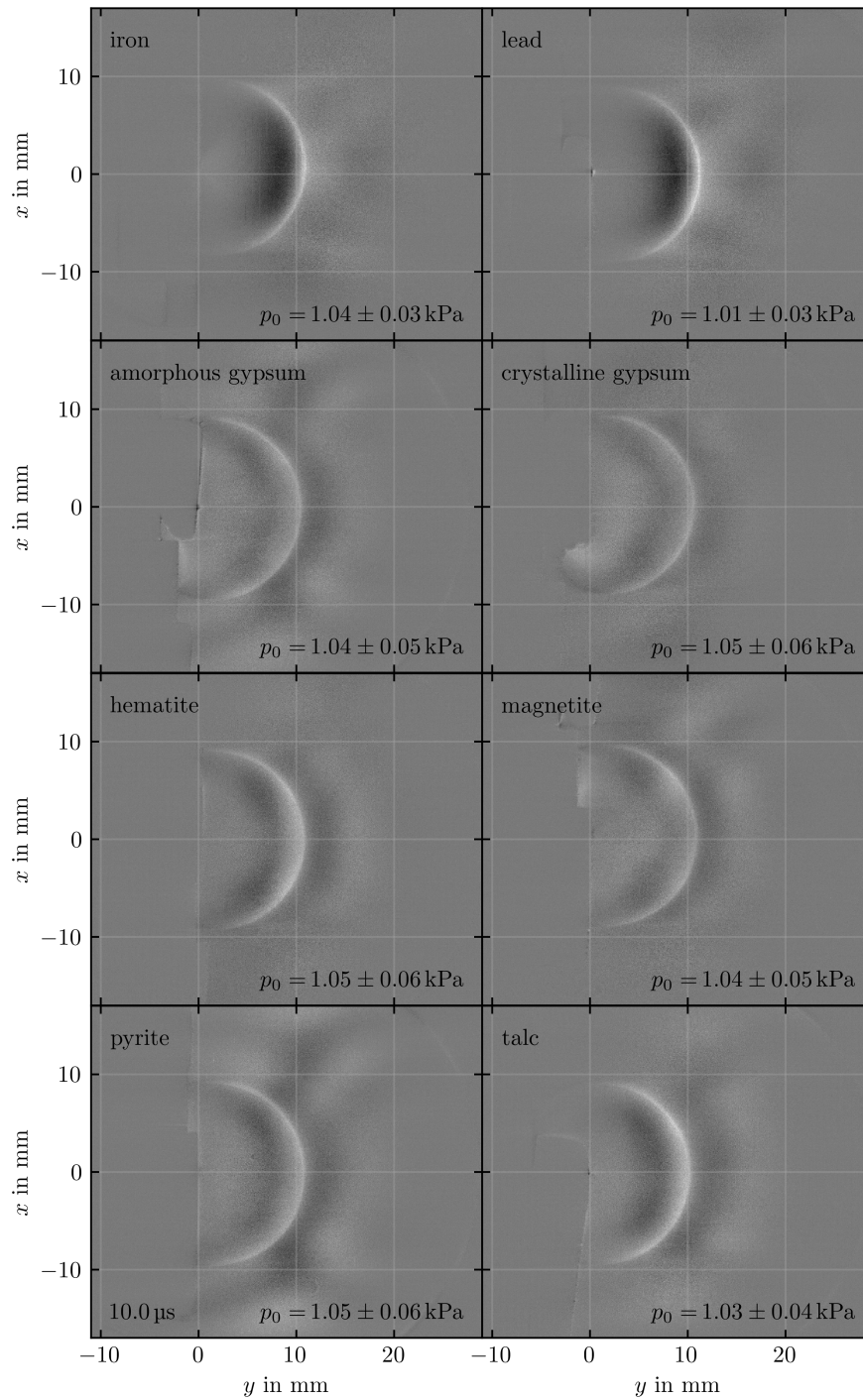


Figure 4.2.: Schlieren images of hemispherical shock waves from all investigated samples in a simulated Martian atmosphere. The higher contrast for iron and lead shows stronger shock waves when compared to the geological targets. Small differences in the position of the shock front show that the expansion velocity varies with the sample.

4. Analysis and Results

Density Distribution As explained in Section 2.4, the density distribution of the gas can be inferred from the schlieren images. Since the data taken with this schlieren imaging system is influenced significantly by optical aberration and diffraction, caution has to be exercised when evaluating the contrast in the schlieren images from this work. The relatively strong signal from the iron target is suitable for an exemplary discussion.

The brightness distribution along the y axis for $x = 0$ after background subtraction is shown in Figure 4.3, along with the corresponding original schlieren image for three different time steps. The blue curves on the right side represent the center line signal normalised to the maximum brightness. To reduce the noise of the center line signal, an average of 10 px lines around the $x = 0$ axis was taken. As mentioned earlier, the schlieren image actually shows the negative gradient of the refractive index $-\frac{\partial n}{\partial y}$ with respect to the y axis due to the orientation of the knife edge. To plot the actual gradient $\frac{\partial n}{\partial y}$ of the center line, the raw image signal was inverted.

Integrating the center line curve results in the green graph, showing the refractive index plus some integration constant $n + C$ normalised to the maximum of the distribution. To reduce the influence of noise and optical artefacts from the regions in front and behind the shocked gas and also the influence of continuum emission from or absorption in the plasma, the left integration limit is set to 3 mm and the right integration limit is chosen to be a short distance in front of the shock layer as indicated by the white and blue vertical lines.

As will become clear in the next section where the plasma expansion is investigated, the influence of the plasma can be assumed to negligible for $y \gtrsim 3$ mm. In the schlieren images of Figure 4.3, a slightly brighter region attributed to plasma emission can be seen close to the target surface. The same effect is visible in the blue curves, where the signal close to the sample is initially smaller than zero, indicating a bright region in the schlieren images. This effect grows weaker with time, which can be explained by reduced continuum emission in the later stages of the plasma lifetime.

The green curve is proportional to the refractive index plus some integration constant $n + C$ within the limits imposed by optical artefacts. According to the Gladstone-Dale relation 2.3.1, the signal is also proportional to the density.

The density distribution of a shock wave is clearly visible in the green curves at all three times with a pronounced peak at the discontinuity. Beginning at $y = 3$ mm, the refractive index and consequently the density first increases. From the strong point explosion model as well as numerical thermodynamic simulations of laser induced plasmas, a low density region in the center of the plasma is expected [51, 69]. In the presented data, the refractive index and density close to the left integration limit are smaller than in the undisturbed gas, which is in agreement with those studies. However, it is not clear if this observation actually results from the low density region in the core. Since the contrast resulting from refractive index changes is highest in the center regions of the schlieren images due to the inhomogeneous background illumination as explained in Section 2.4, the shape of the curve is somewhat distorted with changes in the center region being amplified compared to the outer regions. The refractive index rises to its maximum and declines steeply afterwards. The steepness on both sides of the peak is different for the three times shown here and the width of the peak increases at later times. As the shock wave travels outwards and weakens, the thickness of the shock front increases as can readily be seen from Equation 2.2.5. The widening peak could be explained by a thickening shock front. However, since the shock wave is moving

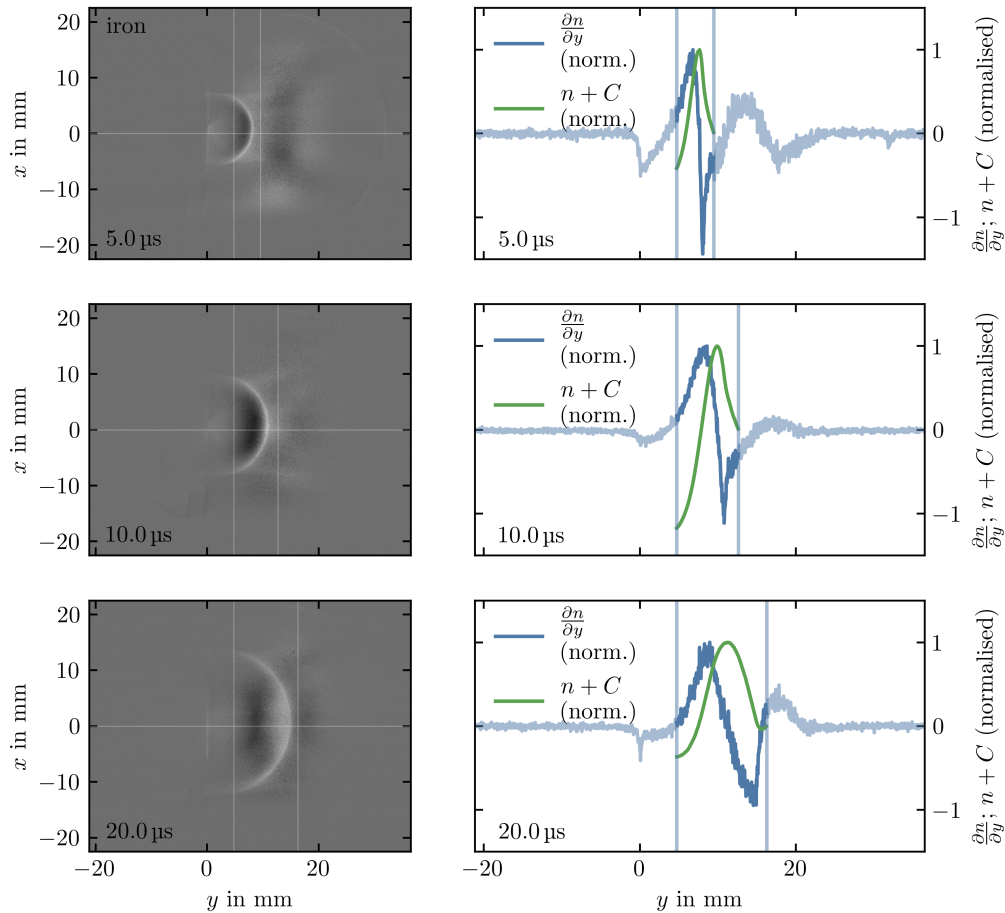


Figure 4.3.: Distribution of the refractive index n over the shock front as inferred from schlieren images at three different times denoted on the bottom left of each frame. On the left side, the original schlieren images are shown. Due to the orientation of the knife edge, the contrast actually shows the negative gradient of the refractive index $-\frac{\partial n}{\partial y}$ with respect to the y axis. The uneven background illumination leads to a higher contrast in the central regions of the schlieren images. The plots on the right side show the inverted brightness distribution along the $x = 0$ axis in blue and the integral of this distribution in green. All curves were normalised to their maximum. The blue curve is proportional to changes in the refractive index and density $\propto \frac{\partial n}{\partial y} \propto \frac{\partial \rho}{\partial y}$, so the maxima in the schlieren images coincide with the minima in the blue curves. The green curve is the integral of the refractive index gradient and thus proportional to the refractive index $\propto n + C$ and the density $\propto \rho + \hat{C}$ plus some integration constant. The integration limits are marked with vertical lines. The discontinuity is visible as a dip in all blue curves.

towards the center of the field of view, this could again be an effect arising from the spatially varying contrast of the schlieren imaging system.

While the exact shape of the refractive index and its gradient should be regarded with caution, the trends are matching results from simulations shown in [51] with a low density region in the center and a pronounced density peak at the shock front. In contrast to the weak shock wave shown in Figure 2.12, no distinct rarefaction wave is visible. This is typical for a strong shock where most of the initial mass moved by the detonation is contained within

4. Analysis and Results

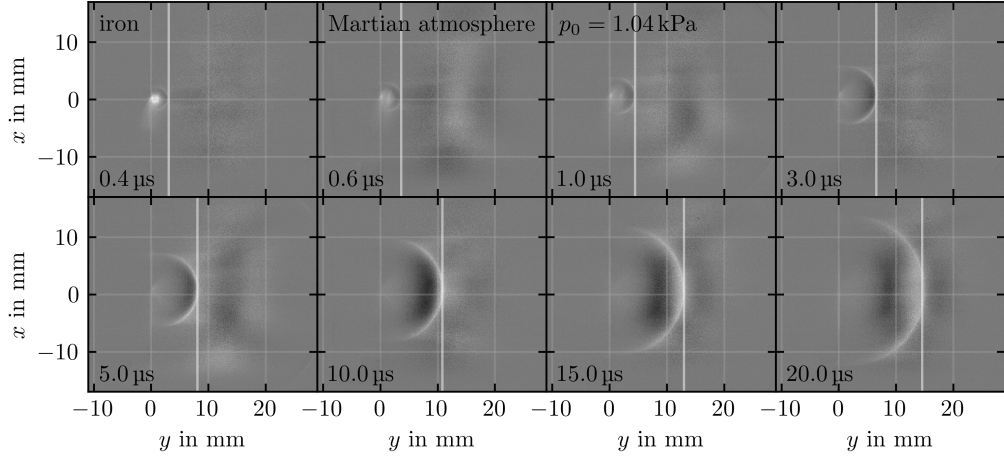


Figure 4.4.: Schlieren images of a time series measurement on iron under Martian atmospheric conditions. The position of the expanding shock front as determined for further analysis is marked with white vertical lines. The times after plasma ignition t are denoted on the bottom left of each frame.

a thin layer near the shock front [69].

From these considerations it can be concluded that taking the peak brightness is a good estimation for the position of the discontinuity and thus for the shock front.

4.1.2. Time Series

Increasing the timing delay t_{delay} between the laser and the imaging system allows for a temporal sequence of consecutive images to be recorded. Time series measurements for different target materials were recorded to compare the positional data of the shock with the temporal evolution predicted by Equation 2.2.7.

Selected images of such a time series from an iron target in a Martian atmosphere are shown in Figure 4.4 with their respective times after plasma ignition t . The positions of the shock front were evaluated manually as described in Section 4.1. To reduce noise when determining the position, 10 lines of pixels around the center $x = 0$ were averaged. White vertical lines mark the positions that are used for the evaluation of the time series.

In these images, a slight upward motion of the center of plasma ignition can be observed. This can be attributed to imperfections in the movement of the mirror used to target new spots on the sample. Changing the spot position in the z axis also leads to a small movement in the x direction.

Shock Wave Expansion The positional data y from this time series is shown in Figure 4.5 as a function of the time t after plasma ignition.

To compare the data with the temporal evolution of a strong point explosion as described by Equation 2.2.7, a function defined as

$$R(t) = \begin{cases} \zeta t^{\frac{2}{5}} & t \leq t_c \\ c(t - t_c) + R(t = t_c) & t > t_c \end{cases} \quad (4.1.1)$$

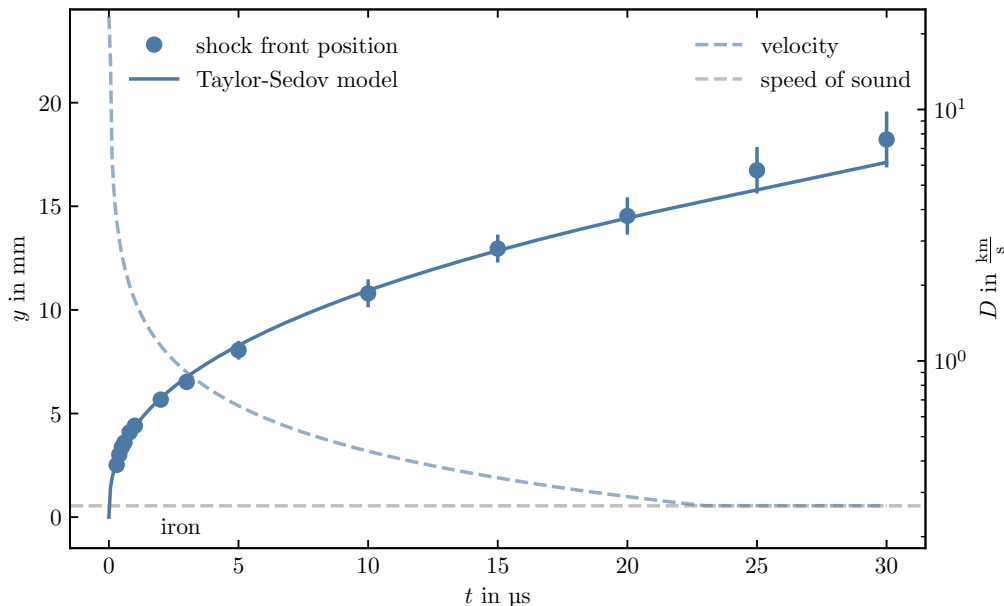


Figure 4.5.: Shock front position y as a function of time t from a schlieren measurement of an iron target under Martian atmospheric conditions. The Taylor-Sedov model from Equation 4.1.1 was fitted to the data with $\zeta = (4.35 \pm 0.04) \text{ mm } \mu\text{s}^{-\frac{2}{5}}$, showing good agreement. The derivative of the fit function gives the expansion velocity D of the shock wave and is shown as a dashed blue line. The dashed grey line marks the speed of sound.

is fitted to the data. The y position of the shock wave is described by R , t_c is the time when the shock wave reaches the speed of sound $\frac{\partial R}{\partial t} = c$. Only ζ is a fit parameter. According to Equation 2.2.7, this parameter depends on the explosion energy E , the density ρ_0 of the surrounding gas and on the heat capacity ratio contained in ξ_0 . As soon as the shock wave decouples from the plasma and starts travelling through the ambient atmosphere, the heat capacity ratio stays approximately constant. In the next paragraph on the plasma expansion, it will be shown that the decoupling of the shock wave from the luminous plasma happens early in the timescales considered for this work at approximately 500 ns for iron. For this reason, the heat capacity ratio will be assumed to stay constant for all materials in the further analysis. Since the density of the atmosphere also remains approximately constant, changes in the fit parameter ζ can be attributed to changes in the explosion energy with $\zeta^5 \propto E$. This relation will be of importance in the following sections, where changes of the explosion energy will be discussed.

For $t \leq t_c$, function 4.1.1 follows the Taylor-Sedov model under the strong shock approximation. At the latest when the speed of sound is reached at $t = t_c$, this approximation no longer holds and the expansion should be described by a sound wave with constant velocity. For the purpose of this work, the fitted function 4.1.1 shall be called the Taylor-Sedov model. The speed of sound is calculated for a perfect CO_2 atmosphere at 290 K. For the following analysis of the shock wave expansion, the speed of sound is assumed to be approximately $c \approx 265 \frac{\text{m}}{\text{s}}$.

Along with the fitted data as a solid line, the derivative of the fitted function is shown as a

4. Analysis and Results

dashed line of the same colour in Figure 4.5, describing the velocity D of the shock wave. A grey dashed line marks the speed of sound when the linear part of the fit function is applied. This scheme can be found throughout the following analysis, though it will not be explicitly marked in the legends.

The positional data of the shock front from an iron target as inferred from the schlieren images taken in Martian atmospheric conditions shows good agreement with the fitted Taylor-Sedov model. Similar results have been obtained previously under terrestrial atmospheric conditions [22, 26, 38, 52].

The dashed line shows hypersonic velocities in the beginning of the expansion exceeding $1 \frac{\text{km}}{\text{s}}$ in the first $2 \mu\text{s}$. The expansion slows down until the speed of sound is reached at about $23 \mu\text{s}$, which corresponds to a distance of about 15 mm. All other target materials were analysed in the same way and show a very similar behaviour. The according data is presented in the appendix in Figure C.1. The pressure p_1 behind the shock front as calculated from Equation 2.2.8 is shown in the appendix in Figure C.2 for the iron target.

Equation 2.2.9 gives an estimation of the length scale at which point the strong shock approximation no longer holds. Assuming that all of the laser pulse energy of about 18 mJ contributes to the shock wave expansion, this estimation gives a characteristic length of about 26 mm for a background pressure of $p_0 = 1 \text{ kPa}$. If only 10% of the energy contribute to the explosion, Equation 2.2.9 yields a characteristic length of 12 mm. The measured distance of about 15 mm is within this range and corresponds to about 20 % of the energy being expended on the explosion. In [44], a conversion efficiency of 20 % was reported for laser induced breakdown in air, while in [4] efficiencies between 50 % and 65 % were reported.

Plasma Expansion The decoupling of the shock wave from the emitting plasma core can be investigated by comparing the position of the shock wave with the leading edge of the plasma emission, which can be recorded with the plasma imaging system. No bandpass filter was used for this so that most of the plasma emission was captured. For these images, an exposure time of 10 ns was used. The leading edge of the plasma emission was determined by the position where the recorded signal had dropped to half of the maximum value. To reduce noise, the average of 10 px around the $x = 0$ axis was taken.

This measurement on iron in a simulated Martian atmosphere is shown green in Figure 4.6 together with a section of the shock front position data presented in the previous paragraph. Since the influence of the plasma's continuum emission on the schlieren images is significant at early times, images taken earlier than 300 ns can not be evaluated. The curve obtained from the emission data is initially very similar to the development of the shock front, however it quickly levels off and remains approximately constant starting at about 600 ns. Between 400 ns and 500 ns at about 3 mm from the sample surface, the shock front position gets ahead of the plasma and detaches. In previous studies under terrestrial atmospheric conditions, it was found that the decoupling happens earlier at around 150 ns after plasma ignition [22]. Prior to the decoupling, the curve obtained from the emission data is ahead of the shock front position. In [22], this behaviour was explained by high energy radiation emitted from the hot plasma that excites the ambient medium and leads to emission from a region outside of the original plasma plume. In this thesis, very little data is available to compare the expansion prior to decoupling and the difference in the positions obtained from the plasma and schlieren images might be an effect arising from instrumentation errors.

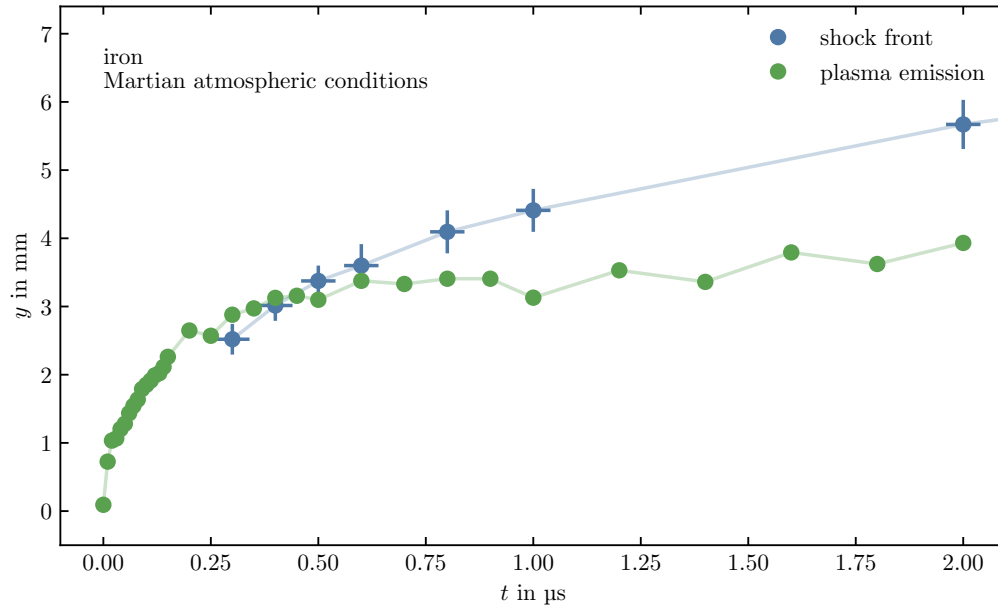


Figure 4.6.: Comparison of the positions y of the shock front and the luminous plasma front from an iron target in a simulated Martian atmosphere over time t . The leading edge of the plasma was determined as the position of half maximum along the $x = 0$ axis. The decoupling of the shock wave can be seen between 400 ns and 500 ns. Prior to that, the plasma emission is slightly ahead of the shock wave. Since only one measurement with the plasma imaging system was performed, no statistical error are indicated.

4.1.3. Shot Series

To investigate the influence of material properties on the shock wave expansion with the schlieren imaging system, a series of 300 laser shots was fired on the same spot. For the amorphous gypsum target, the number of shots had to be reduced from 300 to 50, because the deepening crater from the ablation process reached the backside of the target shortly after the 50th shot.

This procedure is similar to the acoustic measurements from the SuperCam team conducted in [7] and [8]. Schlieren images were taken at a constant delay in a Martian analogue atmosphere. In this section, data from $t_{\text{delay}} = 15 \mu\text{s}$ is evaluated exemplary. At this time, small differences in the expansion velocities lead to changes in the shock wave position that can clearly be seen in the recorded schlieren images. Further delay times will be analysed in the next section to complete the picture of the shock wave expansion dynamics.

The positional data was extracted using an algorithm looking for a local maximum around a manually defined position. A manual review of some data points was performed to confirm the accuracy of the results.

In Figure 4.7, the original schlieren images from the talc sample are shown together with the extracted shock front positions marked as white vertical lines. The shots are numbered with the first shot being $m = 0$ and the last shot $m = 299$.

For the relatively soft talc target, the shock wave position initially moves away from the sample surface over the first two frames shown in Figure 4.7. Subsequently, the shock wave

4. Analysis and Results

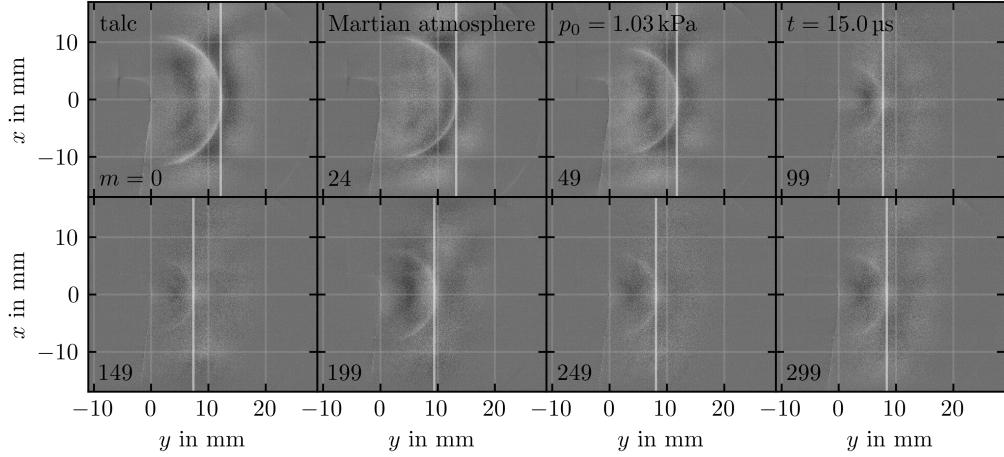


Figure 4.7.: Schlieren images of a shot series measurement on talc under Martian atmospheric conditions. All images were recorded at $t = 15 \mu\text{s}$ after plasma ignition, the shot number m is denoted on the bottom left of each frame. The position of the shock front as determined for further analysis is marked with a white vertical line. Initially, the shock front moves away from the sample surface. In the third frame it starts moving back again. After the fourth frame the position remains relatively constant. Over the first four frames of the shot series the contrast gets lower, showing a weakening shock wave.

moves closer to the target before staying in a relatively constant position starting from the 100th shot in the fourth frame.

The contrast of the shock wave decreases over the first four frames, after which it stays relatively constant on a low level. Again, it should be mentioned that the contrast of the schlieren imaging system is not constant over the entire image, so a change in contrast needs to be considered with caution. However, comparing these images to the time series in Figure 4.4, the lower contrast indeed seems to be a result of a smaller density gradient over the shock front.

After a LIBS measurement, a small crater is formed as discussed in Section 2.1. Probing the same spot on the target multiple times increases the volume of this crater depending on the material's properties. For softer targets, the crater grows faster when compared to harder target materials [8]. Changes in both the position and the schlieren contrast can be attributed to changes in the crater morphology and its effect on the plasma over each consecutive laser shot.

The shock front position as a function of the shot number m is shown in Figure 4.8 exemplary for iron, lead and talc. All positions were extracted from schlieren images taken at $t = 15 \mu\text{s}$ after plasma ignition.

During the first $m \lesssim 30$ shots, the shock front from the talc measurement moves away from the target surface as already seen in the images in Figure 4.7 from a starting position around 12.1 mm to a maximum distance of about 13.3 mm. Between the shots $31 \lesssim m \lesssim 90$, the shock front moves towards the target surface. For shots $m \gtrsim 91$, the shock front position remains relatively constant around 8 mm. During this last phase however, the spread of the data points around this constant value is much bigger than for all previous shots.

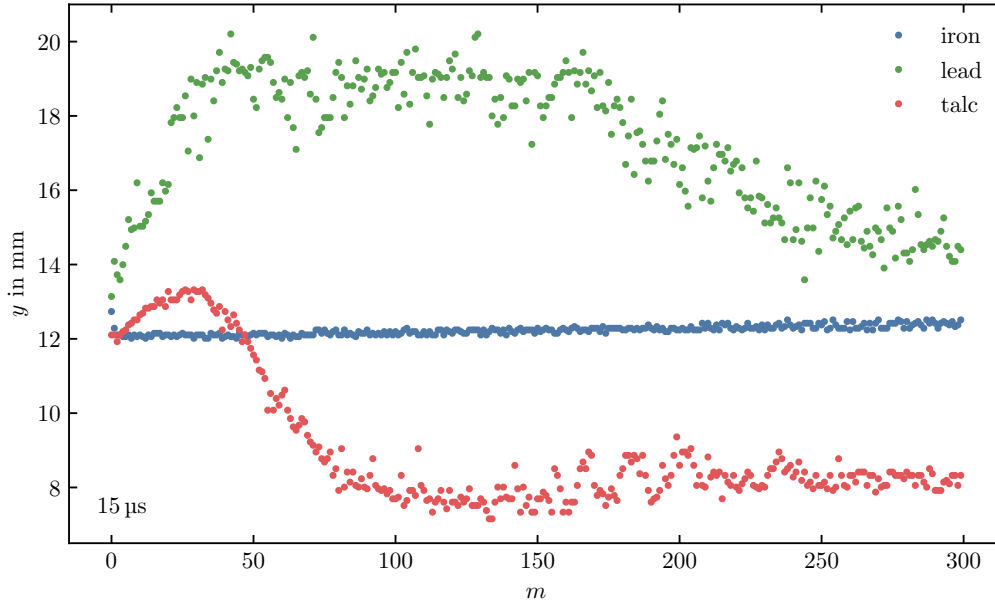


Figure 4.8.: Shock front position y as a function of the shot number m in a shot series for iron, lead and talc. All positions were extracted from schlieren images taken at $t = 15 \mu\text{s}$ after plasma ignition at Martian atmospheric conditions. The three examples show significantly different behaviours in the development of the shock front position.

Lead is showing similar but more expansive trends, with the shock front position moving away from 13.0 mm to around 19 mm over the first $m \lesssim 40$ shots. Between $41 \lesssim m \lesssim 170$, the curve is plateauing around 19 mm with significant spread of the data that can be seen throughout the rest of the curve. Afterwards at $m \gtrsim 171$, the shock front moves back towards the target surface with the last few data points at positions of around 15 mm.

Most schlieren images for lead show a highly irregular shock front at early and intermediate times $t \lesssim 10.0 \mu\text{s}$. Starting at $m \gtrsim 11$, a double structure similar to that observed for iron under terrestrial atmospheric conditions shown in Figure 4.1 can be seen in many but not all images. For later delay times $t \gtrsim 15 \mu\text{s}$, the shock front assumes a roughly elliptical shape. Two exemplary images illustrating this observation are presented in the appendix in Figure C.3. As for the iron sample under terrestrial atmospheric conditions, this double shock wave structure may be explained by strong absorption in the shock front as described by the laser supported detonation wave mechanism, or by ejected molten material droplets that absorb some of the laser radiation and undergo breakdown [38, 52, 56]. Furthermore, residual particles from previous ablation processes in a shot series can remain above the sample surface and lead to the ignition of a second plasma. The observation of irregular shock front geometries that change significantly over the course of the shot series can explain the large spread of the positional data for lead.

For iron, the shock front position initially decreases from about 12.7 mm to 12.1 mm over the first 3 shots. Afterwards, it rises linearly to about 12.4 mm for the last shot. The spread of the iron data is significantly smaller than that for talc and lead.

While the shock wave remains hemispherical throughout the entire shot series for iron, the

4. Analysis and Results

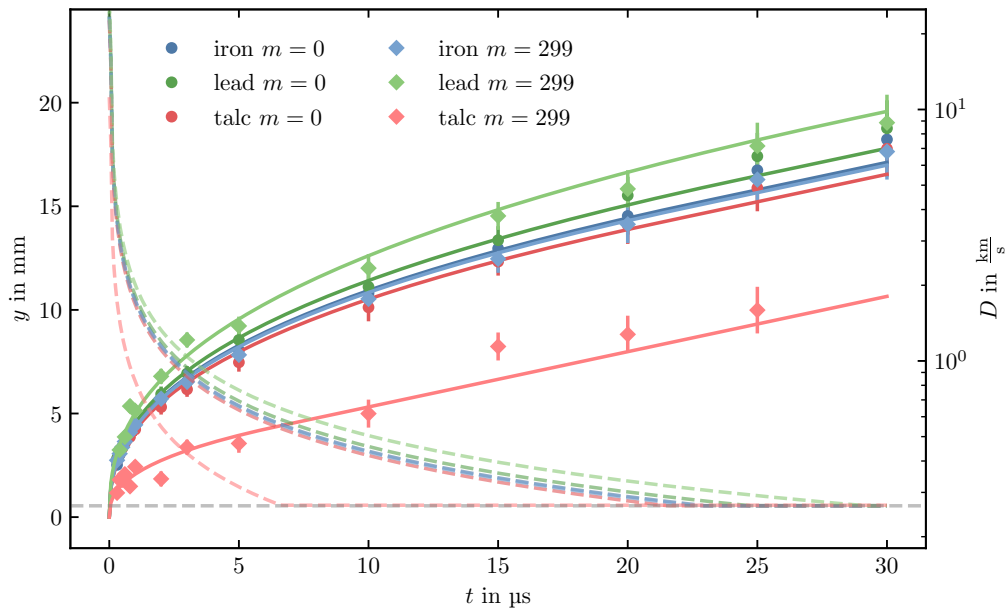


Figure 4.9.: Measurements of the shock front position y over time t for the first $m = 0$ and last shot $m = 299$ in a shot series measurement. The Taylor-Sedov model shows good agreement with all measurements with the exception of the last shot $m = 299$ of talc, where the fit is dominated by the linear part and the data spread is much larger. The derivatives are drawn with dashed lines and show the propagation velocity D of the shock front. The speed of sound is marked with a grey dashed line. The shock wave dynamics for the first shot $m = 0$ are all quite similar. However, the dynamics of the last shots are very different. While the dynamics for the iron target remain relatively unchanged, the measurement on lead shows an increase in expansion velocity and the talc measurement shows a decrease.

shock front for talc becomes distorted roughly after the fifth shot. This effect is especially pronounced in frames captured at early times after plasma ignition and becomes less relevant for later frames. A detailed analysis of the shock front shape is beyond the scope of this thesis.

A plot of the shock front position for all the samples can be found in the appendix in Figure C.4. The geological samples of hematite, magnetite and pyrite show a roughly similar trend to that of iron while the amorphous gypsum target shows a trend comparable with talc.

The shock wave position changes with the shot number and also with the target material, indicating that the shot number and the target material also affect the expansion velocity of the shock wave. This behaviour can be investigated further by combining time and shot series measurements.

4.1.4. Combined Time and Shot Series

The two types of measurements described above can be combined to reveal changes in the shock wave dynamics as a function of the shot number m . By recording shot series at different delay times between $0.3 \mu\text{s} \leq t_{\text{delay}} \leq 30.0 \mu\text{s}$, a data set can be acquired that shows the expansion process for each consecutive laser shot. Since the data from these measurements was analysed manually, only every fiftieth shot was evaluated to stay within reasonable time

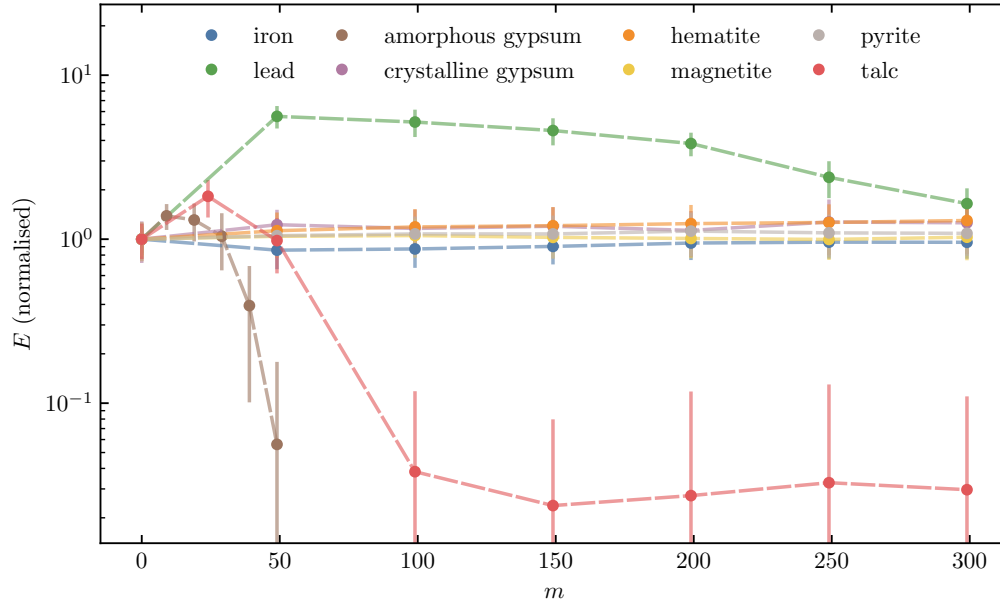


Figure 4.10.: Development of the explosion energy E as a function of the shot number m as determined by the fit parameter $\zeta^5 \propto E$. Each curve was normalised to the first shot's explosion energy. While the energy remains fairly constant for most geological samples and the iron target, talc and amorphous gypsum show a steep decline. For lead, the explosion energy initially increases and falls afterwards. The errorbars indicate the fitting error from the Taylor-Sedov model.

limits.

These combined measurements are shown in Figure 4.9 exemplary for the same three targets presented in Figure 4.8. For each target, the time series from the first shot $m = 0$ and the last shot $m = 299$ are fitted with the Taylor-Sedov model described by Equation 4.1.1. The velocities derived from these fits are also shown as dashed lines of the same colour, and the speed of sound is marked with a grey dashed line.

All curves show good agreement with the Taylor-Sedov model, however the last shot $m = 299$ of talc shows some deviation throughout the entire expansion process and the fit is dominated by the linear part.

While the expansion of the shock wave for the first shot $m = 0$ is very similar for all materials, the dynamics of the last shot $m = 299$ are significantly different. For talc, the shock wave expands more slowly in the last shot, while the expansion velocity for lead actually increases. The dynamics for iron meanwhile do not vary much between the first and the last shot. Changes in between the first and the last shot follow similar patterns as seen in Figure 4.8 for all three samples. The large spread in the lead data observed in the shot series measurements does not impact the quality of the fit significantly. Time series measurements for all analysed shots between the first and last one can be found in the appendix in Figure C.5 for all samples.

As mentioned in Section 4.1.2, for a constant background pressure p_0 and heat capacity ratio γ the fit parameter ζ in the Taylor-Sedov model depends only on the explosion energy

4. Analysis and Results

with $E \propto \zeta^5$. Consequently, ζ^5 can be used to analyse the development of the explosion energy. This parameter is shown in Figure 4.10 for all targets. Each curve was normalised to the first shot, the indicated errors represent the standard deviation of the fitting parameter. For all targets, the curves are similar to the data from the shot series. This is to be expected, since they show quite similar data, namely the change of the shock wave expansion velocity over the course of a shot series when drilling deeper into the sample.

The explosion energy for talc initially rises by a factor of two. After that, the explosion energy decreases rapidly to about 3% of the initial energy and remains relatively constant. Initially, the curve for amorphous gypsum increases as well. Since the crater from the ablation process reached the backside of the target shortly after the fiftieth shot, less data was analysed with a higher resolution of ten shots. The curve peaks at around 1.4 and drops rapidly afterwards with the fiftieth shot showing an explosion energy of about 6% of the first shot's.

For lead, the explosion energy first rises to roughly 6 times its initial value over the first fifty shots. Afterwards, a slow decrease can be observed. The last shot's explosion energy is roughly 1.6 times the initial value.

The explosion energy for iron initially decreases slightly. Afterwards, it rises slowly, approximately to the energy of the first shot.

For the crystalline gypsum sample, hematite, magnetite and pyrite, the explosion energy changes little throughout the entire shot series.

4.2. Acoustic Measurements of a Shot Series

In this section, changes in the acoustic signal over the course of a shot series will be investigated in a way very similar to [7]. The pressure wave is analysed in terms of its acoustic energy E_a . To do this, a quantity $\hat{E}_a \propto E_a$ proportional to the acoustic energy is calculated from Equation 3.5.1.

Figure 4.11 shows the first milliseconds of the normalised acoustic signal from the iron target in a simulated Martian atmosphere measured at a distance of about 60 mm. The signal does not only show the compression and subsequent rarefaction zones of an acoustic wave, but a much longer more complicated pattern with several peaks and troughs. This can be explained by reflections of the sound wave within the simulation chamber. Due to experimental limitations, no measures could be applied to suppress acoustic reflections.

To minimise the effects from reflections on the analysis, \hat{E}_a is calculated by integrating over the square of the first compression wave only. This area is shaded blue in Figure 4.11. The duration of the compression phase is roughly $\Delta t_{\text{com}} \sim 0.1$ ms, corresponding to a length of about $c \cdot \Delta t_{\text{com}} \sim 27$ mm, which is significantly larger than the compression section seen in the bottom of Figure 4.3 with a width of about 8 mm. In this frame taken at 20 μ s after plasma ignition, the shock wave is in the transsonic regime and has travelled about 14 mm. Changes to the pressure wave structure before reaching the microphone at about 60 mm are to be expected.

The compression phases and the calculated development of the acoustic energy in a shot series are shown in the appendix in Figure C.6 exemplary for talc.

For all targets with the exception of the amorphous gypsum sample, a series of 300 shots was recorded simultaneously with the schlieren images discussed in the previous sections.

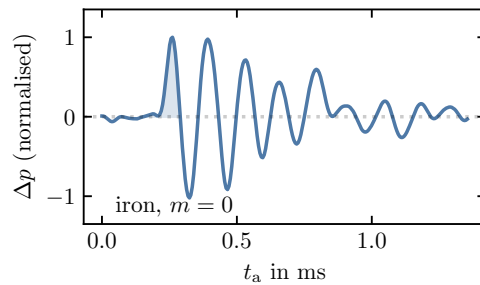


Figure 4.11.: Normalised acoustic signal Δp of the pressure wave over time t_a recorded about 60 mm away from the sample surface. The signal shown here was recorded from the first shot $m = 0$ in a shot series measurement. The acoustic energy is analysed using the integral over the square of the first compression zone. This area is coloured blue.

Only 50 shots were recorded for the amorphous gypsum target. The acoustic energies E_a for these shot series normalised to each target's first shot are presented in Figure 4.12a. From the similar Figure 4.12b with a linear axis, small differences in the beginning of the shot series can be seen more easily.

For iron, the curve remains constant for $m > 10$ for the entire series as already seen for the explosion energy shown in Figure 4.10. The initial rise that was seen previously for lead in the explosion energy is still present in this data for $4 \lesssim m \lesssim 50$ but much less pronounced. After this rise, the acoustic energy decreases throughout the rest of the series. The negative slope is getting smaller for later shots.

For amorphous gypsum, an initial increase of the acoustic energy is followed by a steep decline as seen before in the explosion energy. The slope is also levelling out towards the end of the measurement. A much greater variance in the acoustic energy than for all the other targets can be seen in the measurement of the crystalline gypsum target. Over the first 20 shots, a steep dip is present, after which the signal decreases slowly.

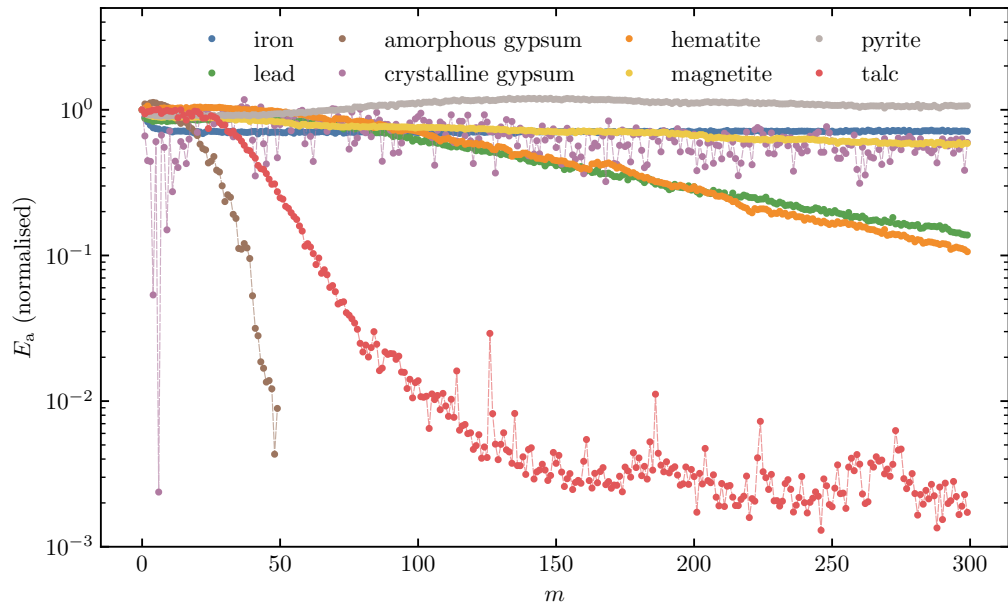
The acoustic energy for hematite rises over the first 20 shots or so. Afterwards, the curve shows a roughly linear decrease until it begins to flatten out at around $m \sim 220$. For magnetite, the acoustic energy decreases rapidly over the first 5 shots, after which it enters an approximately linear decline. The pyrite target meanwhile shows a different behaviour, where the signal increases over the first 150 shots. Afterwards, a roughly linear decline can be observed that appears to flatten out towards the end of the measurement.

The curve from the talc measurement is missing the initial increase that could be observed in the explosion energy in Figure 4.10. However, the following development is quite similar with a steep slope that begins to flatten out around the fiftieth shot. For shots $m \gtrsim 150$, the acoustic energy remains fairly constant at a very low level.

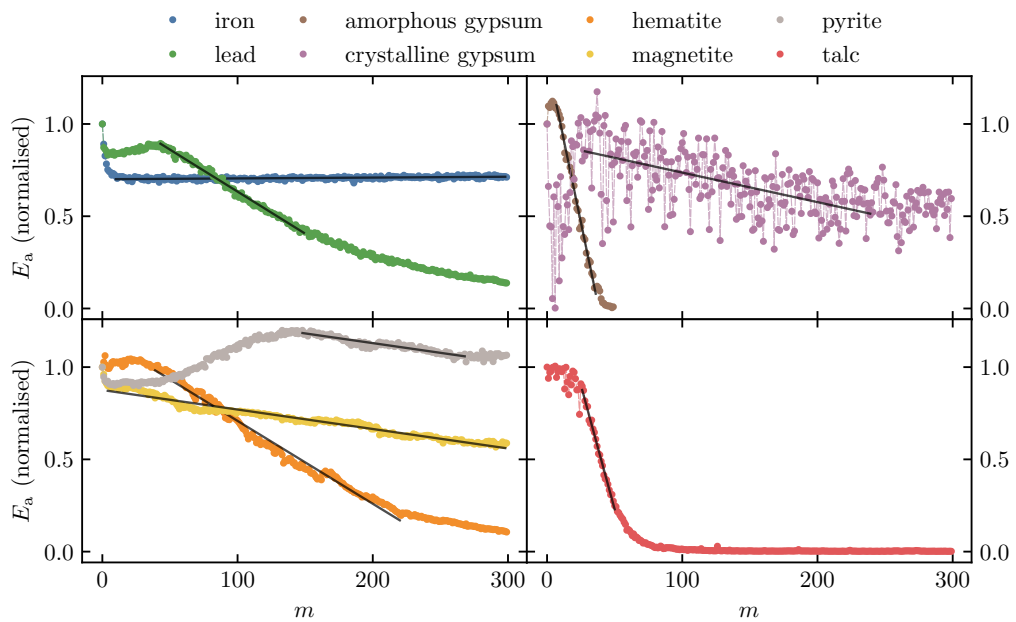
All of these curves are quite dissimilar to the ones reported in [7], even though some of the targets are from the same geological sample. There it was found that all samples except the metallic ones show a linear decrease within the first 30 shots. It should be noted that in the mentioned study, experimental parameters were slightly different with a lower atmospheric pressure of about 0.6 kPa and a lower laser energy of about 10 mJ.

For the non-metallic samples, a correlation between the material's Vickers hardness number HV

4. Analysis and Results



(a) Development of the acoustic energy in logarithmic scale.



(b) Development of the acoustic energy in linear scale with fits.

Figure 4.12.: Development of the acoustic energy E_a as a function of the shot number m . Each curve was normalised to the first shot's acoustic energy. Both figures show the same data, once in logarithmic scale in (a) and once in linear scale in (b). For all samples, the acoustic energy starts decreasing at some point, the onset of this trend however is at different points in the shot series. The linear parts of the decrease were fitted with linear functions as previously done in [7] to investigate a correlation between the decay rate s and the Vickers hardness number HV of the sample. Each measurement was performed once, so no statistical errors are given.

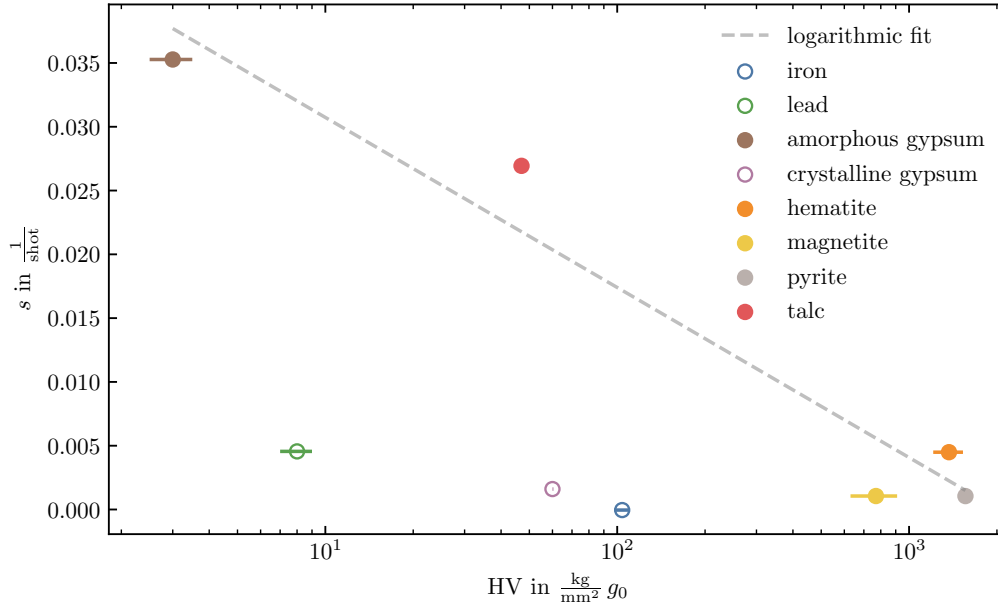


Figure 4.13.: Linear decay rate s of the acoustic energy E as a function of the sample's Vickers hardness number HV. The unit of the commonly used Vickers hardness number HV includes the standard gravity g_0 . The decay rate was calculated from the normalised development of the acoustic energy. The logarithmic correlation seen previously in [7] can be confirmed for the non-metallic samples with the exception of crystalline gypsum. The fit illustrating this correlation was performed on the data with filled markers. Since only one measurement of the decay rate was performed, no standard deviations are given. The errors for the hardness can be found in Table 3.1.

and the slope of a linear function fitted over the first 30 shots was shown in [7].

The data presented here exhibits a somewhat different behaviour. While for all targets some area of the curve shows a roughly linear decline, its onset is much less well defined, as it appears somewhere between $m = 5$ and $m = 150$. Nevertheless, an attempt is made to apply the method from [7] of fitting a linear function to the data. The acoustic data in a linear scale is presented in Figure 4.12b along with the fitted linear functions in black.

The negative slopes s from these fits are shown in Figure 4.13 as a function of the Vickers hardness numbers HV from Table 3.1. Even though the acoustic shot series vary from those presented in [7], the logarithmic correlation between the decay rate s and the Vickers hardness number HV of the non-metallic targets is confirmed by this work's data with the exception of the crystalline gypsum target. The fit in Figure 4.13 illustrating this was performed on the data points with filled markers.

4.3. Spectral Measurements of a Shot Series

Along with acoustic data, spectral measurements are of course also available from LIBS measurements on Mars. Apart from the target composition, its hardness can also be analysed using only spectral data. From the spectral data, plasma temperatures can be calculated showing a linear correlation with the material's hardness for certain alloys [1]. However, the scope of this work is limited to the analysis of changes in the total photon count N_{ph} .

To investigate a possible correlation between the shock wave expansion, the acoustic data and spectral data, all targets were analysed spectroscopically in a simulated Martian atmosphere. Again, a series of 300 shots was used to monitor changes in the signal as a function of the shot number. For the amorphous gypsum target only 50 shots were performed. These measurements were made using the LIBS apparatus with high spectral resolution presented in Section 3.2. All spectra were taken with a delay time between 250 ns and 300 ns after the laser pulse to reduce the amount of continuum emission recorded. The laser energy for these measurements was set to (17.9 ± 0.5) mJ, as close as possible to the laser system's energy used in the previous measurements. To achieve a high signal to noise ratio even at the later stages in a shot series, 30 consecutive shots were averaged for each spectrum, so the first data point corresponds to the averaged spectrum of the shots $0 \leq m \leq 29$ and the last data point to $270 \leq m \leq 299$. Each of these data points shows the average of ten different positions on the target so that each spectrum shown actually corresponds to the average of 300 single spectra in a shot series of 30 shots from 10 positions. Since the total number of shots on a single spot needed to be reduced for the amorphous gypsum sample, spectra from 10 positions were averaged over 10 consecutive shots.

For each of the three exemplary targets iron, lead and talc, the first spectrum corresponding to the shots $0 \leq m \leq 29$ and the last spectrum for $269 \leq m \leq 299$ are presented in Figure 4.14, showing the normalised photon count per wavelength \hat{n}_{ph} . From these spectra, the changes in intensity between the first and the last shots of a series are obvious. The change in intensity is different for these three targets. The relative change in the total photon count N_{ph} , that is the integral over the entire recorded spectrum, is shown in Figure 4.15.

For iron, the total photon count drops to around 60% over the course of the first 120 shots, after which it remains relatively constant. As seen previously in the acoustic and in the shock wave expansion measurements, the curve for lead rises to about 7 times the initial value over the first 60 shots. While this relative change is much larger than what was observed in the acoustic measurements, it is comparable to the rise of the explosion energy with a roughly sixfold increase. Afterwards, the total photon count decreases again throughout the rest of the series with the last shots having a total intensity comparable to that of the first shots'. The total photon count of the talc spectra follows a development similar to that seen in previous measurements with a small rise over the first 30 shots and a subsequent decrease in intensity that is levelling off. Over the last recorded shots, the total intensity is at about 50% of the first shots'.

The amorphous gypsum target shows a steep drop in intensity beginning after the tenth shot. For hematite, magnetite and pyrite the curves remain relatively constant throughout the entire shot series.

It should be noted that due to the delay that was used to reduce the influence of continuum emission in the spectra, not all of the changes in the total plasma emission are covered by these measurements. The effect this could have on the development of the total photon count can not be quantified with the data at hand.

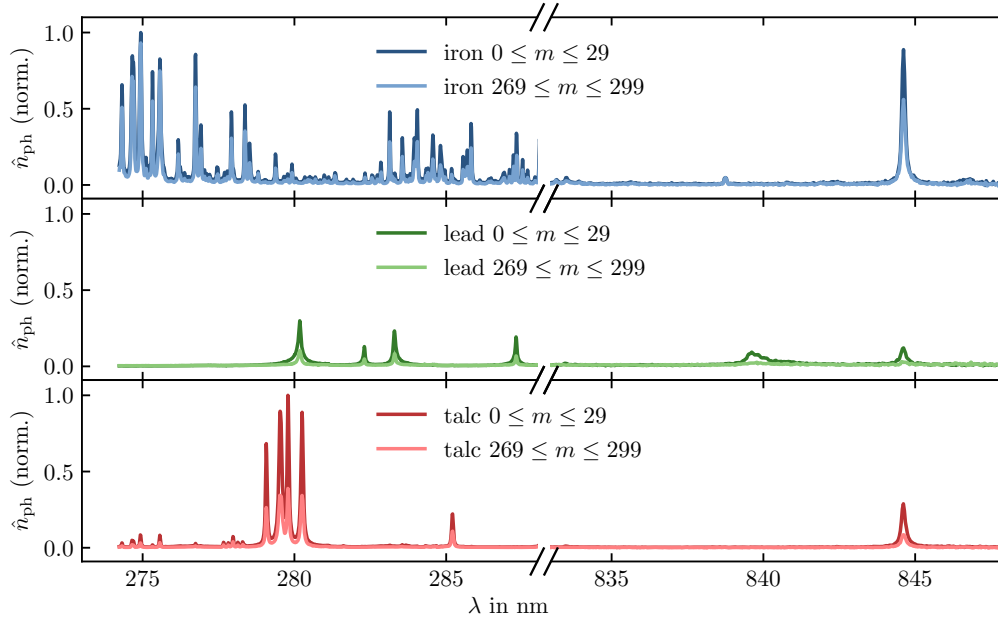


Figure 4.14.: Normalised photon count \hat{n}_{ph} as a function of wavelength λ from LIBS measurements for the first $0 \leq m \leq 29$ and last shots $270 \leq m \leq 299$ in a shot series measurement. Each spectrum was averaged over 30 shots from 10 positions and normalised to its maximum. For lead, this maximum lies in the region that was cut out.

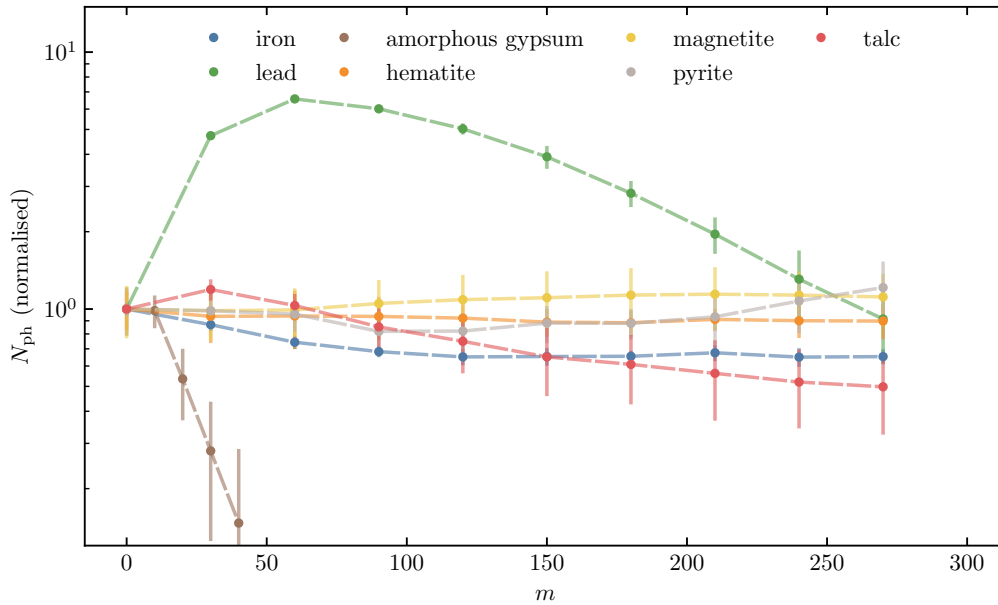


Figure 4.15.: Development of the total photon count N_{ph} as a function of the shot number m under Martian atmospheric conditions. Each curve was normalised to the total photon count of the first 30 measurements. The errors were calculated from the standard deviations of the total intensities between measurements at different spots on the target.

4.4. Comparison and Discussion of the Signal Changes in a Shot Series

When performing a series of LIBS measurements at the same spot on the target, plasma properties and shock wave dynamics change over the course of the measurement. As shown in the previous sections, these changes can be seen in the explosion energy E , the acoustic energy E_a carried by the recorded pressure wave and also in the total photon count N_{ph} of the measured spectra.

In Figure 4.16, a summary of these different parameters for each of the samples is given. The development of the different curves varies with the material under investigation and the considered parameter.

Starting with the metallic materials, for iron all parameters evolve in a very similar way. The drop in the beginning of each parameter is most pronounced in the acoustic energy but can be seen for all parameters. While the relative change in the total photon count N_{ph} is very similar to the change in acoustic energy E_a , the explosion energy E begins to rise again after the first decline, ending at a similar value as it started. A drastically different behaviour can be seen for lead, as the explosion energy and the photon count rise significantly over the first part of the shot series. Note the different scaling needed for lead to fit the entire curve in the figure. The rise in the two curves is comparable and the following decline exhibits a similar behaviour, too. A peak can also be seen in the acoustic data, however it is far less pronounced than the change in the other two parameters.

Generally, for each of the two metallic targets, all curves change in a broadly similar way, however on very different scales.

Moving on to the amorphous gypsum target, the initial development of the photon count remains constant while both other curves first rise to a peak. The following steep decline of the signals is similar for all parameters. For the crystalline gypsum target, the acoustic energy initially drops to almost zero. After rising to approximately its initial value shortly after, it declines constantly throughout the rest of the shot series. The large variation of the acoustic signal is notably different from all other targets. While less pronounced, it is also noticeable in the explosion energy. Note also that while the amorphous gypsum target was pierced after about 50 shots, a complete shot series could be performed on the gypsum crystal. No spectral data was recorded for the crystalline target.

While the development of the parameters for each sample discussed so far shows a broadly similar behaviour, this is not the case for hematite. Here, the acoustic energy initially rises a bit to drop over the rest of the shot series, while the explosion energy is actually increasing throughout. Meanwhile, only a small decline is visible in the photon count. For magnetite, the acoustic energy declines over the entire shot series, while both the explosion energy and the photon count remain fairly constant. In previous studies, an increase in the acoustic energy of hematite over the first few shots was found to be correlated with a phase transition of hematite to magnetite induced by the repeated laser ablation [6, 17, 46]. The lower thermal penetration depth δ_{th} of a magnetite layer on the crater surface was suggested as an explanation of the stronger acoustic signal, since lower heat dissipation leads to a more efficient ablation process.

Pyrite shows a behaviour different from hematite and magnetite, where the acoustic energy rises over the first half of the series and declines over the second half, while the acoustic

4.4. Comparison and Discussion of the Signal Changes in a Shot Series

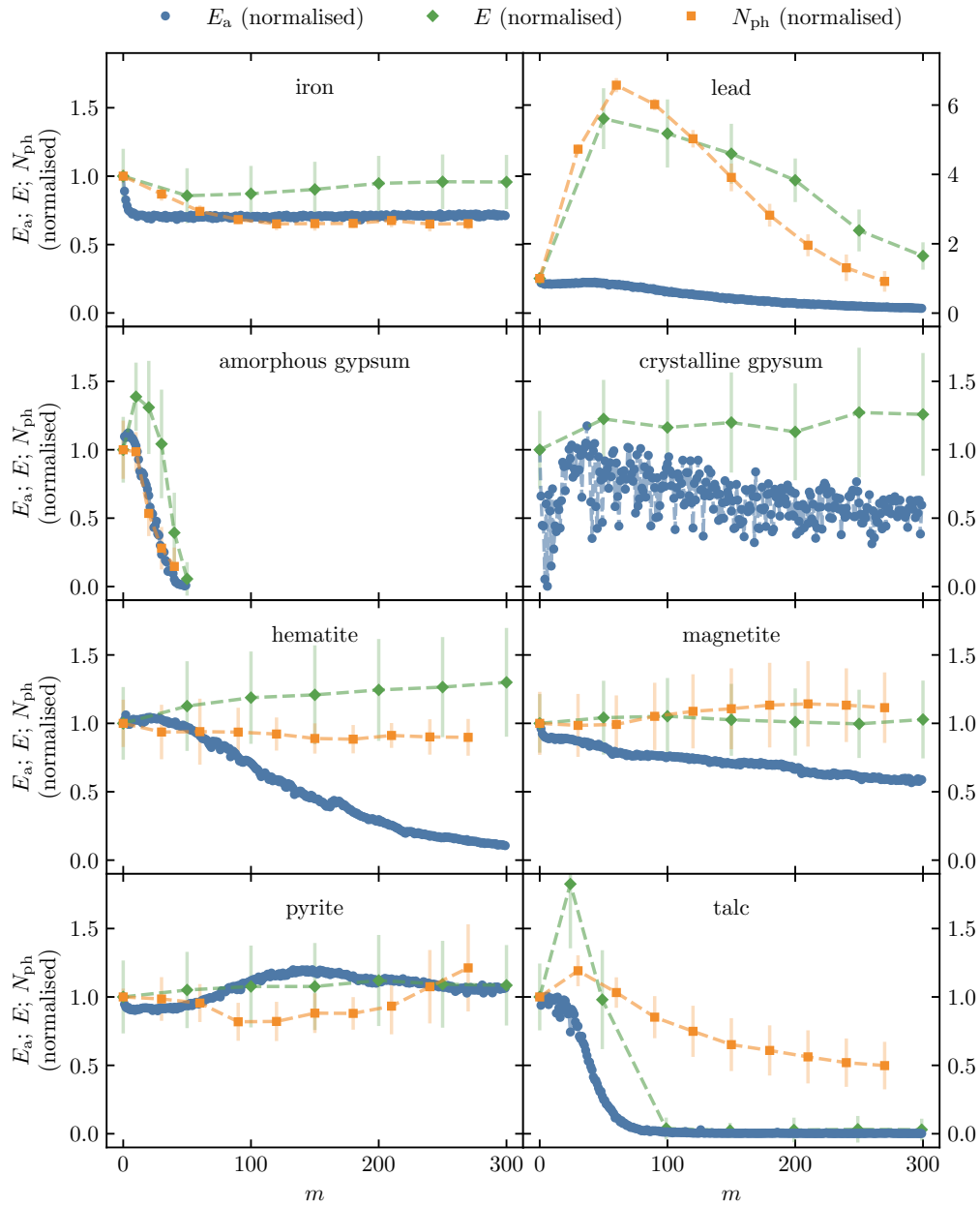


Figure 4.16.: Comparison of the development of the acoustic energy E_a , the explosion energy E and the total photon count N_{ph} in a shot series as a function of the shot number m . All curves are normalised to the value of the first data point. Note the different scale for the lead measurements. No spectral measurements were performed on the crystalline gypsum sample.

4. Analysis and Results

energy of the last shot is greater than that of the first shot. This behaviour can only be seen for the pyrite sample.

For the talc target, the photon count shows a small increase over the first shots and a gentle decline over the rest of the shot series. The initial increase is much more pronounced in the explosion energy, while the acoustic energy stays relatively constant in the beginning. Both parameters show a steep decline to almost zero afterwards, where they stay constant.

The external parameters like the laser energy E_L and background pressure p_0 are approximately the same for all measurements. Differences in the development of the measured parameters between different materials can therefore be attributed to their respective physical and chemical properties and their morphology.

As confirmed in the previous section, the acoustic energy E_a of the emitted pressure wave shows a correlation with the material's hardness and as shown in [8] also with the volume of the crater formed by the ablation process. This correlation however was only shown for non-metallic target materials.

For metallic targets, redeposition of sample material was shown to play an important role in the development of the crater over the course of a series of shots and the ablated volume is generally much smaller when compared to minerals and rocks with the exception of lead, where a lower temperature for a change in the material's state is needed [7, 8, 25, 42].

As described in Section 2.1.2, the sample evaporation process differs for materials depending on their optical and thermal penetration depths δ_{opt} and δ_{th} . For the targets investigated in this work, only for the metallic samples is the thermal penetration depth δ_{th} greater than the optical penetration depth δ_{opt} , as seen in Table 3.1. Surface absorption thus occurs for the metallic targets, while volume absorption can be assumed for some of the geological samples. The type of absorption process impacts the ablation rate of the target and thus the crater volume, as a greater thermal diffusion leads to the loss of some energy into the sample [7, 42].

Differences in material properties lead to varying crater volumes, influencing all parameters measured in this work, as explained in the following.

Acoustic Energy E_a The acoustic energy E_a of the pressure wave can be correlated to the crater volume and the hardness of the material [7, 8].

Total Photon Count N_{ph} Cavity effects of the plasma confined by the crater walls affect the LIBS plasma emission [11]. Among other effects, the confinement of the plasma in the cavity can lead to a higher density and temperature in the plasma and stronger plasma shielding, while the interaction of the plasma with the walls of the crater can help dissipate heat away. This effect was investigated in [7] and [8], where the total photon count N_{ph} over a wide spectral range was analysed.

Explosion Energy E In [55], a correlation between the hardness of concrete, the speed of the shock wave and the ratio of ionic to atomic lines was shown. For softer targets, more of the recoil of the ablated atoms is absorbed in the sample material, leading to a slower speed D of the shock wave and subsequently to reduced ionisation by the detonation wave travelling into the surrounding gas [26]. In the Taylor-Sedov model of a strong point explosion, this speed depends only on the parameter $\zeta^5 \propto E$ of Equation 4.1.1.

4.4. Comparison and Discussion of the Signal Changes in a Shot Series

The developing crater influences all the measured parameters E_a , E and N_{ph} in different ways as can be seen in Figure 4.16. It appears that any one parameter behaves in different ways for different materials. While the acoustic energy E_a appears to be correlated with the explosion energy E for the soft talc target, a very different trend can be seen for the hard hematite target. Here, the explosion energy E grows over the duration of the shot series while the energy transported by the pressure wave E_a declines throughout the series. A decline in acoustic energy also does not necessarily coincide with a decreasing photon count N_{ph} , as can readily be seen in the examples of magnetite and pyrite.

An explanation of these observations must take a multitude of phenomena into account and can not be made with confidence from the data shown in this work. However, a few effects that could be relevant in an explanation shall be mentioned.

While a deepening crater might lead to a more closely confined plasma and a higher pressure driving the shock front away from the target, in a material with good thermal conducting properties more energy can be lost to the bulk material by thermal diffusion, lowering the explosion energy as the crater and with it the surface area interacting with the plasma grows. Furthermore, the material's hardness can influence the shock wave speed by absorbing more or less of the recoil from the ablated particles. This means that relying only on the target's hardness or its thermal properties is insufficient in explaining changes in the explosion energy.

An explanation of a varying photon count must also take changing plasma properties due to confinement into account. Optical and thermal properties of the material also need to be considered.

The lack of a correlation between the development of the explosion energy and the acoustic energy is noteworthy, as both are essentially a result of the pressure driving the expanding plasma.

While all presented parameters show some change over the course of a shot series that is likely caused by material properties, there is no obvious correlation between the parameters, nor a simple correlation with the material's hardness or other characteristics. This leads to the conclusion that caution needs to be taken when normalising LIBS spectra from a shot series to just one of these parameters. A deeper understanding of the relevant mechanisms influencing the development of each parameter is needed and a multitude of effects need to be accounted for.

4.5. Influence of Laser Energy and Ambient Pressure on the Shock Wave Expansion

As is clear from the Taylor-Sedov model, both the explosion energy E and the density of the ambient gas ρ_0 influence the shock wave dynamics. The former can be adjusted by changing the energy E_L of the laser irradiating the target while the latter can be changed by adjusting the atmospheric pressure p_0 inside the simulation chamber.

The influence of both the laser energy E_L and the background pressure p_0 on the expansion of the shock wave are topic of this section. Time series were recorded with the iron target using the schlieren imaging system and evaluated analogous to the data discussed in Section 4.1.2. Each measurement was performed on a pristine spot on the target to avoid crater effects. For all measurements, acoustic data was acquired simultaneously and analysed as described in Section 4.2.

4.5.1. Laser Energy

As mentioned earlier, the laser energy influences the plasma conditions, its dynamics and consequently also the shock wave expansion. The ChemCam and SuperCam instruments currently on Mars achieve laser energies of about 10 mJ and 14 mJ, respectively. Both systems are capable of reducing the laser energy, with SuperCam achieving minimum laser energies of about 3 mJ [36, 64, 65].

To vary the laser energy, different attenuation filters were introduced to the optical path of the laser. Here, three different filters with optical densities of $OD = 0.1$, $OD = 0.3$ and $OD = 0.6$ were used, resulting in laser energies of $E_L = (18.22 \pm 0.22)$ mJ, $E_L = (10.4 \pm 0.3)$ mJ and $E_L = (5.4 \pm 0.5)$ mJ on the sample surface, respectively. All measurements were conducted under Martian atmospheric conditions at a background pressure of $p_0 = (1.01 \pm 0.03)$ kPa.

The effect of changing the laser energy E_L on the shock wave expansion is presented in Figure 4.17a. All curves were fitted with the Taylor-Sedov model from Equation 4.1.1.

With decreasing laser energy, the shock wave expansion slows down as predicted by the model and the speed of sound is reached earlier for lower energies.

In Figure 4.17b, the fit parameter $\zeta^5 \propto E$, which is proportional to the explosion energy, is presented along with the acoustic energy E_a of the pressure wave. The curves for both parameters are normalised to their respective maximum value.

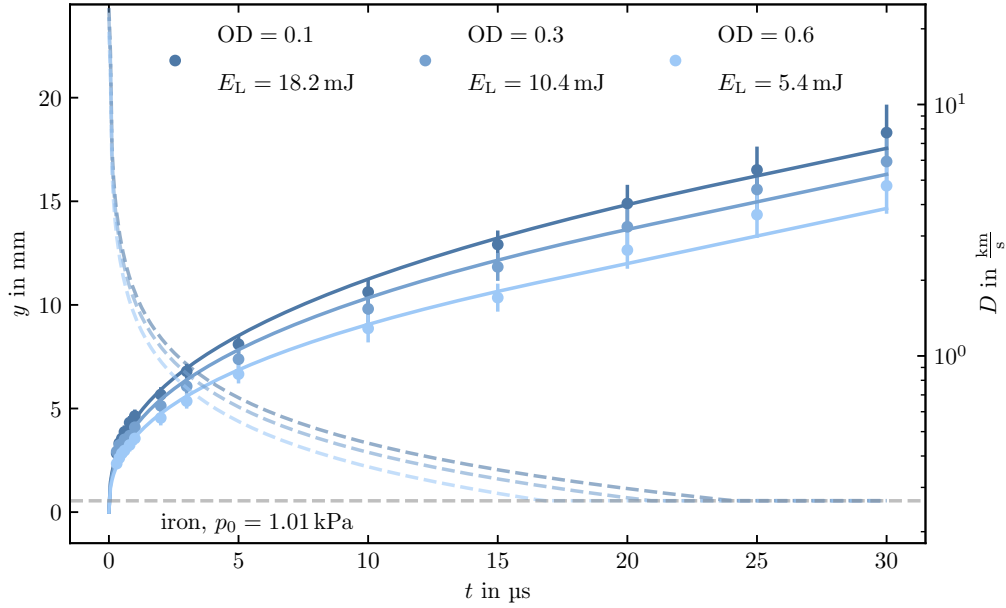
Both parameters grow with increasing laser energy at a comparable rate. While the trend appears to be roughly linear, more data is needed to assess the shape of the curves.

4.5.2. Discussion of the Influence of the Laser Energy

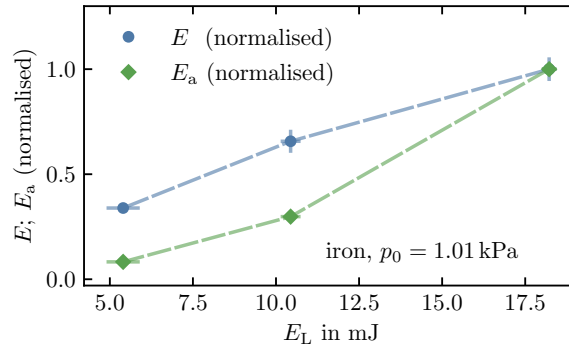
The effect of a changing laser energy on the expansion of the plasma plume has previously been studied in [22], where a strong dependence of the plasma expansion on the laser energy was found. This observation is confirmed by the presented data, as the explosion energy grows with the laser energy.

If the correlation is confirmed to be linear in this regime, then this means that a constant fraction of the laser energy contributes to the expansion of the shock wave. This is supported by [4], where a roughly constant fraction between 50% and 65% of the laser energy was

4.5. Influence of Laser Energy and Ambient Pressure on the Shock Wave Expansion



(a) Shock front position y over time t for different laser energies E_L . The derivatives of the fits are drawn with dashed lines and show the propagation velocity D of the shock front. The speed of sound is marked with a grey dashed line.



(b) Normalised explosion energy E and acoustic energy E_a for different laser energies E_L . Since only one acoustic measurement was performed, no errors are indicated for the acoustic energy.

Figure 4.17.: Influence of the laser energy E_L on the shock wave from an iron target under Martian atmospheric conditions. In accordance with the Taylor-Sedov model, higher laser energies result in a faster expansion of the shock wave. The explosion energy E and the energy of the acoustic wave E_a increase at a comparable rate with growing laser energies.

expended on the shock wave expansion for a laser-induced gas breakdown in a terrestrial atmosphere. In [68], it was found that the laser energy does not influence the plasma temperature or electron density significantly. This was confirmed in [22] and [61], leading the authors to hypothesise that higher laser energies lead to larger plasma plumes with similar average temperatures and densities instead. The data presented in Figure 4.17b is supporting this theory. The influence of the laser energy on the total photon count N_{ph}

4. Analysis and Results

emitted by the plasma was studied in [47], where a linear relation was found for the energy regime covered in this work.

In Section 4.4, no clear relationship between the measured acoustic energy and the explosion energy could be seen. The variation of the laser energy however appears to impact the explosion energy E and the acoustic energy E_a in a similar way, at least for the iron target in the regime covered in this work. This observation suggests that the discrepancy between those two parameters discussed above could indeed be a result of the repeated laser ablation of the same spot.

The presented data shows that the explosion energy changes considerably over the range of laser energies that can be achieved with the SuperCam instrument on Mars.

4.5.3. Ambient Pressure

The effect of a varying ambient pressure p_0 on the shock wave expansion was investigated by adjusting the atmospheric pressure inside the simulation chamber. Over the course of a year, surface pressures on Mars vary between roughly 600 Pa and 1000 Pa [39, 53]. This pressure range is covered by measurements for this thesis, where ambient pressures from as low as 250 Pa to 1000 Pa are investigated to observe pressure dependent trends more clearly. While the ambient pressure was adjusted, the atmospheric composition remained the same.

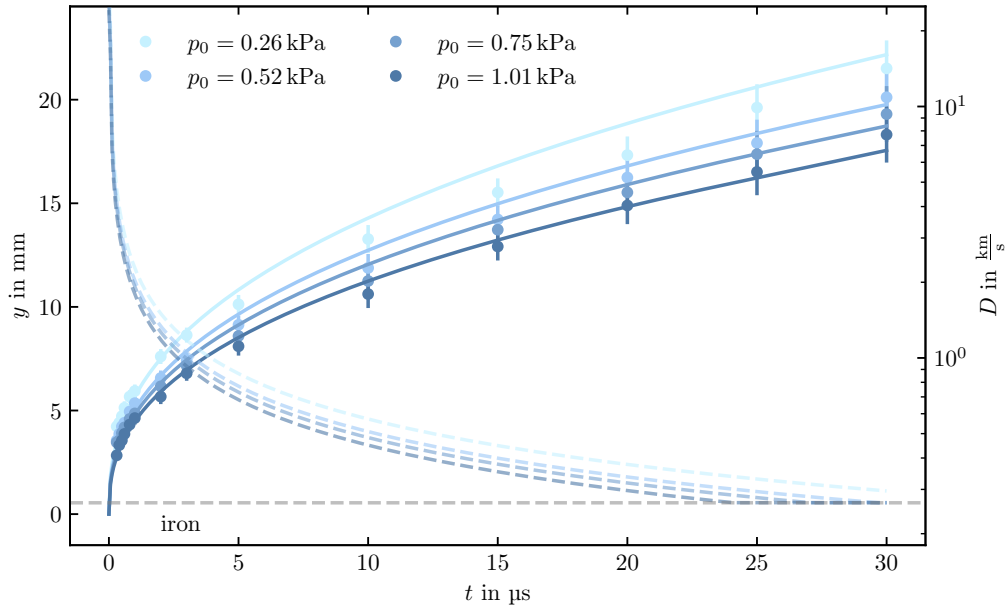
Figure 4.18a shows the time series for an iron target at four different background pressures $p_0 = (0.26 \pm 0.04)$ kPa, $p_0 = (0.520 \pm 0.010)$ kPa, $p_0 = (0.750 \pm 0.010)$ kPa and $p_0 = (1.01 \pm 0.03)$ kPa. Again, the Taylor-Sedov model from Equation 4.1.1 was fitted to the data. In contrast to all previously discussed measurements, the density ρ_0 does in fact vary here. This means that the fit parameter ζ^5 is no longer a tracer for the explosion energy only but instead for its ratio to the ambient gas' density $\zeta^5 \propto \frac{E}{\rho_0}$.

While all fits show good agreement with the data, the fit for $p_0 = (0.26 \pm 0.04)$ kPa shows some deviation. Although the schlieren images taken at lower pressures have lower signal to noise ratios, this does not affect the extraction of the shock position significantly. The discrepancy can likely be explained by statistical errors not analysed in the measurements. With increasing background pressure p_0 , the shock wave expansion is slowed down, which is in accordance with the Taylor-Sedov model as a higher background pressure results in a higher density ρ_0 . Changes in the ablation and heating process due to the greater plasma confinement in an atmosphere with higher pressure likely also play a role, affecting the explosion energy E .

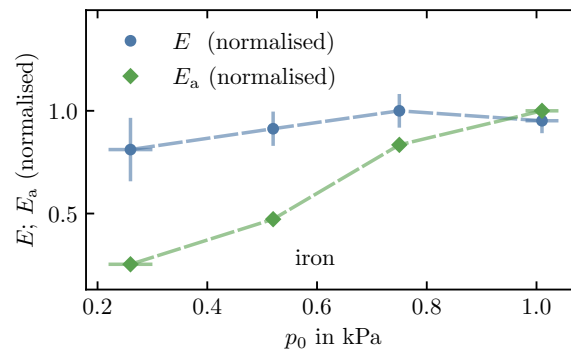
Since the density and pressure of an ideal gas are proportional to one another $p_0 \propto \rho_0$ at constant temperatures, a value proportional to the explosion energy can be calculated from $p_0 \zeta^5 \propto E$. A comparison of the explosion energy E and the acoustic energy E_a is given in Figure 4.18b. Again, both curves are normalised to their respective maximum.

The explosion energy varies little within the tested pressure range while the acoustic energy E_a increases. The acoustic energy E_a shows a roughly linear dependence on the pressure p_0 in this regime, however more data is needed to assess the shape of the curve with confidence.

4.5. Influence of Laser Energy and Ambient Pressure on the Shock Wave Expansion



(a) Shock front position y over time t for different ambient pressures p_0 . The derivatives of the fits are drawn with dashed lines and show the propagation velocity D of the shock front. The speed of sound is marked with a grey dashed line.



(b) Normalised explosion energy E and acoustic energy E_a for different ambient pressures p_0 . Since only one acoustic measurement was performed, no errors are indicated for the acoustic energy.

Figure 4.18.: Influence of the ambient pressure p_0 on the shock wave expansion from an iron target in a simulated Martian atmosphere. In accordance with the Taylor-Sedov model, higher pressures result in a slower expansion of the shock wave. The explosion energy E varies little for the different pressures. A previously found linear relation between the acoustic energy E_a and the ambient pressure is confirmed by this data [7].

4.5.4. Discussion of the Influence of the Ambient Pressure

The decreasing expansion velocity D of the shock wave with increasing pressures as seen in Figure 4.18a can readily be explained with the Taylor-Sedov model. Since the background pressure p_0 and the background density ρ_0 in an ideal gas are proportional to one another

4. Analysis and Results

at constant temperatures like in this scenario, Equation 2.2.7 shows that the shock wave expansion proceeds more slowly for higher pressures.

However, processes relevant to the generation and heating of the laser-induced plasma also change with the ambient pressure. In [30] it was found that a decrease in ambient pressure results in a lower electron density in the pressure range from 0.1 kPa to 10 kPa, reducing the effects of plasma shielding. A reduced line intensity was also correlated with a reduction in ambient pressure.

Figure 4.18b shows that the explosion energy calculated from the fit parameter $p_0 \zeta^5 \propto E$ does not vary significantly with the ambient pressure. In a simple model where no plasma shielding occurs, the explosion energy can be expected to stay roughly constant for different pressures. When plasma shielding effects are present, higher pressures could lead to a direct heating of the plasma, increasing the energy available for its expansion and the subsequent shock wave. In the presented data, the initial slight increase in explosion energy between 0.26 kPa and 0.75 kPa could be an indication for this behaviour. The increase however is smaller than the error of the data, so a larger data set with higher fidelity is needed to study the possible influence of plasma shielding.

The increase in acoustic energy with increasing background pressure is likely a result of a stronger shock wave in a denser atmosphere as suggested in [7]. This behaviour is also suggested by Equation 2.2.4, which shows that the ratio of the densities on both sides of the shock is constant. This means that a higher background pressure leads to a higher shock pressure for strong shock waves. The stronger shock wave also results in an increased contrast in the schlieren images, which can be seen in the exemplary pictures presented in Figure C.7 in the appendix.

A linear relation between the acoustic signal and the background pressure was previously found in [7] for pressures between 0.2 kPa and 0.8 kPa. The data presented in Figure 4.18b confirms this result.

Surface pressures on Mars can change by about 100 Pa over the course of a Sol, while pressure changes over a year can be on the order of 400 Pa. The shock wave dynamics and the acoustic energy change notably over these pressure ranges, so the ambient pressure needs to be considered when measurements are compared.

5. Conclusion and Outlook

To investigate possible correlations between the acoustic and the spectral data from a LIBS measurement with the expansion dynamics of the shock wave induced by the ablation process, a new schlieren system capable of imaging density gradients was designed and built for this work along with a microphone system to monitor the acoustic signal. The schlieren imaging system was demonstrated to achieve sufficient contrast to analyse shock wave dynamics in the low density environment of a simulated Martian atmosphere at around 1 kPa. Schlieren images of laser-induced shock waves under Martian atmospheric conditions were presented in this thesis for the first time.

At higher atmospheric pressures, the system is capable of resolving additional features within the expanding shock wave. These features were attributed to reflections of the shock wave. The density distribution of the shock wave under Martian atmospheric conditions along an axis perpendicular to the target surface showed a low density region in the center. The width of the shock front grew larger with time. While both observations are in agreement with theoretical considerations and computational simulations [51, 69], they should be treated carefully, since the schlieren system is subject to significant instrumental errors.

To investigate the dynamics of the expanding shock wave, a series of images at successive time delays after plasma ignition was recorded. The early phase of the shock wave expansion could be described by the Taylor-Sedov model, which has been applied successfully to laser-induced shock waves under terrestrial atmospheric conditions in previous works [22]. A linear model was successfully fitted to the data acquired at later times to account for the propagation velocity of the weak shock wave with the speed of sound. The shock wave from an iron target reached the speed of sound at around 15 mm from the target surface in Martian atmospheric conditions, which corresponds to a time of about 23 μ s after plasma ignition.

The decoupling of the shock wave from the emitting plasma in a Martian atmosphere was investigated for an iron sample using a plasma imaging system. By comparing the shock front position with the leading edge of the plasma emission, the decoupling was found to occur between 400 ns and 500 ns after plasma ignition, which corresponds to a position of about 3 mm from the sample surface. In accordance with previous studies under terrestrial atmospheric conditions, the plasma emission was found to be ahead of the shock wave at early times < 400 ns, which could be explained with the radiation wave mechanism [22].

A possible correlation between the acoustic signal and the shock wave dynamics was investigated by comparing the development of the explosion energy to the change of the acoustic energy of the pressure wave over the course of a series of laser shots at the same position on the target. The explosion energy E was determined from the only fit parameter ζ in the Taylor-Sedov model and the acoustic energy E_a was determined by integrating over the square of the first compression signal recorded with the microphone.

While a previously discovered correlation between the decrease in the acoustic energy over the course of a shot series and the material's hardness could be confirmed for most geological samples, no obvious correlation between the acoustic signal and the explosion energy was

5. Conclusion and Outlook

found [7].

The development of these parameters was also compared to the total photon count N_{ph} in the range from ultraviolet to infrared. Again, no clear correlation between the measured parameters or material properties was found.

Changes to all parameters were attributed to material properties and the crater morphology. Some mechanisms possibly leading to these changes were discussed, including plasma confinement by the ablation crater and thermal diffusion.

Finally, the influence of external parameters on the shock wave dynamics and the acoustic signal was investigated. The laser energy E_L was varied between 5 mJ and 18 mJ. These energies are comparable to those used for measurements conducted with the ChemCam and SuperCam instruments on Mars. It was found that an increase in laser energy leads to a faster expansion of the shock wave, confirming previous studies [22]. The rise in the explosion energy with increasing laser energy was comparable to changes in the recorded acoustic energy.

The background pressure p_0 was varied between 0.26 kPa and 1.01 kPa to study the influence of the changing atmospheric pressures on Mars. An increase in background pressure was found to slow down the expansion of the shock wave, which is in accordance with the Taylor-Sedov model. Changes in the ambient pressure were shown to have little impact on the explosion energy. Small variations could be a result of increased plasma shielding at higher pressures. A higher atmospheric pressure was also found to correlate with a higher acoustic energy, confirming previous studies [7]. Changes in the shock wave dynamics and acoustic signal were notable over the pressure range relevant for diurnal and seasonal pressure fluctuations on Mars.

While a relation between the energy of the acoustic wave emitted from the laser ablation process and the material's hardness could be confirmed, no clear correlation between the acoustic energy, the explosion energy and the total photon count was found. This work shows that material properties can have opposite effects on the different investigated parameters. To evaluate the acoustic signal in the context of its use to normalise Martian LIBS data, it has to be studied in greater depth on a bigger sample set relevant for Martian targets. Moreover, a complete model of the plasma expansion needs to take several effects of the interaction between the laser, the target, the plasma and the ambient atmosphere into account.

The schlieren system realised in this work can support the investigation of relevant effects from the cratering process. The irregular shock wave geometries observed for some of the samples should be investigated further as they can give insight into ablation processes and mechanisms in the shock wave formation. More studies on the impact of material parameters on measuring parameters for a narrower selection of targets are planned. A calibration of the schlieren images for a spatially varying contrast should be implemented for future measurements. Improving the schlieren system by eliminating or reducing the inhomogeneity of the background illumination and increasing the system's contrast could allow for a quantitative evaluation of the density gradient. This could give further insight into the mechanisms involved in the generation of the acoustic pressure wave and thus the discrepancy between the development of the acoustic energy and the explosion energy found in the shot series measurements.

Acknowledgements

First, I would like to thank the head of the Institute of Optical Sensor Systems at the Deutsches Zentrum für Luft- und Raumfahrt, Prof. Dr. Heinz-Wilhelm Hübers, and the head of the department for Terahertz and Laser Spectroscopy, Prof. Dr. Michael Gensch, for their support and the opportunity of performing the research for this thesis under their supervision.

Furthermore, I want to thank the head of my research group, Dr. Susanne Schröder, for assisting me in my work with her great knowledge in the field of laser-induced breakdown spectroscopy for space exploration and also for the opportunity to work on other exciting projects.

I want to express special gratitude towards my colleague Dr. David Vogt, who supported me almost every day in the laboratory, both professionally and morally. His thoughtful questions and constructive criticism helped me improve my research greatly.

I would also like to thank my colleague Peder Bagge Hansen, who provided valuable insight into the theoretical aspects of LIBS and was a great partner for productive and entertaining discussions.

Furthermore, I want to thank Dr. Enrico Dietz, whose experience and technical expertise helped me in the design of the schlieren imaging system.

Finally, I want to thank my friends Timo Dörries, Lucas Kluge and Paul Müller and my family. They are always supportive and helped me find my way to where I am right now. Special thanks go to my father Christian Seel for his help in the construction of the acoustic recording system.

A. Appendix: Theory

A.1. Plasma Properties

The knowledge of plasma properties can be of great importance for the modelling and analytical evaluation of the plasma's emission. All plasma properties discussed here depend on the location within the plasma and change with time. If properties like temperature or electron density are to be calculated from spectral data, some considerations need to be made in the experimental setup. Information on this can be found in [30] and [51]. Much of this section relies on the work in [14].

Local Thermodynamic Equilibrium When describing laser-induced plasmas analytically for modelling the plasma emission or to determine the concentration of specimen without calibration targets, the existence of a local thermodynamic equilibrium is often assumed, to reduce the complexity of the many processes involved in the plasma emission [14].

In a LIBS plasma, thermodynamic conditions change fast and vary spatially, so care needs to be taken when a thermodynamic approach is used to calculate plasma properties or compositions. For dynamic laser-induced plasmas, the timescales at which different particle's interactions happen span several orders of magnitude. The time between electron-electron interactions τ_e for example is on the order of 1×10^{-12} s, while the collision time between electrons and neutral particles τ_{n-e} is closer to 10×10^{-9} s*. This means that within the plasma's lifetime of about $\tau_{\text{plasma}} \sim 1 \times 10^{-6}$ s the relaxation times vary significantly for different kinds of interaction.

After some time $\tau_{e,0}$ however, the population density of the neutral particles' discrete energy levels can be described by the Boltzmann statistics with an electron equilibrium temperature T_e .

For an ideal stationary and homogeneous optically thin plasma, a local thermodynamic equilibrium (LTE) can be reached if the probability of a collision induced electron transition from energy level m to a higher level j is much greater than the probability for a radiative energy level transition from j to m . In other words, for a given energy level transition collisional excitations have to be much more likely than spontaneous radiative decay.

From the inequality

$$N_m \sum_{j>m} X_{mj} \gg \sum_{j>m} N_j A_{jm} \quad (\text{A.1.1})$$

with the populations N_m and N_j , the collisional excitation rate X_{mj} and the radiative decay rate A_{jm} , the McWhirter criterion

$$n_e > 1.6 \times 10^{12} \sqrt{T} (\Delta E_{nm})^3 \quad (\text{A.1.2})$$

*These times were measured in a LIBS plasma under terrestrial atmospheric conditions.

A. Appendix: Theory

can be derived, with the electron density in $[n_e] = \frac{1}{\text{cm}^3}$, the temperature $[T] = \text{K}$ and the difference in energy $[\Delta E_{nm}] = \text{eV}$ of levels n and m . The McWhirter criterion must hold for the largest gap ΔE_{nm} between two adjacent levels, so the ground level and the first excited level are usually considered. This kind of plasma is referred to as an electron excitation kinetic plasma [14].

For plasmas used in LIBS, measuring or calculating the electron density n_e however is only a necessary, not a sufficient criterion. Whether or not LTE is a valid assumption for a given plasma can and should be checked using other complementing criteria. Considering the equilibrium for different kinds of inelastic processes in LIBS plasmas, as well as the temporal and spatial changes within the plasma are of great importance, especially for plasmas under reduced atmospheric pressures [14].

Temperature In a system in thermodynamic equilibrium, equilibrium distributions for all particles can be characterised by the same temperature. For a LIBS plasma, this includes the distributions of electrons, atoms, ions and the radiation. Since the plasma does not radiate black-body radiation, the plasma can not be in a complete thermodynamic equilibrium. For a plasma in LTE, this means that the temperatures for heavy particles T_H and electrons T_e are the same, characterised by the excitation temperature T_{exc} of the distribution of atomic states, while the temperature for the radiation field T_ν is different.

$$T_{\text{exc}} = T_H = T_e \neq T_\nu \quad (\text{A.1.3})$$

If the assumption of LTE is verified as stated in the paragraph above concerning LTE, the excitation temperature of the plasma can be calculated from the spectrum using the method of Boltzmann or Saha-Boltzmann plots [20].

For a plasma in LTE, the distribution of atomic states is described by the Boltzmann distribution

$$\frac{N_n}{N} = \frac{g_n e^{-\frac{E_n}{kT}}}{Z(T)} \quad (\text{A.1.4})$$

with the population N_n , energy E_n and degeneracy g_n of the quantum level n , the Boltzmann constant k , the temperature T , the temperature dependent partition function $Z(T)$ and the total number density of the species N .

This equation can be rearranged and plotted for different energy levels. The slope of a fit through the resulting data set then reveals the excitation temperature T_{exc} . A similar approach can be taken for ionic states using the Saha-Eggert equation so that ionic emission lines can be included to achieve a more precise value for the temperature. This type of plot is called Saha-Boltzmann plot.

Electron Density As explained earlier, the electron density n_e in a plasma can be used as a necessary criterion to determine whether or not LTE may exist.

The Stark broadening mechanism can be exploited to calculate the plasma's electron density from the linewidth of an emission line. This is a well established and simple to use method employed in plasma research [18, 30].

The hydrogen lines of the Balmer series are especially important for this, since the Stark

effect for hydrogen is linear. Gigoso et al. found the relation

$$\text{FWHA}_{H_\alpha} = 0.549 \text{ nm} \times \left(\frac{n_e}{10^{23} \frac{1}{\text{m}^3}} \right)^{0.67965} \quad (\text{A.1.5})$$

between the full width at half area (FWHA) of the Balmer alpha line H_α and the electron number density n_e [18].

A detailed study on the distribution and evolution of plasma parameters can be found in [51].

The crater resulting from repeated LIBS measurements at the same position changes the interaction between the laser and the sample, which also influences the plasma properties.

B. Appendix: Setup

B.1. Derivation of the Maximum Angle of Deflection

The maximum angle that light rays get deflected by a schlieren object θ_{\max} can be estimated by considering a spherical gas bubble of refractive index n where the greatest refraction occurs at the periphery of the bubble [49].

$$\theta_{\max} = 2\left(\frac{n}{n_0} - 1\right) \quad (\text{B.1.1})$$

According to the Gladstone-Dale relation

$$n - 1 = k \rho, \quad (\text{B.1.2})$$

the refractive index depends linearly on the density ρ of the medium with k being a gas and wavelength depended constant [49].

This relationship leads to

$$\frac{n}{n_0} = \frac{1}{n_0} + \frac{\rho}{\rho_0} \left(\frac{n_0 - 1}{n_0}\right). \quad (\text{B.1.3})$$

To determine the maximum angle of deflection for Martian atmospheric conditions, the density of the gas that is compressed by the shock wave needs to be known. Assuming an ideal gas and a pure CO₂ atmosphere one can estimate the specific volume ratio of the shock wave from the Hugoniot relations [69] in the limit of a strong shock $p_1 \gg \frac{\gamma+1}{\gamma-1} p_0$ with the adiabatic exponent γ and the pressures p from

$$\frac{V_1}{V_0} = \frac{(\gamma - 1)p_1 + (\gamma + 1)p_0}{(\gamma + 1)p_1 + (\gamma - 1)p_0} \approx \frac{\gamma - 1}{\gamma + 1}. \quad (\text{B.1.4})$$

Assuming a constant number of particles and with $\gamma = \frac{9}{7}$ * it follows that

$$\frac{\rho_1}{\rho_0} = \frac{\gamma + 1}{\gamma - 1} = 8 \quad (\text{B.1.5})$$

and

$$\frac{n}{n_0} = \frac{8n_0 - 7}{n_0}. \quad (\text{B.1.6})$$

Assuming a refractive index of $n_0 - 1 = 5.7 \times 10^{-7}$ [37], equation B.1.1 yields a maximum angle $\theta_{\max} = 7.5 \times 10^{-6} \text{ rad} = 4.3 \times 10^{-4} \text{ }^\circ = 1.6 \text{ arcseconds}$.

* $\gamma = \frac{f+2}{f}$ with $f = 3N - r$ with $N = 3$ atoms and $r = 2$ bonds

B.2. Schlieren Imaging System

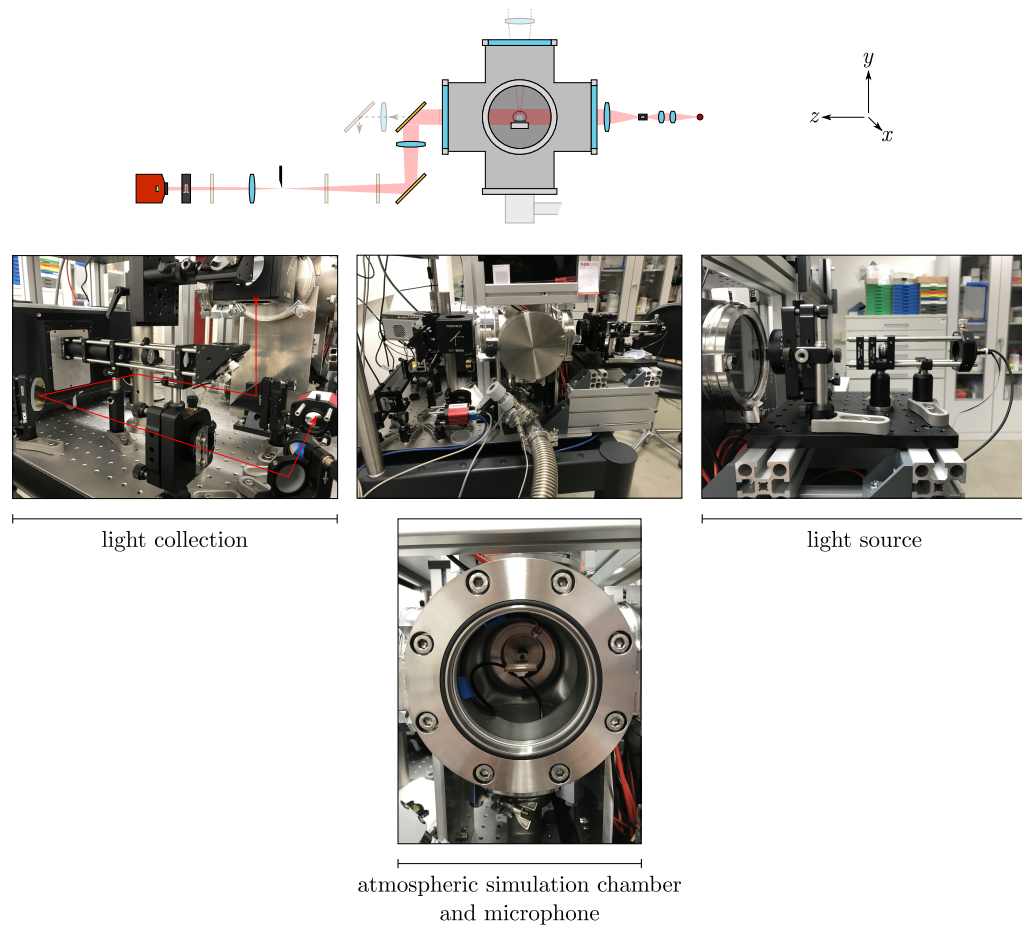


Figure B.1.: Photos of the schlieren imaging system. The upper row shows the optics of the light source on the right side, an overview image of the entire schlieren system in the middle and the light collection and contrast optics on the left. The red line marks the optical path. In the lower image, the open atmospheric simulation chamber with the sample holder and the microphone can be seen. The closed atmospheric simulation chamber can be seen in the center of the overview image. The schematics of the schlieren imaging system are also shown for reference.

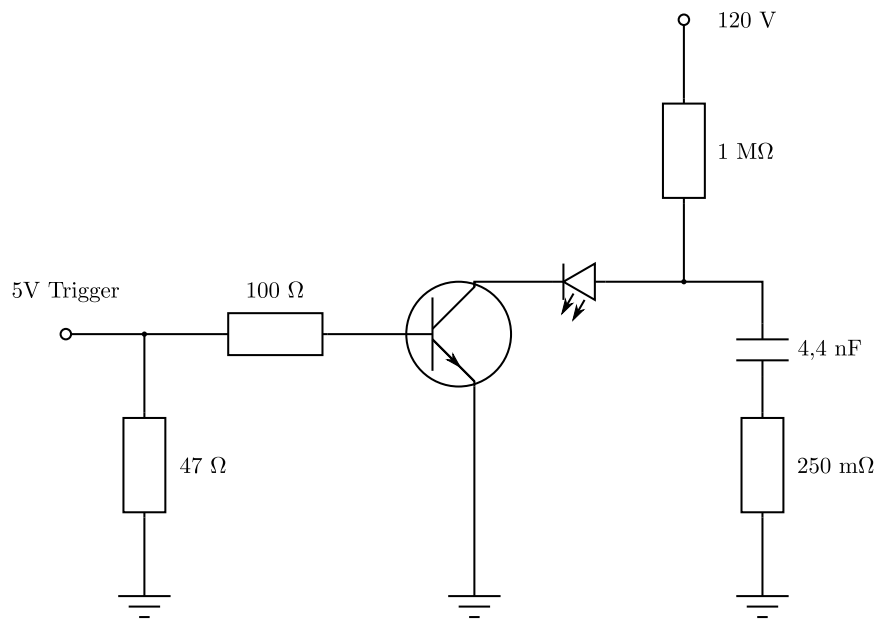


Figure B.2.: Circuit diagram of the avalanche pulse generator used to drive the light source in the schlieren imaging system. It was designed and built by Enrico Dietz of the Deutsches Zentrum für Luft- und Raumfahrt, who also provided the schematics. The duration of the light source pulses achieved with this circuit is around $\Delta t_{ls} \approx 40$ ns.

C. Appendix: Results

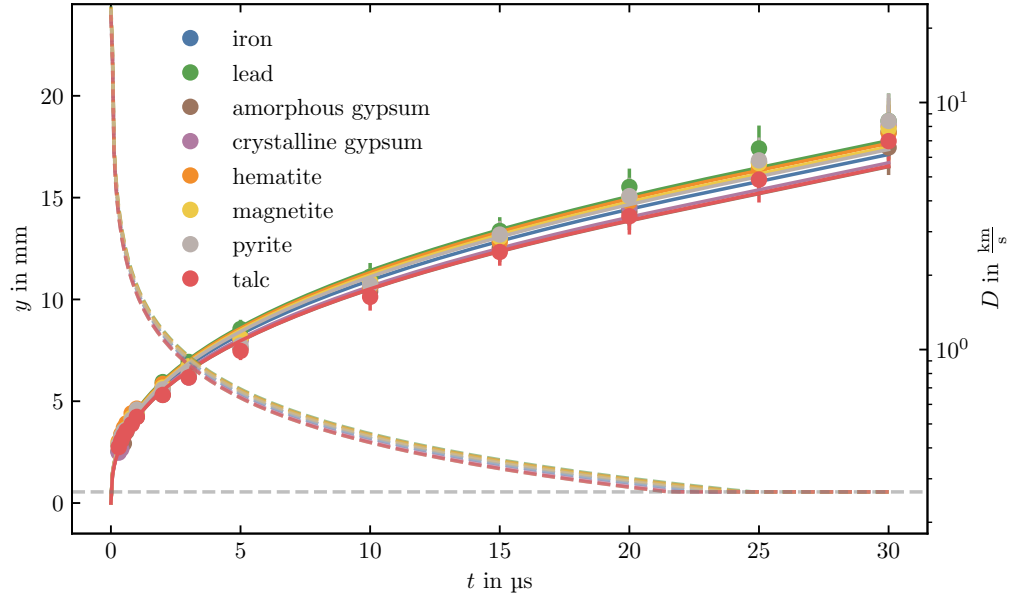


Figure C.1.: Shock front position y as a function of time t from schlieren measurements for all targets under Martian atmospheric conditions. The Taylor-Sedov model from equation 4.1.1 was fitted to the data, showing good agreement for all samples. The derivatives of the fit functions give the expansion velocities D of the shock wave and are shown as dashed lines in the same color as the corresponding target. The dashed grey line marks the speed of sound. All sample materials show a very similar expansion behaviour with only little deviations that are within the error margins.

C. Appendix: Results

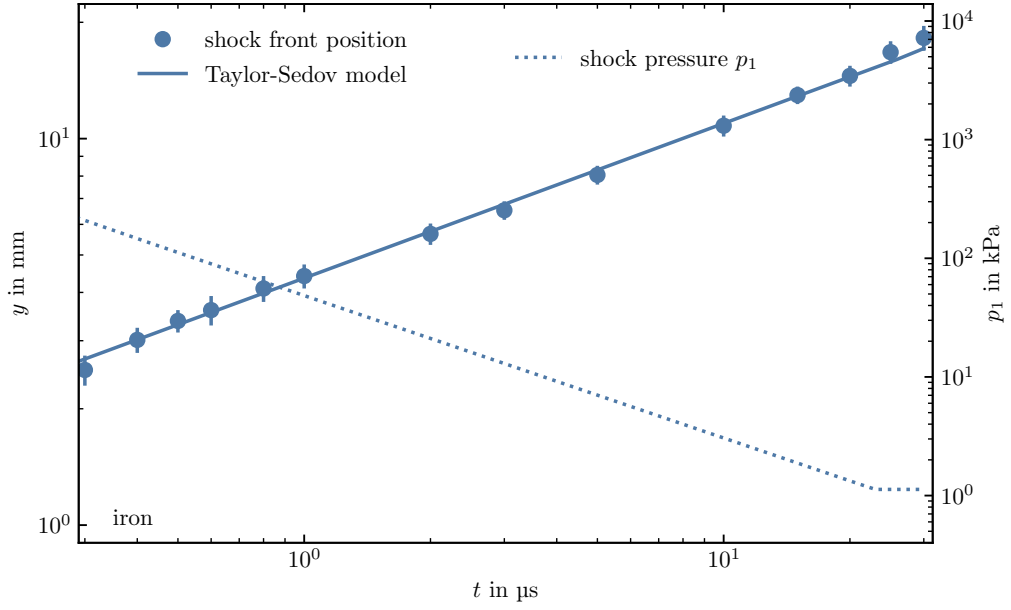


Figure C.2.: Position of the shock front y and pressure p_1 behind the shock front over time t as calculated from equation 2.2.8 for an iron sample under Martian atmospheric conditions. The right axis showing the pressure refers to the dashed lines. The relative pressure changes are comparable to those shown under terrestrial atmospheric conditions in [22], however the decay is slower. This can be attributed to the low pressure of the simulated Martian atmosphere.

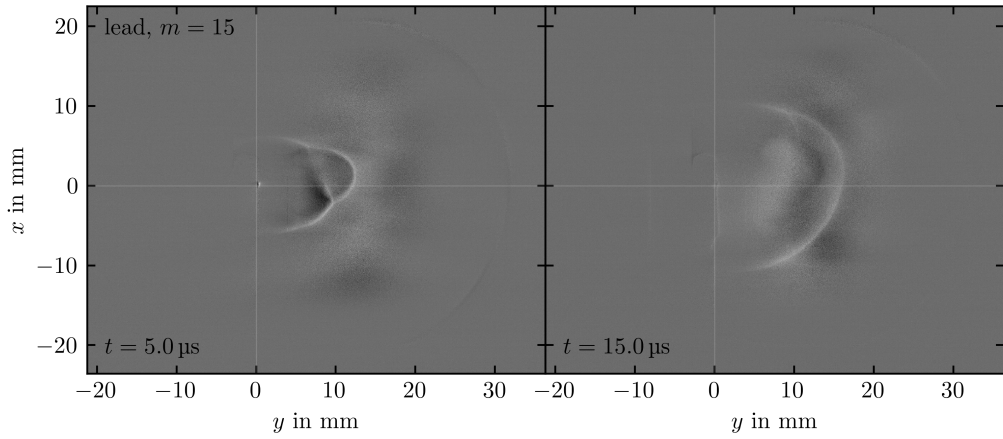


Figure C.3.: Exemplary pictures of irregular shock wave structures formed from a lead target under Martian atmospheric conditions. The irregular shape begins to form at shot numbers $m \gtrsim 11$. At early times shown in the left frame at $t \lesssim 10 \mu\text{s}$, a double structure can be observed. At later times $t \gtrsim 15 \mu\text{s}$, the shock front assumes an approximately elliptical shape.

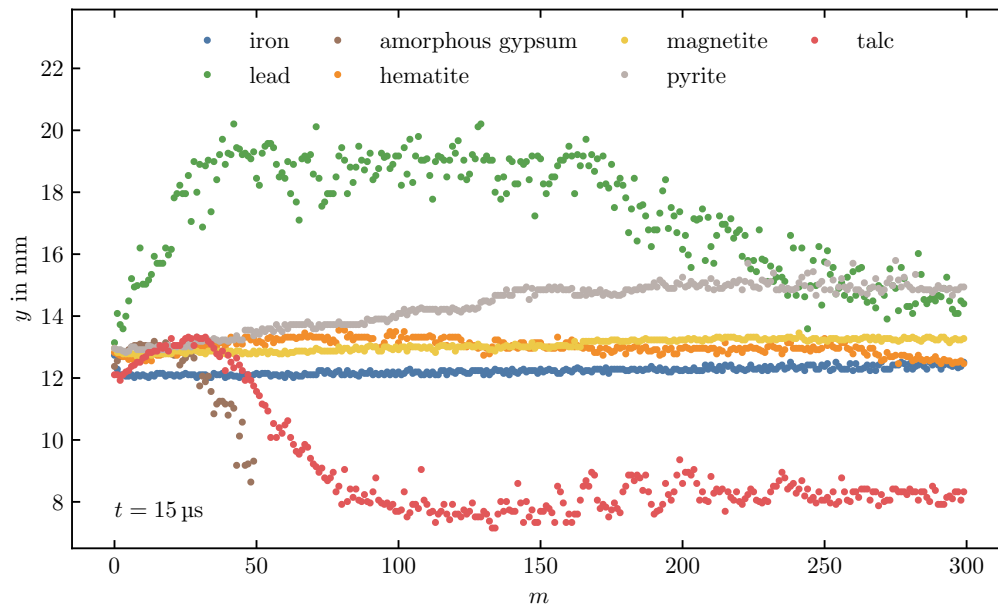


Figure C.4.: Development of the shock front position y at $t = 15 \mu\text{s}$ after plasma ignition as a function of the shot number m for all samples except the crystalline gypsum target in a simulated Martian atmosphere. Due to the large variance in the position, the computer-aided extraction of the shock front position was not possible for this sample.

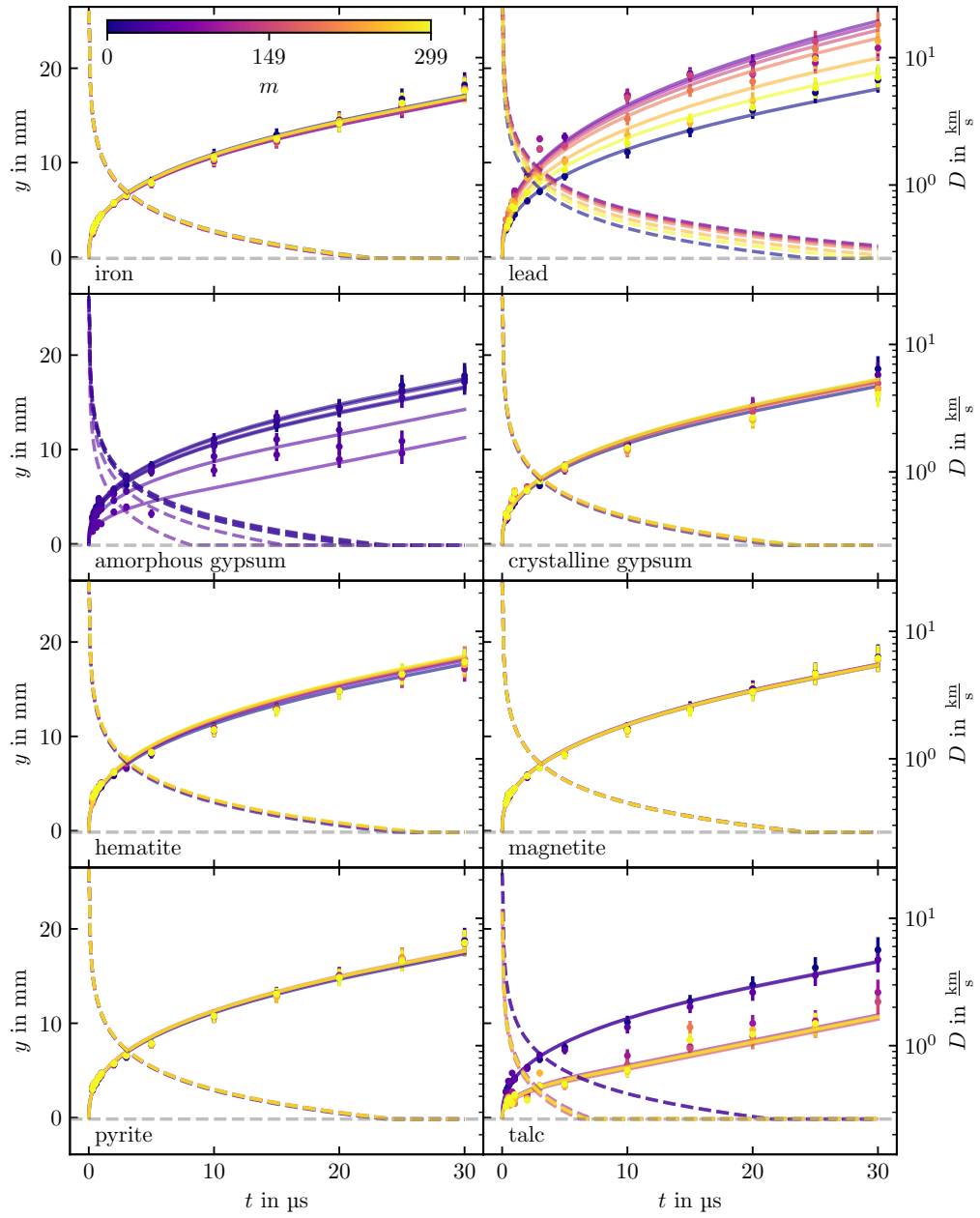


Figure C.5.: Combined time and shot series measurements in a simulated Martian atmosphere for all samples with fits. The plots show the development of the shock front position y over time t . The color of each measurement represents the shot number m in the shot series. The parameter ζ extracted from these fits is used to calculate the explosion energy E . The derivatives of the fits are drawn with dashed lines and show the propagation velocity D of the shock front. The speed of sound is marked with a grey dashed line.

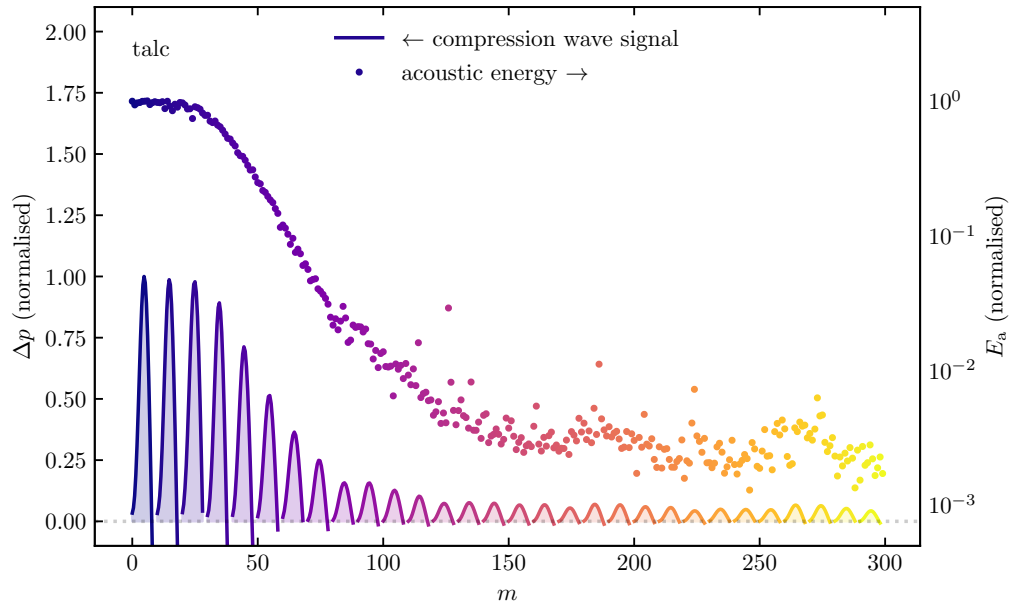


Figure C.6.: Pressure of the acoustic wave Δp from an acoustic shot series measurement of talc in a simulated Martian atmosphere and the calculated acoustic energy E_a as functions of the shot number m . The left axis refers to the pressure signals of the acoustic waves shown as solid lines. The first compression phase of every tenth shot is shown, illustrating the temporal change of the pressure. Each compression phase shows the development within about 0.1 ms. The right axis refers to the acoustic energy marked with dots as calculated from this compression phase. Both the sound pressure Δp and the acoustic energy E_a were normalised to the value of the first shot. The shot numbers are color coded from blue for $m = 0$ to yellow for $m = 299$.

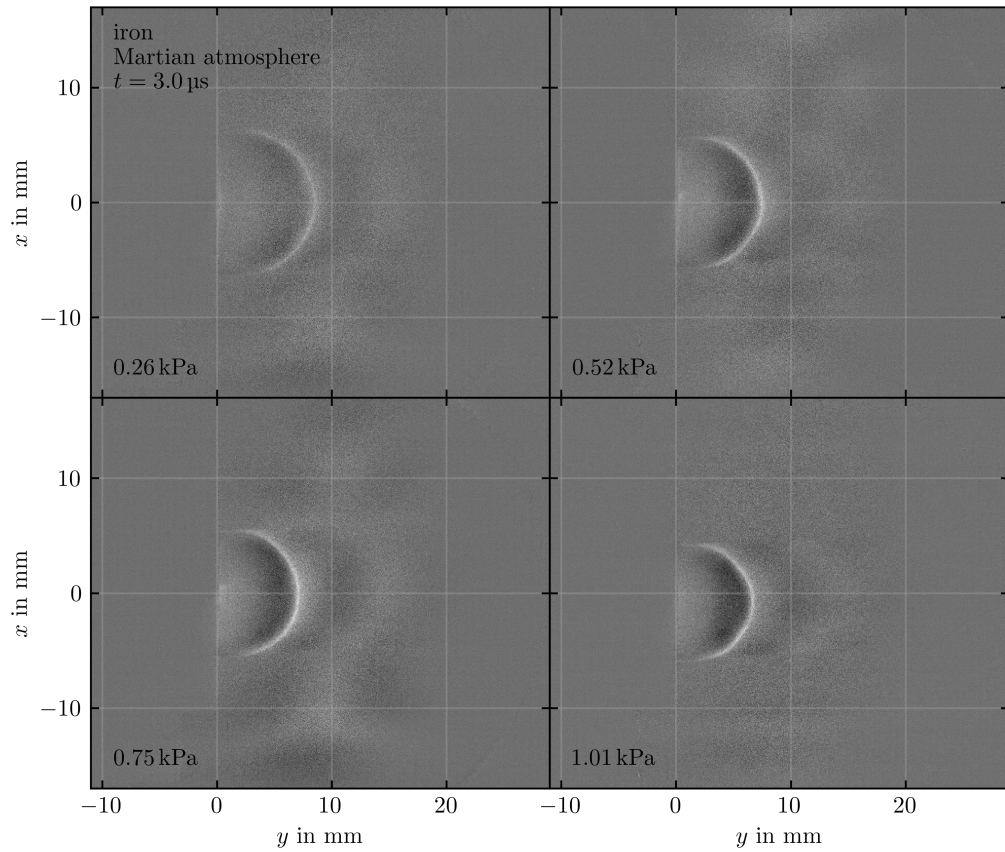


Figure C.7.: Schlieren images taken with an iron target at different ambient pressures in a simulated Martian atmosphere. The pressures p_0 are noted in the bottom left of each frame. All images were recorded at $t = 3.0 \mu\text{s}$ after plasma ignition. The reduced contrast at low pressures can be attributed to a weaker shock wave.

List of Figures

1.1. Shock Wave Expansion from an Iron Target	2
2.1. Principle of a LIBS Measurement	6
2.2. Optical and Thermal Penetration Depths	7
2.3. Breakdown Threshold in LIBS	9
2.4. Changes of a LIBS Spectrum over Time	11
2.5. Laser Parameters and Plasma Properties	12
2.6. Generation of a Shock Front	14
2.7. Weak Shock Wave	15
2.8. Principle of Shadowgraphing	19
2.9. Principle of Schlieren Imaging	19
2.10. Schlieren Imaging System with an Extended Light Source	21
2.11. Contrast in a Schlieren Apparatus	22
2.12. Density Gradient of a Weak Shock Wave	25
3.1. Setup with Multiple Diagnostic Tools	30
3.2. Plasma Imaging System	31
3.3. Schlieren Imaging System	33
3.4. Trigger Timings for Schlieren Imaging	35
3.5. Temporal Resolution of the Schlieren Imaging Light Source	36
3.6. Schlieren Images Before and After Background Subtraction	37
3.7. Cutoff Scan of the Schlieren System	38
3.8. Acoustic Recording System	39
3.9. Overview of the Samples	41
4.1. Time Series on Iron in Terrestrial Atmosphere	45
4.2. Schlieren Images of Shock Waves from all Samples in Martian Atmosphere	47
4.3. Refractive Index Distribution of a Shock Wave	49
4.4. Schlieren Images of a Time Series Measurement on Iron	50
4.5. Shock Wave Expansion from an Iron Sample	51
4.6. Decoupling of the Shock Wave from an Iron Sample in Martian atmosphere	53
4.7. Schlieren Images of a Shot Series Measurement on Talc	54
4.8. Development of the Shock Front Position in a Shot Series	55
4.9. Development of the Shock Wave Expansion in a Shot Series	56
4.10. Development of the Explosion Energy in a Shot Series	57
4.11. Acoustic Signal of the Pressure Wave	59
4.12. Development of the Acoustic Energy in a Shot Series	60
4.13. Correlation Between Decay Rate of the Acoustic Signal and the Vickers Hardness	61
4.14. Development of the LIBS spectrum in a Shot Series	63
4.15. Development of the Total Photon Count in a Shot Series	63

List of Figures

4.16. Development of Acoustic Energy, Explosion Energy and Total Photon Count in a Shot Series	65
4.17. Influence of the Laser Energy on the Shock Wave	69
4.18. Influence of the Ambient Pressure on the Shock Wave	71
B.1. Photos of the Schlieren Imaging System	82
B.2. Circuit Diagram of the Avalanche Pulse Generator	83
C.1. Time Series Measurements of all Samples	85
C.2. Pressure Behind the Shock Front	86
C.3. Irregular Shock Waves from Lead	86
C.4. Shot Series Measurements for All Samples	87
C.5. Combined Time and Shot Series Measurements for all Samples	88
C.6. Acoustic Shot Series Measurement of Talc	89
C.7. Influence of the Ambient Pressure on the Schlieren Contrast	90

Bibliography

- [1] S. M. Aberkane, A. Bendib, K. Yahiaoui, S. Boudjemai, S. Abdelli-Messaci, T. Kerdja, S. Amara, and M. Harith. Correlation between fe–v–c alloys surface hardness and plasma temperature via libs technique. *Applied surface science*, 301:225–229, 2014.
- [2] R. Anderson, S. Clegg, J. Frydenvang, R. Wiens, S. McLennan, R. Morris, B. Ehlmann, and M. Dyar. Improved accuracy in quantitative laser-induced breakdown spectroscopy using sub-models. *Spectrochimica Acta Part B: Atomic Spectroscopy*, 129:49–57, 2017.
- [3] R. Brennetot, J. Lacour, E. Vors, A. Rivoallan, D. Vailhen, and S. Maurice. Mars analysis by laser-induced breakdown spectroscopy (malis): influence of mars atmosphere on plasma emission and study of factors influencing plasma emission with the use of doehlert designs. *Applied spectroscopy*, 57(7):744–752, 2003.
- [4] S. Brieschenk, R. Hruschka, S. O’Byrne, and H. Kleine. High-speed time-resolved visualisation of laser-induced plasma explosions. In *28th International Congress on High-Speed Imaging and Photonics*, volume 7126, page 71260N. International Society for Optics and Photonics, 2009.
- [5] Z. Chen and A. Bogaerts. Laser ablation of cu and plume expansion into 1 atm ambient gas. *Journal of Applied Physics*, 97(6):063305, 2005.
- [6] B. Chide, O. Beyssac, K. Benzerara, M. Gauthier, S. Maurice, D. Mimoun, and R. Wiens. Acoustic monitoring of laser-induced phase transition in minerals. In *Lunar and Planetary Science Conference*, number 2326, page 1818, 2020.
- [7] B. Chide, S. Maurice, A. Cousin, B. Bousquet, D. Mimoun, O. Beyssac, P. Meslin, and R. Wiens. Recording laser-induced sparks on mars with the supercam microphone. *Spectrochimica Acta Part B: Atomic Spectroscopy*, 174:106000, 2020.
- [8] B. Chide, S. Maurice, N. Murdoch, J. Lasue, B. Bousquet, X. Jacob, A. Cousin, O. Forni, O. Gasnault, P. Meslin, et al. Listening to laser sparks: a link between laser-induced breakdown spectroscopy, acoustic measurements and crater morphology. *Spectrochimica Acta Part B: Atomic Spectroscopy*, 153:50–60, 2019.
- [9] A. Ciucci, M. Corsi, V. Palleschi, S. Rastelli, A. Salvetti, and E. Tognoni. New procedure for quantitative elemental analysis by laser-induced plasma spectroscopy. *Applied spectroscopy*, 53(8):960–964, 1999.
- [10] S. Clegg, R. Wiens, A. Misra, S. Sharma, J. Lambert, S. Bender, R. Newell, K. Nowak-Lovato, S. Smrekar, M. Dyar, et al. Planetary geochemical investigations using raman and laser-induced breakdown spectroscopy. *Applied Spectroscopy*, 68(9):925–936, 2014.

- [11] M. Corsi, G. Cristoforetti, M. Hidalgo, D. Iriarte, S. Legnaioli, V. Palleschi, A. Salvetti, and E. Tognoni. Effect of laser-induced crater depth in laser-induced breakdown spectroscopy emission features. *Applied spectroscopy*, 59(7):853–860, 2005.
- [12] J. Craig and F. M. Vokes. The metamorphism of pyrite and pyritic ores: an overview. *Mineralogical Magazine*, 57(386):3–18, 1993.
- [13] D. Cremers and L. Radziemski. *Handbook of Laser-Induced Breakdown Spectroscopy*. Wiley, 2013.
- [14] G. Cristoforetti, A. De Giacomo, M. Dell’Aglia, S. Legnaioli, E. Tognoni, V. Palleschi, and N. Omenetto. Local thermodynamic equilibrium in laser-induced breakdown spectroscopy: beyond the mcwhirter criterion. *Spectrochimica Acta Part B: Atomic Spectroscopy*, 65(1):86–95, 2010.
- [15] M. Dong, X. Mao, J. J. Gonzalez, J. Lu, and R. E. Russo. Time-resolved libs of atomic and molecular carbon from coal in air, argon and helium. *Journal of Analytical Atomic Spectrometry*, 27(12):2066–2075, 2012.
- [16] A. Effenberger and J. Scott. Effect of atmospheric conditions on libs spectra. *Sensors*, 10(5):4907–4925, 2010.
- [17] A. Fau, O. Beyssac, M. Gauthier, P. Meslin, A. Cousin, K. Benzerara, S. Bernard, J.-C. Boulliard, O. Gasnault, O. Forni, et al. Pulsed laser-induced heating of mineral phases: Implications for laser-induced breakdown spectroscopy combined with raman spectroscopy. *Spectrochimica Acta Part B: Atomic Spectroscopy*, 160:105687, 2019.
- [18] M. Gigosos, M. González, and V. Cardenoso. Computer simulated balmer-alpha,-beta and-gamma stark line profiles for non-equilibrium plasmas diagnostics. *Spectrochimica Acta Part B: Atomic Spectroscopy*, 58(8):1489–1504, 2003.
- [19] L. Grad and J. Možina. Acoustic in situ monitoring of excimer laser ablation of different ceramics. *Applied surface science*, 69(1-4):370–375, 1993.
- [20] D. Hahn and N. Omenetto. Laser-induced breakdown spectroscopy (libs), part i: review of basic diagnostics and plasma–particle interactions: still-challenging issues within the analytical plasma community. *Applied spectroscopy*, 64(12):335A–366A, 2010.
- [21] D. Hahn and N. Omenetto. Laser-induced breakdown spectroscopy (libs), part ii: review of instrumental and methodological approaches to material analysis and applications to different fields. *Applied spectroscopy*, 66(4):347–419, 2012.
- [22] S. Harilal, B. Brumfield, and M. Phillips. Lifecycle of laser-produced air sparks. *Physics of Plasmas*, 22(6):063301, 2015.
- [23] C. Harris, K. J. Millman, S. van der Walt, R. Gommers, P. Virtanen, D. Cournapeau, E. Wieser, J. Taylor, S. Berg, N. Smith, et al. Array programming with numpy. *Nature*, 585(7825):357–362, 2020.
- [24] N. Hosoya, M. Nagata, I. Kajiwara, and R. Umino. Nano-second laser-induced plasma shock wave in air for non-contact vibration tests. *Experimental Mechanics*, 56(7):1305–1311, 2016.

- [25] Y. Iida. Effects of atmosphere on laser vaporization and excitation processes of solid samples. *Spectrochimica Acta Part B: Atomic Spectroscopy*, 45(12):1353–1367, 1990.
- [26] K. Kagawa, T. Lie, R. Hedwig, S. Abdulmajid, M. Suliyanti, and H. Kurniawan. Sub-target effect on laser plasma generated by transversely excited atmospheric co2 laser at atmospheric gas pressure. *Japanese Journal of Applied Physics*, 39(5R):2643, 2000.
- [27] K. Kane and D. Cremers. An in situ technique for elemental analysis of lunar surfaces. In *New Technologies for Lunar Resource Assessment*. Lunar and Planetary Institute, 1992.
- [28] K. Kane and D. Cremers. Remote elemental analysis of planetary surfaces using laser-induced breakdown spectroscopy. In *Lunar and Planetary Science Conference*, volume 23. Lunar and Planetary Institute, 1992.
- [29] E. S. Kite. Geologic constraints on early mars climate. *Space Science Reviews*, 215(1):10, 2019.
- [30] A. Knight, N. Scherbarth, D. Cremers, and M. Ferris. Characterization of laser-induced breakdown spectroscopy (libs) for application to space exploration. *Applied Spectroscopy*, 54(3):331–340, 2000.
- [31] E. Lebigot. Uncertainties: a python package for calculations with uncertainties.
- [32] D. Lide. *CRC handbook of chemistry and physics*, volume 82. CRC press, 2002.
- [33] Y. Lu, Y. Lee, M. Hong, and T. Low. Acoustic wave monitoring of cleaning and ablation during excimer laser interaction with copper surfaces. *Applied surface science*, 119(1-2):137–146, 1997.
- [34] S. Maurice, S. Clegg, R. Wiens, O. Gasnault, W. Rapin, O. Forni, A. Cousin, V. Sautter, N. Mangold, L. Le Deit, et al. Chemcam activities and discoveries during the nominal mission of the mars science laboratory in gale crater, mars. *Journal of Analytical Atomic Spectrometry*, 31(4):863–889, 2016.
- [35] S. Maurice, R. Wiens, P. Bernardi, P. Caïs, S. Robinson, T. Nelson, O. Gasnault, J.-M. Reess, M. Deleuze, F. Rull, et al. The supercam instrument suite on the mars 2020 rover: Science objectives and mast-unit description. *Space Science Reviews*, 217(3):1–108, 2021.
- [36] S. Maurice, R. Wiens, M. Saccoccio, B. Barraclough, O. Gasnault, O. Forni, N. Mangold, D. Baratoux, S. Bender, G. Berger, et al. The chemcam instrument suite on the mars science laboratory (msl) rover: Science objectives and mast unit description. *Space science reviews*, 170(1-4):95–166, 2012.
- [37] K. Newbound. Refractive indices of water vapor and carbon dioxide at low pressure. *Journal of the Optical Society of America*, 39(10):835–840, 1949.
- [38] R. Noll. *Laser-induced breakdown spectroscopy*. Springer, 2012.
- [39] I. Ordonez-Etxeberria, R. Hueso, A. Sánchez-Lavega, E. Millour, and F. Forget. Meteorological pressure at gale crater from a comparison of rems/msl data and mcd modelling: Effect of dust storms. *Icarus*, 317:591–609, 2019.

- [40] R. Orosei, S. Lauro, E. Pettinelli, A. Cicchetti, M. Coradini, B. Cosciotti, F. Di Paolo, E. Flamini, E. Mattei, M. Pajola, et al. Radar evidence of subglacial liquid water on mars. *Science*, 361(6401):490–493, 2018.
- [41] S. Palanco and J. Laserna. Spectral analysis of the acoustic emission of laser-produced plasmas. *Applied optics*, 42(30):6078–6084, 2003.
- [42] S. Preuss, A. Demchuk, and M. Stuke. Sub-picosecond uv laser ablation of metals. *Applied physics A*, 61(1):33–37, 1995.
- [43] K. Rammelkamp. *Investigation of LIBS and Raman data analysis methods in the context of in-situ planetary exploration*. PhD thesis, Humboldt-Universität zu Berlin, 2019.
- [44] A. Sasoh, T. Ohtani, and K. Mori. Pressure effect in a shock-wave–plasma interaction induced by a focused laser pulse. *Physical review letters*, 97(20):205004, 2006.
- [45] S. Schröder. *Laser-induced breakdown spectroscopy for planetary research: Analysis of salts and frozen salt solutions under Martian conditions*. PhD thesis, Technische Universität Berlin, 2013.
- [46] S. Schröder, K. Rammelkamp, F. Hanke, I. Weber, D. Vogt, S. Frohmann, S. Kubitzka, U. Böttger, and H.-W. Hübers. Effects of pulsed laser and plasma interaction on fe, ni, ti, and their oxides for libs raman analysis in extraterrestrial environments. *Journal of Raman Spectroscopy*, 51(9):1667–1681, 2020.
- [47] S. Schröder, K. Rammelkamp, D. Vogt, O. Gasnault, and H.-W. Hübers. Contribution of a martian atmosphere to laser-induced breakdown spectroscopy (libs) data and testing its emission characteristics for normalization applications. *Icarus*, 325:1–15, 2019.
- [48] G. Senesi. Laser-induced breakdown spectroscopy (libs) applied to terrestrial and extraterrestrial analogue geomaterials with emphasis to minerals and rocks. *Earth-Science Reviews*, 139:231–267, 2014.
- [49] G. Settles. *Schlieren and shadowgraph techniques: visualizing phenomena in transparent media*. Springer Science & Business Media, 2001.
- [50] G. Settles and M. Hargather. A review of recent developments in schlieren and shadowgraph techniques. *Measurement Science and Technology*, 28(4):042001, 2017.
- [51] S. Shabanov and I. Gornushkin. Two-dimensional axisymmetric models of laser induced plasmas relevant to laser induced breakdown spectroscopy. *Spectrochimica Acta Part B: Atomic Spectroscopy*, 100:147–172, 2014.
- [52] J. Singh and S. Thakur. *Laser-induced breakdown spectroscopy*. Elsevier, 2007.
- [53] A. Spiga, F. Forget, B. Dolla, S. Vinatier, R. Melchiorri, P. Drossart, A. Gendrin, J.-P. Bibring, Y. Langevin, and B. Gondet. Remote sensing of surface pressure on mars with the mars express/omega spectrometer: 2. meteorological maps. *Journal of Geophysical Research: Planets*, 112(E8), 2007.
- [54] E. Taylor. Correlation of the mohs’s scale of hardness with the vickers’s hardness numbers. *Mineralogical Magazine and Journal of the Mineralogical Society*, 28(206):718–721, 1949.

- [55] K. Tsuyuki, S. Miura, N. Idris, K. Kurniawan, T. Lie, and K. Kagawa. Measurement of concrete strength using the emission intensity ratio between ca (ii) 396.8 nm and ca (i) 422.6 nm in a nd: Yag laser-induced plasma. *Applied spectroscopy*, 60(1):61–64, 2006.
- [56] T. Valentino. Analytical model to determine the relevant parameters governing the transferred momentum to spherical indenters by laser-induced shock waves. *Optics and Lasers in Engineering*, 145:106670, 2021.
- [57] P. Ventzek, R. Gilgenbach, J. Sell, and D. Heffelfinger. Schlieren measurements of the hydrodynamics of excimer laser ablation of polymers in atmospheric pressure gas. *Journal of applied physics*, 68(3):965–968, 1990.
- [58] P. Virtanen, R. Gommers, T. Oliphant, M. Haberland, T. Reddy, D. Cournapeau, E. Burovski, P. Peterson, W. Weckesser, J. Bright, S. van der Walt, M. Brett, J. Wilson, K. Millman, N. Mayorov, A. Nelson, E. Jones, R. Kern, E. Larson, C. Carey, Í. Polat, Y. Feng, E. Moore, J. VanderPlas, D. Laxalde, J. Perktold, R. Cimrman, I. Henriksen, E. Quintero, C. Harris, A. Archibald, A. Ribeiro, F. Pedregosa, P. van Mulbregt, and SciPy 1.0 Contributors. SciPy 1.0: Fundamental Algorithms for Scientific Computing in Python. *Nature Methods*, 17:261–272, 2020.
- [59] D. Vogt. *Laser-Induced Breakdown Spectroscopy for the Exploration of Mars: Analysis of Molecular Emissions and Spatial Characterization of the Plasma*. PhD thesis, Humboldt-Universität zu Berlin, 2020.
- [60] D. Vogt, K. Rammelkamp, S. Schröder, and H.-W. Hübers. Molecular emission in laser-induced breakdown spectroscopy: An investigation of its suitability for chlorine quantification on mars. *Icarus*, 302:470–482, 2018.
- [61] D. Vogt, S. Schröder, K. Rammelkamp, P. Hansen, S. Kubitzka, and H.-W. Hübers. Cacl and caf emission in libs under simulated martian conditions. *Icarus*, 335:113393, 2020.
- [62] D. Vogt, S. Schröder, S. Frohmann, P. Hansen, F. Seel, M. Gensch, and H.-W. Hübers. Spatial characterization of the laser-induced plasma of calcium sulfate in simulated martian ambient conditions. Article in preparation, Deutsches Zentrum für Luft- und Raumfahrt.
- [63] W. Wei, X. Li, J. Wu, Z. Yang, S. Jia, and A. Qiu. Interferometric and schlieren characterization of the plasmas and shock wave dynamics during laser-triggered discharge in atmospheric air. *Physics of Plasmas*, 21(8):083112, 2014.
- [64] R. Wiens, S. Maurice, B. Barraclough, M. Saccoccio, W. Barkley, J. Bell, S. Bender, J. Bernardin, D. Blaney, J. Blank, et al. The chemcam instrument suite on the mars science laboratory (msl) rover: Body unit and combined system tests. *Space science reviews*, 170(1):167–227, 2012.
- [65] R. Wiens, S. Maurice, and F. Rull Perez. The supercam remote sensing instrument suite for the mars 2020 rover mission: A preview. *Spectroscopy*, 32(LA-UR-17-26876), 2017.
- [66] J.-P. Williams. Acoustic environment of the martian surface. *Journal of Geophysical Research: Planets*, 106(E3):5033–5041, 2001.

Bibliography

- [67] K. Williford, K. Farley, K. Stack, A. Allwood, D. Beaty, L. Beegle, R. Bhartia, A. Brown, M. de la Torre Juarez, S.-E. Hamran, et al. The nasa mars 2020 rover mission and the search for extraterrestrial life. In *From habitability to life on Mars*, pages 275–308. Elsevier, 2018.
- [68] S. Yalçın, D. Crosley, G. Smith, and G. Faris. Influence of ambient conditions on the laser air spark. *Applied Physics B Lasers and Optics*, 68:121–130, 1999.
- [69] Y. Zel'Dovich and Y. Raizer. *Physics of shock waves and high-temperature hydrodynamic phenomena*. Academic Press, 1966.